# PROPAGATION OF THE FAST MAGNETOSONIC WAVE IN A TOKAMAK PLASMA

Thesis by

David Li-Shui Quek Hwang

In Partial Fulfillment of the Requirements

For the Degree of

Doctor of Philosophy

California Institute of Technology

Pasadena, California

1979

(Submitted June 15, 1978)

ACKNOWLEDGMENTS

I would like to express my deep appreciation to my thesis advisor, Professor Roy W. Gould, for his guidance, encouragement, and many direct contributions throughout the course of this investigation. His insight and knowledge of plasma physics have been extremely enlightening.

I am indebted to Professor William Bridges, Dr. James Long, and Professor Hardy Martel for the useful discussions and suggestions on both circuit theory and experimental techniques. Many of their suggestions have led to fruitful results.

Special thanks go to Dr. Gary Bedrosian and Professor Paul Bellan for their critical reading of the manuscript and useful comments for improvements. Special gratitude is extended to Dr. Mario Simonutti for help and discussions on the initial theoretical part of this work.

I would like to thank Mr. Frank Cosso for his skillful assistance in the contruction of experimental instruments. To Mrs. Edith Huang I would like to extend my appreciation for her help on writing and debugging many computer programs. I am very grateful to Mrs. Ruth Stratton and Mrs. Verona Carpenter for their excellent typing, and especially to Mrs. Stratton for proofreading the original text.

The generous financial support from the U. S. Department of Energy in carrying out this work is gratefully acknowledged.

To my wife, Mona, and my sister in-law, Lenita, thank you for the help in preparing the manuscript. Finally, I would like to dedicate this thesis to the members of my family, especially to my parents, for their constant support, encouragement, love, and understanding without which this work would not have been possible.

ABSTRACT

The propagation of the fast magnetosonic wave in a tokamak plasma has been investigated at low power, between 10 and 300 watts, as a prelude to future heating experiments.

The attention of the experiments has been focused on the understanding of the coupling between a loop antenna and a plasma-filled cavity. Special emphasis has been given to the measurement of the complex loading impedance of the plasma. The importance of this measurement is that once the complex loading impedance of the plasma is known, a matching network can be designed so that the r.f. generator impedance can be matched to one of the cavity modes, thus delivering maximum power to the plasma. For future heating experiments it will be essential to be able to match the generator impedance to a cavity mode in order to couple the r.f. energy efficiently to the plasma.

As a consequence of the complex impedance measurements, it was discovered that the designs of the transmitting antenna and the impedance matching network are both crucial. The losses in the antenna and the matching network must be kept below the plasma loading in order to be able to detect the complex plasma loading impedance. This is even more important in future heating experiments, because the fundamental basis for efficient heating before any other consideration is to deliver more energy into the plasma than is dissipated in the antenna system.

The characteristics of the magnetosonic cavity modes are confirmed by three different methods. First, the cavity modes are observed as voltage maxima at the output of a six-turn receiving probe.

Second, they also appear as maxima in the input resistance of the transmitting antenna. Finally, when the real and imaginary parts of the measured complex input impedance of the antenna are plotted in the complex impedance plane, the resulting curves are approximately circles, indicating a resonance phenomenon.

The observed plasma loading resistances at the various cavity modes are as high as 3 to 4 times the basic antenna resistance ($\sim .4\ \Omega$). The estimated cavity Q's were between 400 and 700. This means that efficient energy coupling into the tokamak and low losses in the antenna system are possible.

TABLE OF CONTENTS

# I. INTRODUCTION

## 1.1 Introduction to Tokamak Fusion and Plasma Heating

In order to produce net energy from controlled thermonuclear fusion, two physical parameters, the product of the plasma density $n$ and the confinement time $\tau$, and the ion temperature $T_i$ must simultaneously satisfy the Lawson criterion. The Lawson criterion is a statement of energy break-even in a thermonuclear reaction, where the energy gained in the reaction equals the energy lost due to both radiation and particle losses. For example, the Lawson criterion for the deuterium and tritium reaction

$$D + T \rightarrow {}^4He\ (3.5\ MeV) + n\ (14.1\ MeV) \qquad (1.1)$$

is that $T_i \geq 10$ keV, and $n\tau \geq 10^{14}$. Among the many methods under study to reach the Lawson criterion, one device that has made a great deal of progress toward achieving these parameters is the tokamak.

A tokamak is a toroidal magnetic confinement device with a toroidal magnetic field and an inductively induced toroidal current (Figure 1.1; and for details see Section 3.1). The toroidal current serves a two-fold purpose: 1) to produce a poloidal field which provides the proper rotational transform for plasma equilibrium; 2) to heat the plasma by ohmic dissipation due to the plasma resistance.

There is a limit to the plasma temperature that can be reached by heating the tokamak plasma with the toroidal current, because the plasma resistance decreases with increasing plasma temperature. To dissipate the same amount of ohmic power, $I_p^2R$, in the plasma at a higher temperature, the plasma current, $I_p$, must be higher since the plasma resistance $R$ is

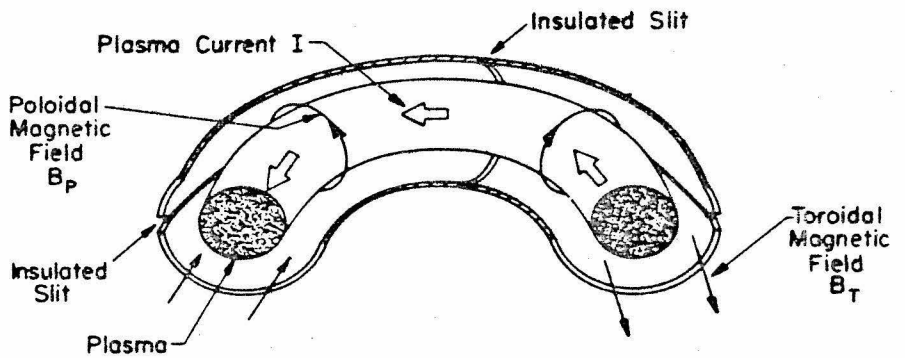


Figure 1.1
Schematic of a Tokamak (From Principles of Plasma Physics, by N. A. Krall and A. W. Trivelpiece)

lower. The limit on the magnitude of the toroidal plasma current that can be used for ohmic heating is the condition for plasma equilibrium which specifies the maximum allowable poloidal magnetic field for a given toroidal magnetic field (see Section 3.1).

The inverse temperature dependence of the plasma resistance is the result of the Coulomb interaction of the charged particles in a plasma. The plasma resistivity, or the Spitzer resistivity, is as follows:

$$\rho_s = 1.65 \times 10^{-9} Z \ln \Lambda / T^{3/2} \qquad (1.2)$$

where $\Lambda = 12\pi(\varepsilon_o k_B T/e^2)^{3/2} / \sqrt{n_e}$, and $T_e$ is in keV. Thus, after the plasma temperature has reached between 1 and 3 keV, other plasma heating methods must be used to supplement ohmic heating and to bring the ion temperature to the required value. Currently, the two major proposed methods for auxiliary heating of a tokamak plasma are neutral beam injection heating and radio frequency wave heating.

The reason for using neutral beam injection to heat the plasma instead of ion beam injection is that charged particles cannot penetrate the magnetic field of the tokamak. The neutral particle injection scheme is to inject a beam of energetic neutral particles across the magnetic field. The neutral particles can deliver energy to the ions by charge exchange with cold ions in the plasma, thus resulting in energetic ions and cold neutrals which will escape.

The neutral beam is produced by passing an intense ion beam through a gas neutralizing cell. Energetic neutrals can be formed by electron capture by positive ions, electron stripping by negative ions or dissociation of molecular ions [1]. Injection experiments using either

hydrogen or deuterium beams with powers up to 700 kW have been performed in various tokamaks around the world. A heating efficiency of 57%, for example, has been reported by the TFR group in France [2].

Although neutral beam heating has enjoyed success in the present experimental tokamaks, there are doubts about its efficiency in heating the bulk of the ion distribution in a reactor-size tokamak, which would be much larger. Because of the increase in size of the reactor tokamaks, higher energy neutral particles are needed in order to penetrate to the center of the tokamak. At present, difficulties have been encountered with efficient neutralization of ion beams with energy greater than 120 keV. Therefore, alternatives to the neutral beam heating must be studied for the auxiliary heating of a reactor-size tokamak.

The use of radio frequency electromagnetic waves to heat a plasma was proposed in the early days of plasma physics. Efficient high power wave generators in the radio frequency range are at present readily available, and so the technological basis for using electromagnetic wave heating is quite sound. Because of technical know-how in radio wave generation, the cost of using r.f. heating in a reactor-size tokamak could be lower than that for neutral beam heating.

The heating of a plasma using r.f. waves has been summarized by T. H. Stix as follows [3]. First, the r.f. wave must be generated and delivered to the plasma. The r.f. energy is then coupled to the plasma and an "efficient way to couple the r.f. energy into the plasma is to match the frequency and parallel wavelength of the driving field to those of a natural mode in the plasma, thereby exciting a 'coupling resonance'." The r.f. wave interacts with the plasma through "either linear or nonlinear

processes". There is some absorption process of the wave in the plasma, "which competes with eddy current dissipation in the walls". Finally, there must be "effective thermalization of the energy added to the plasma".

One proposed method for r.f. heating is the use of the magnetosonic wave to heat the ions. The attractive feature of this method is that the wave energy should couple directly to the ions, instead of heating the electrons first, then relying on electron-ion collisions to transfer energy to the ions. The propagation of the magnetosonic wave in a magnetized plasma can be approximately described by the cold plasma dispersion relation. The cold plasma dispersion relation indicates that there are two branches of waves that can propagate when the wave frequency is approximately equal to the ion cyclotron frequency. One branch is the ion cyclotron wave which is left-circularly polarized (LCP) and has a resonance, i.e., a large plasma response to the field, at the ion cyclotron frequency (Appendix b). The other branch is the magnetosonic wave which is right-circularly polarized (RCP) and does not have a resonance at the ion cyclotron frequency.

When the magnetosonic wave is propagating in a plasma-filled metallic container such as a tokamak, the appropriate EM problem can be thought of as that of wave propagation in a dielectric-filled cavity. At first sight one would not expect to be able to couple energy to the ions using the magnetosonic wave, because it has the wrong polarization. However, when temperature effects are included in the dispersion relation, one finds that the magnetosonic wave is no longer purely RCP, but contains a small left-handed component. F. Perkins [4] has worked out the damping decrements of the magnetosonic wave in a finite temperature

plasma at both the ion cyclotron and twice the ion cyclotron frequencies. It is found that the damping is not strong, and it is a linear function of the ion temperature of the plasma.

Wave propagation in a plasma-filled cavity can be described by the dispersion relation of the wave and the proper boundary conditions. To keep the theory simple and yet retain the essential features of the physics, some approximations are introduced. The plasma is assumed to be cold, uniform, and magnetized. The tokamak is approximated by a cylindrical cavity with perfectly conducting walls and a periodic boundary condition in the axial direction. The wave propagation problem is solved in cylindrical coordinates with the plasma magnetized along the axial direction. From the cold plasma theory, the dispersion relation, $\omega = \omega(\underline{k})$, is obtained, where $\underline{k}$ is the wave vector (see Section 2.1). Once the plasma is placed in the cylindrical cavity, only discrete values of $\underline{k}$ which satisfy the boundary conditions can exist, i.e., the conducting wall boundary conditions being that the tangential electric field and the normal magnetic field must vanish at the boundary. By exciting the magnetosonic wave at the eigenmode frequencies, $\omega = \omega(\underline{k})$, standing waves are set up in the cavity; thus, one has a forced oscillation system which will enhance the damping of the wave. With the simple assumptions used here, there are a few experimental effects that are neglected in the theory, for example, the toroidal effects, effects due to both density and magnetic field gradients, the poloidal field effects, finite temperature effects, and the effects of the cavity wall resistance. Nevertheless, the simple cold plasma theory describes the propagation of the magnetosonic wave reasonably well (see Section 2.2 for references to other

theories that include these effects).

The problem of efficient r.f. heating of a tokamak plasma using the fast magnetosonic wave can be studied in the following way. First, the physics of the cavity modes must be understood experimentally. This can be done by studying both the standing wave patterns of the eigenmodes in the tokamak and the plasma loading behavior at the transmitting antenna during the passage through a cavity mode. Second, efficient ways to feed r.f. energy into a plasma at the cavity modes need to be examined carefully. By knowing the complex plasma loading impedance, the antenna and the matching network can be designed so that the generator impedance can be properly matched to the antenna at a cavity mode. This ensures maximum power input into the plasma. Third, the duration of the cavity modes used for heating must be long enough during the discharge to get any significant increase in plasma temperature. Usually in the present day tokamak discharges, the duration of the eigenmodes is not long enough for effective plasma heating. The reason is that a particular cavity mode is excited only during the time when both the plasma density and the input frequency satisfy simultaneously the dispersion relation and the boundary conditions. As soon as the plasma density is changed sufficiently, this mode no longer propagates in the tokamak, and so no more wave heating is possible. One proposed way to track the modes is by changing the input frequency of the transmitter to compensate for any changes in the density which will shorten the duration of the modes. Finally, high power experiments can be done to study the physics of the damping mechanism of the wave by the plasma, and the actual temperature

increase of the plasma due to the r.f. power input.

## 1.2 Summary of Previous Work on Magnetosonic Wave Heating in Tokamaks

The first series of magnetosonic wave heating experiments in the United States was done in the ST tokamak and the ATC tokamak at Princeton [5,6]. Initially, a low power experiment was performed on the ST tokamak to show the existence of the magnetosonic wave and to study the resistive loading of the transmitting antenna by the modes. The modes were identified by measuring the standing wave patterns using a number of probes placed around the tokamak. Both poloidal and toroidal mode numbers, m and N, were obtained. Matching networks were used so that the r.f. generator impedance could be matched to one of the cavity resonances [7]. The resistive loading of the transmitting antenna by various modes was measured, and resistive loading results indicated that efficient wave generation in the tokamak was possible.

One of the ST tokamak experimental results which was predicted by a theory worked out by Chance and Perkins [8] was that the m = -1 mode was split by the effect of the poloidal magnetic field (where the fields vary as $e^{i(kz+m\theta-\omega t)}$), which makes the phase velocity of this mode different when propagating in the opposite direction along the toroidal axis. In other words, the dispersion curves for the m = -1 modes with positive and negative N, the toroidal mode number, are different from each other. The splitting of the m = -1 mode appears as "double humps" on the cavity resonance peaks.

High power experiments were done with power level up to 1 MW in the ST tokamak with a hydrogen plasma, and a typical ion temperature increase of 100 eV was observed [8]. This corresponded to a heating efficiency of

20%. High power experiments in a deuterium plasma were also performed in the ST and ATC tokamaks. However, the cavity Q of the cavity modes measured in the deuterium plasma is much lower than the theoretical predictions. At present, it is believed that the observed discrepancy is due to the two ion hybrid resonance effect between the deuteron plasma and the proton impurities in the tokamaks [6]. In this thesis the experiments are done in a hydrogen plasma; thus, there are no two-ion hybrid resonance effects. No further discussion will be made on this effect, except to refer the interested reader to the latest theoretical and experimental publications on the subject.

Magnetosonic wave heating experiments were also performed on the TM-1-VCH tokamak and the TO-1 tokamak in the Soviet Union [9,10]. The TM-1-VCH tokamak is a small device with the major torus radius R = 40 cm and the plasma radius=8 cm. Ion temperature increase of up to 100 eV at generator power levels of 40 kW was reported. When a deuterium plasma is used, the phenomenon of low cavity Q at the eigenmodes was also observed, and the cavity Q was found to be about 10. Magnetosonic wave heating experiments in the TO-1 had produced comparable ion temperature increases. In the TO-1 experiments, some kind of frequency modulation had been used to compensate any density variations and thus to remain on one of the modes for a longer duration [10].

Another experiment at low power level (approximately 1kW) was done on the TFR tokamak in France. In this experiment careful studies of the density dependence of the eigenmodes, and tracking of the modes using frequency modulation were performed. One of the interesting discoveries

in the experiment was that the amplitude maxima of the eigenmodes appeared to be modulated at a frequency around 1 kHz. This modulation was due to a periodic density fluctuation in the tokamak of about .5% at 1 kHz as observed using soft x-ray diagnostics. The decrease of the cavity Q in a deuterium plasma was examined in these experiments, and some agreements between the data and the two-ion hybrid resonance theory were found [11]. Mode tracking using frequency compensation was attempted. The phase information between a local oscillator and a receiving probe signal was used to frequency modulate the pilot oscillator. The density in the TFR varied only a few percent for several tens of msec. The direction of the change in the frequency of the pilot oscillator was such that it compensated any change in density which would destroy the cavity resonance effect. Typically, a resonance condition which lasted for .2 msec was extended to a duration of 5 msec [12]. In this experiment, the transmitting antenna was carefully designed for low losses and good coupling to the plasma.

Recently, magnetosonic wave experiments were done in two of the smaller tokamaks, the Microtor at UCLA and the Erasmus tokamak in Brussels, Belgium [13,14]. The results from the Microtor "showed no evidence of a correlation between the excitation of Alfven (magnetosonic) resonances and the antenna loading. Upper bound estimates on these experiments indicate that 70% of the applied power went into the plasma but less than 5% appeared as resonances" [13]. This result does not agree with the data presented in this thesis, where it was found that most of the r.f. power went into the plasma via the cavity resonances. However,

not enough is known about the experimental procedures used in the UCLA experiments to resolve this difference. The preliminary measurements in the Erasmus tokamak "does not show a large increase of absorption due to magnetosonic resonances. This is in disagreement with the resonance loading seen on the TFR, T4, and the Caltech tokamak" [14]. In the Erasmus tokamak experiments the modulation of the resonance peaks by a periodic density fluctuation which was first reported by the TFR group was also observed.

The magnetosonic wave experiment was done in the larger tokamak at UCLA, the Macrotor tokamak (R = 95 cm, a = 44 cm) [15]. "In this machine one is able to observe a definite correlation between antenna loading and magnetosonic resonances for well shielded antenna, and during the low density portion of the shot." The resonance loading was reported to be between .5 and 1 ohm. "However, this wave loading is masked by the parasitic loading during the early part of the shot when the density is high."

## 1.3 General Thesis Outline

This thesis has been devoted to the understanding of how to couple r.f. energy efficiently into a tokamak plasma via the magnetosonic cavity modes. Special attention was given to the measurement of the complex plasma loading impedance of the plasma at the cavity modes. The ratio of the real part of the plasma loading impedance and the antenna resistance determines the efficiency of the wave generation in the tokamak at the cavity modes. The complex plasma loading impedance contains the information needed to match the r.f. generator impedance to the antenna during the presence of a cavity mode. Careful designs of the antenna and the impedance matching network were found to be necessary for efficient energy coupling to the tokamak plasma and properly matching the generator impedance to the antenna at a cavity mode.

In Chapter II, the theory of the magnetosonic wave in an axially magnetized cold uniform plasma filled cylindrical cavity is presented. Although the cylindrical cold plasma theory is only an approximation to the experimental conditions in a tokamak plasma, the theory is found to agree reasonably with the transmission data of the cavity modes. The characteristics of the magnetosonic cavity modes are determined from the cold plasma dispersion relation, $\omega = \omega(\underline{k})$, and the discrete values of the wave vector, $\underline{k}$, which satisfies the boundary conditions at the cavity wall. Each of the discrete cavity modes is associated with a particular wave vector which is represented by a set of mode numbers $(\ell,m,N)$ corresponding to the three components of the wave vector, where $\ell$ is the radial modes number, m is the poloidal mode number, and $N$ is

the axial mode number. An equivalent circuit representation of the transmitting antenna and the tokamak cavity is used to obtain relations between various physical parameters of the cavity modes [Section 2.3]. The antenna input impedance has been calculated from the equivalent circuit with the antenna modelled by a transformer, and each of the cavity modes represented by a R-L-C resonant circuit. The various circuit parameters used in this calculation are either derived from theory, or measured experimentally [Section 2.8].

In Chapter III, the operating conditions and the plasma parameters of the Caltech tokamak are discussed, and the various diagnostic tools available on the Caltech tokamak are described. The time dependence of the plasma density, which is an important parameter governing the behavior of the cavity modes, is given [Section 3.1]. Typically, the plasma density increases rapidly during the first .3 millisecond, then decays quickly to 20% of its maximum value in the next 2 milliseconds, and stays constant at around $1 \times 10^{12}$ particles per $cm^3$ for the remainder of the discharge.

Chapter IV is devoted to the experimental apparatus and procedures of the different r.f. meausrements. The transmission measurements were made with a single-turn tungsten transmitting loop antenna and a small six-turn receiving loop probe with low coupling coefficient so as not to load the cavity modes in the tokamak [Section 4.1]. The input antenna resistance was determined by measuring the incident and reflected power into the antenna with a VHF directional coupler, and the r.f. current in the antenna with a high frequency current probe [Section 4.3].

The plasma loading resistance was obtained by determining the additional resistance present at the transmitting antenna due to the plasma effect. The complex input impedance of the antenna was computed from the data of the amplitude and the phase difference of the incident and reflected waves from the VHF directional coupler [Section 4.4]. Considerations that went into the design of the two-turn copper transmitting antenna and the impedance matching network using vacuum variable capacitors are discussed in section 4.2, and the details of the construction of the copper antenna are given in Appendix a.

Chapter V contains the experimental results of the r.f. measurements and the computed values of the equivalent circuit parameters from measured data. The computed equivalent circuit parameters of the cavity modes include the antenna input impedance under different experimental conditions, the cavity Q of the various cavity modes, and the antenna coupling coefficient at the various cavity modes. The data from the transmission measurements at the cavity modes appear as voltage maxima in the output signal of the receiving probe, and agree reasonably with the cold plasma theory given in Chapter II when the experimental data are superimposed on the dispersion curves of the cavity modes in a frequency versus density plot [Section 5.1]. Plasma loading resistance at the cavity modes has been observed to be as high as 3 to 4 times the basic antenna resistance [Section 5.3]. The complex plasma loading impedance at the cavity modes follows the general behavior of the impedance function derived from the equivalent circuit model of the

cavity modes [Section 5.5]. When the real and imaginary parts of the measured plasma loading impedance are plotted on the complex impedance plane as a cavity mode is passed through, the resultant curve is approximately a circle indicating a resonance effect.

Section 5.6 contains the estimated values of the cavity Q and the coupling coefficient for the various cavity modes. The cavity Q can be estimated from the time dependence of the plasma evolution by using the approximate frequency-density relation for the cavity mode cutoffs [Section 2.6]. The estimated Q obtained from the density data is the cavity Q loaded by the impedance of the antenna and the r.f. generator. The unloaded cavity Q, $Q_0$, can be related to the loaded Q by a circuit equation. Once $Q_0$ is known, the antenna coupling coefficient, $\kappa$, can be obtained from the circuit model of the antenna-cavity coupling. After the parameters of the equivalent circuit have been computed, the wave generation efficiency, $\eta$, of the antenna is estimated. For the present antenna design, the efficiency has been found to be as high as 80%.

In Section 5.5, attempts to match the r.f. generator impedance to the antenna when one of the cavity modes is resonant are described. Due to the variation of the plasma density with time, this matching can only be done for a brief interval. The ability to match to a cavity mode is the ultimate goal of the entire experiment, because in order to deliver the maximum amount of power to the plasma, the generator impedance must be properly matched at a cavity resonance where the

loading is stronger than when there is no resonance.

Finally, the experimental results and conclusions are summarized in Chapter VI, and some improvements to the experimental apparatus for future high power experiments are suggested.

# II. COLD PLASMA THEORY AND CIRCUIT MODELING OF THE CAVITY MODES

## 2.1 Theory for a Cold Uniform Cylindrical Plasma Cavity

The mode structure of the electromagnetic wave in a dielectric filled cavity with perfect conducting walls can be obtained from Maxwell's equations, equations for the dynamics of the plasma, and the boundary conditions at the cavity wall. For substitution of the plasma dynamics into the Maxwell's equations, it is convenient to derive a relation between the plasma current density and the electric field. The plasma current density can be thought of as a displacement current in a dielectric medium, as shown in equation (b.1) of Appendix b, and the dynamics of the magnetized plasma is represented by a dielectric tensor [16]

$$\underline{\underline{\varepsilon}} = \begin{bmatrix} \varepsilon_\perp & j\varepsilon_x & 0 \\ -j\varepsilon_x & \varepsilon_\perp & 0 \\ 0 & 0 & \varepsilon_{||} \end{bmatrix}$$

where the definitions of the components of the dielectric tensor are given in equation (b.3) of Appendix b. For the propagation of the magnetosonic wave in the tokamak, the following assumptions are made to keep the theory simple, yet contain enough physics to reveal the essential features of the cavity modes. The chamber of the tokamak is approximated by a cylindrical cavity with perfectly conducting wall and periodic boundary condition in the axial direction (Figure 2.1). The plasma is assumed to be uniform, cold, collisionless, and axially magnetized with a uniform magnetic field, $\underline{B}_o$. Several approximations of the dielectric properties of the plasma can be used to simplify the dispersion relation. For instance, in the dielectric tensor of the magnetized plasma, terms of the order $(m_e/m_i)$,

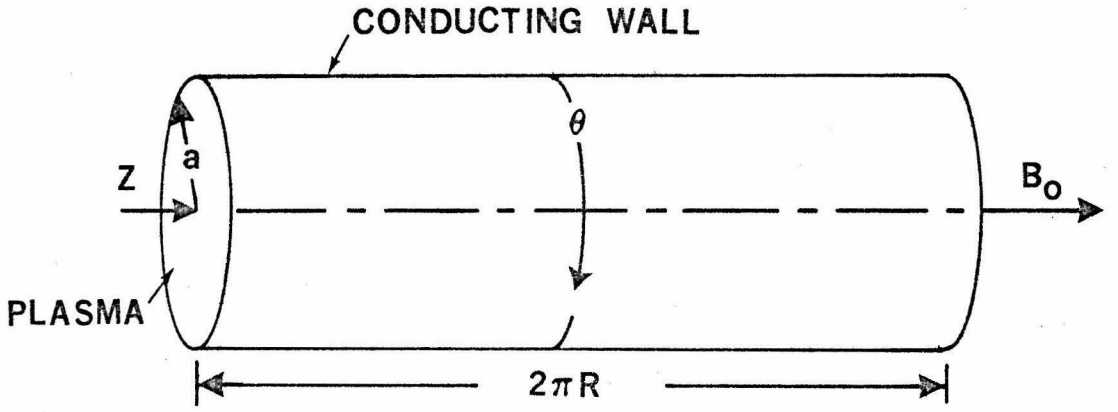


Figure 2.1

Plasma filled cylindrical cavity with conducting wall. R is the major radius, and a is the minor radius of the tokamak. Periodic boundary condition is imposed in the z direction.

where $m_e$ and $m_i$ are the electron and ion masses, respectively, are neglected. The propagation frequency of the wave is taken to be near the ion cyclotron frequency, which is much smaller than the electron cyclotron frequency and the electron plasma frequency. After including all the simplifications mentioned above, the resulting dispersion for the magnetosonic wave is as follows [17]:

$$k^2 = \frac{\Omega_i^2 \omega_{ci}^2}{V_A^2(1-\Omega_i^2)} - T^2/2 + \sqrt{\left(\frac{T^2}{2}\right)^2 + \left(\frac{\Omega_i^3 \omega_{ci}^2}{V_A^2(1-\Omega_i^2)}\right)^2} \qquad (2.1.1)$$

where T and k are the radial and axial components of the wave vector, $\omega_{ci}$ is the angular ion cyclotron frequency, $\Omega_i$ is $\omega/\omega_{ci}$, $V_A = B_o/\sqrt{\mu_o m_i n_i}$ is the Alfven velocity in the plasma, and $n_i$ is the ion number density. (For more details, see Appendix b).

All the transverse components of the electric and magnetic fields can be expressed in terms of the axial electric field, $E_z$, and axial magnetic field, $H_z$. A consequence of the propagation frequency being much smaller than the electron plasma frequency is that $E_z$ is small (see Appendix b). For our calculation $E_z$ is assumed to be zero. The solution of the axial magnetic field, $H_z$, as shown in equation (b.31) is

$$H_z = H_o J_m(Tr)\, e^{j(\omega t - m\theta - kz)} \qquad (2.1.2)$$

where $J_m$ is an integer order Bessel function, T and k are the radial and axial components of the wave vector, respectively. (Note the fields vary as $e^{-jm\theta}$ --different from the $e^{jm\theta}$ dependence used in some of the references.)

The boundary condition for the cavity is $E_\theta = H_r = 0$ at the conducting wall, i.e., at r = a. As shown in Appendix b, equation (b.32), the boundary condition can be written as:

$$TaJ_m'(Ta) + \frac{\gamma_2}{\gamma_1} mJ_m(Ta) = 0 \qquad (2.1.3)$$

where $\gamma_1 = k^2 - \omega^2\mu_o\varepsilon_\perp$ and $\gamma_2 = \omega^2\mu_o\varepsilon_x$ , m = the poloidal mode number, $\varepsilon_\perp$ and $\varepsilon_x$ are the components of the dielectric tensor of the magnetized plasma.

The eigenmodes of the cavity are the simultaneous solutions of equations (2.1.1) and (2.1.3). Each of these dispersion solutions is identified by a set of mode numbers, ($\ell$,m,N), where $\ell$ is the radial mode number, m is the poloidal mode number, and N is the axial mode number. The poloidal mode number, m, is the integer order of the Bessel function in the solution (2.1.2). The axial mode number, N, is related to the axial component of the wave vector, k, by the periodic boundary condition in the axial direction. k = N/R, where N is an integer, and R is the major radius of the tokamak. The definition of the radial mode number, $\ell$, can be best described in an example. Consider the m = 0 modes, the boundary condition (2.1.3) can be written as

$$J_1(Ta) = 0$$

In this case the radial mode number is defined to be the order of the zeros of $J_1$. For instance, the lowest radial mode, $\ell$ = 1, corresponds to Ta = 3.83, the first zero of $J_1$, if $J_1(0) = 0$ is not included. (In waveguide theory it is customary to denote the radial component of the wave vector by $T_{\ell m}$ corresponding to the ($\ell$,m) mode. In the above case, for instance, $T_{10}a = 3.83$).

For m $\neq$ 0 modes the solution is more involved because of the transcendental nature of equation (2.1.3). Once the values of the independent variables (the density, the poloidal mode number m, and the axial mode

number, N) are imposed, Newton's method for solving a system of equations is used to find the solutions of the input frequency and the radial component of wave vector, T, which simultaneously satisfy both equations (2.1.1) and (2.1.3). For a given set of values for independent variables, there are an infinite number of discrete solutions for the frequency and T. Therefore, the radial mode number is picked in the solution by the initial guesses for T and the frequency used in the Newton method.

Two sets of cavity mode dispersion curves are shown in Figures 2.2 and 2.3. Figure 2.2 shows the various poloidal and axial modes of the magnetosonic cavity wave for the lowest radial mode. Figure 2.3 shows the various radial and axial modes for the m = 0 poloidal mode. From Figure 2.3 one can see that for the parameters in our experiment, i.e., density less than $7 \times 10^{12}$ particles per $cm^3$ and $\omega/\omega_{ci}$ less than 3, the higher radial modes for the m = 0 poloidal mode are not excited. The spacings between the various modes with different radial mode number in the frequency versus density plot are large, so in our experiment only modes with the lowest radial mode number are excited. Therefore, only modes with the lowest radial mode number are used to compare with the experimental data (Figure 5.2).

Simplifications to the dispersion relation in equation (2.1.1) can be made under certain conditions for various modes as an aid to estimating some of the measured physical quantities. For instance, the cut-off relation, i.e., k = 0, for the various modes is very useful both as a guide to the general trends of the dispersion curves in the density

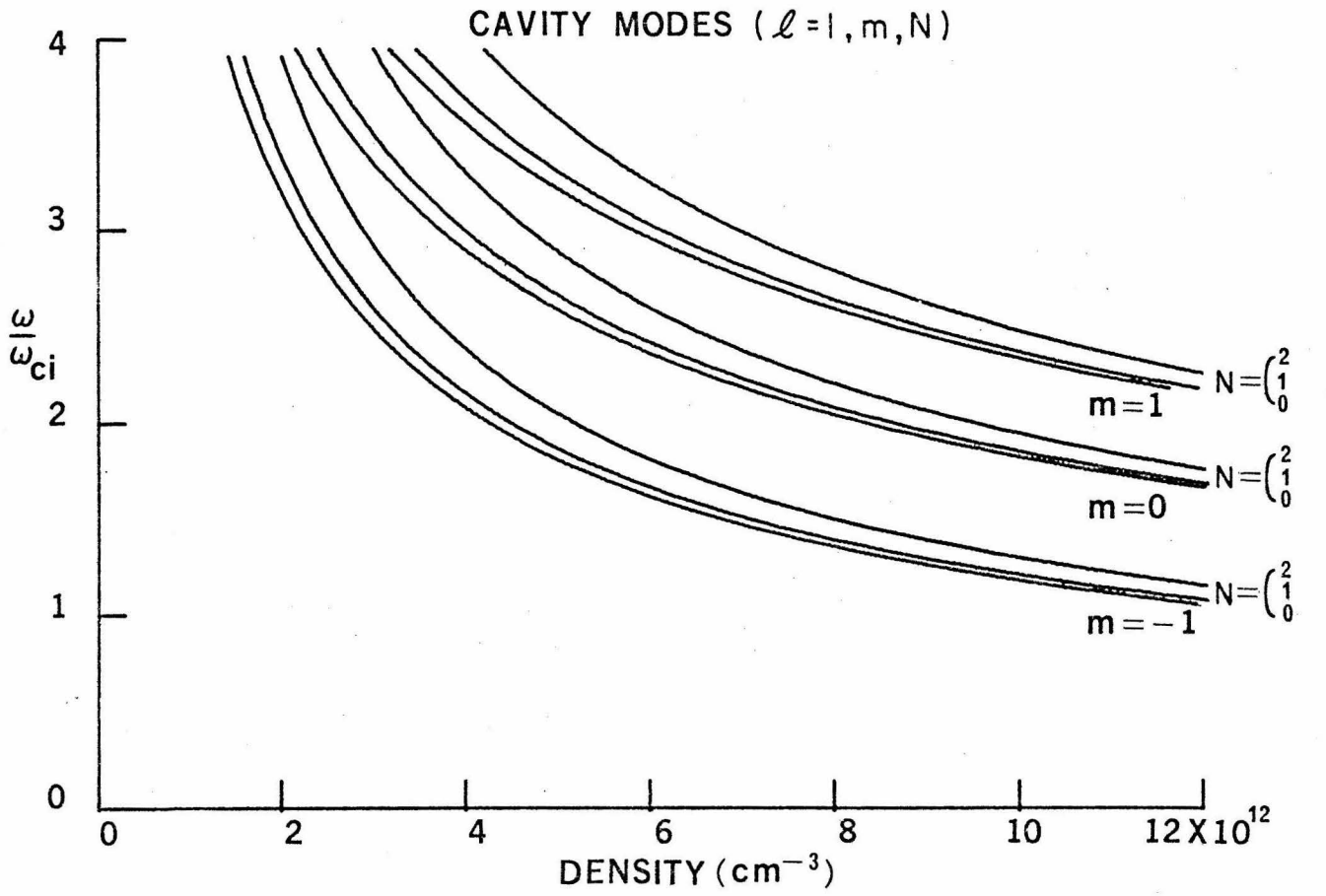


Figure 2.2

Dispersion curves of the magnetosonic cavity modes in a cold uniform cylindrical plasma filled cavity with conducting walls. $\ell$ = the radial mode number, m = the poloidal mode number, and N = the toroidal mode number. Theses are the lowest radial modes ($\ell$ = 1). For hydrogen plasma, with R=.45 m and a=.15 m.

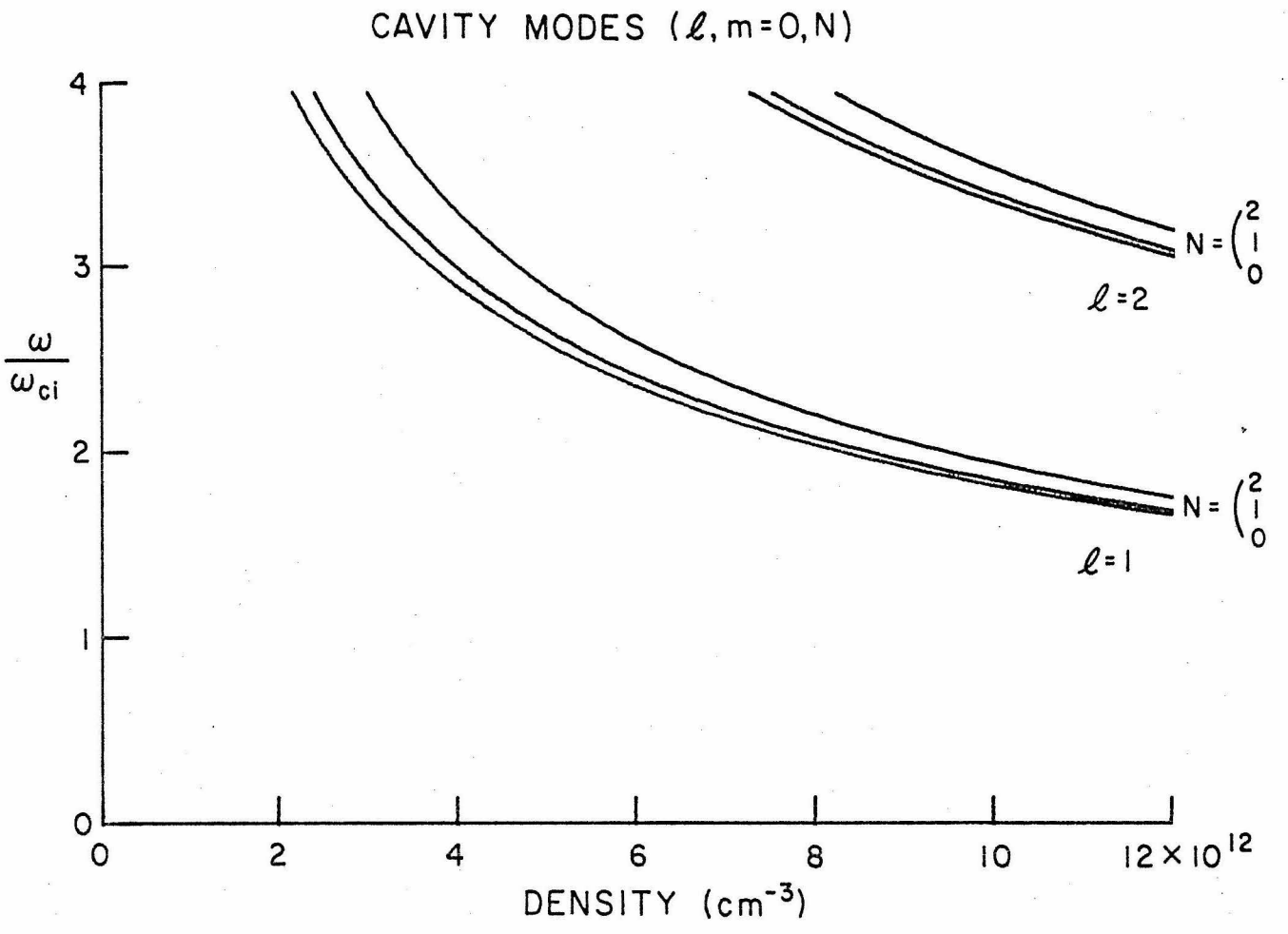


Figure 2.3

Dispersion curves of various radial and toroidal modes for m = 0.

Definitions and parameters same as in Fig. 2.2.

versus frequency plane, and in the estimation of the cavity Q. The cut-off relation will be estimated for modes in two frequency ranges. First, consider $\omega << \omega_{ci} << \omega_{ce}$. The dispersion relation (2.1.1) with k = 0 can be written as follows:

$$\frac{\Omega_i^2}{V_A^2}\frac{\omega_{ci}^2}{(1-\Omega_i^2)} - \frac{T^2}{2} - \sqrt{\left(\frac{T^2}{2}\right)^2 + \left(\frac{\Omega_i^3\,\omega_{ci}^2}{(1-\Omega_i^2)}\right)^2} = 0 \qquad (2.1.4)$$

where $V_A = B_o/\sqrt{\mu_o m_i n_i}$ is the Alfven velocity. For the approximation that $\Omega_i << 1$, the result is

$$T^2 \simeq \Omega_i^2\omega_{ci}^2/\,V_A^2$$

If the hydrogen plasma is assumed to be fully ionized, then the electron number density $n_e$ is equal to the ion number density $n_i$. The relation between resonant frequency of a given mode and electron density is

$$f \simeq A_{\ell mo}/\sqrt{n_e} \qquad (2.1.5)$$

where $A_{\ell mo}$ is a constant, and $\ell$,m are the corresponding radial and poloidal mode numbers.

Next, consider the region where $\Omega_i$ is near one. Then $T^2/2 << (\Omega_i^3\omega_{ci}^2)/[V_A^2(1-\Omega_i^2)]$ for the lower T modes. Therefore, equation (2.1.1) can be reduced to

$$\frac{\Omega_i^2}{V_A^2}\frac{\omega_{ci}^2}{(1-\Omega_i^2)} - \frac{T^2}{2} - \frac{\Omega_i^3\,\omega_{ci}^2}{V_A^2(1-\Omega_i^2)} \simeq 0$$

$$\frac{T^2}{2} \simeq \frac{\Omega_i^2}{V_A^2}\frac{\omega_{ci}^2(1-\Omega_i)}{(1-\Omega_i)(1+\Omega_i)}$$

$$T^2 \simeq \omega^2/V_A^2$$

which is the same as equation (2.1.4). Since the cut-off relation is continuous for the frequency range between $\Omega_i = 1$ and $\Omega_i = 3$, equation (2.1.4) should be a fairly good approximation for our purpose.

## 2.2 Summary of More Sophisticated Theories of Magnetosonic Cavity Modes

The theory presented here is a great simplification of the experimental conditions. Many physical conditions, such as the toroidal geometry, density, and magnetic field gradients, finite plasma temperature, and finite conductivity of the tokamak wall, have all been neglected. Therefore, this theory cannot predict all the effects of the cavity modes, but only can give the general features of the cavity resonances. There have been several theories developed by different groups, each including some of the neglected effects. Perkins, Chance, and Kindel have included the finite temperature effects and predicted damping of the magnetosonic wave by cyclotron damping at both the ion cyclotron frequency and twice the ion cyclotron frequency, and by electron transit time damping when the thermal velocity of the electrons is close to the phase velocity of the wave. They have also calculated the damping due to the finite conductivity of the tokamak wall [4].

As mentioned in the introduction, the effects of the poloidal field on the cavity modes were first suggested by Chance and Perkins [8], and later worked out in more detail by J. Adam and J. Jacquinot [12]. The poloidal field splits the toroidal mode degeneracy of the m = -1 poloidal modes. In other words, when the poloidal field is included in the calculation, the dispersion curves for the m = -1 modes with positive and negative toroidal mode number, N, are different from each other. The

experimental result is the splitting of the cavity modes. We observed some modes in our experiments had double peaks; however, no definite conclusion can be drawn because of two difficulties. First, there was not an independent mode identification measurement, other than using density information to correlate with theory, as to which modes should appear at a given time in the plasma discharge. Second, the plasma density decays bery quickly during the first two milliseconds in the discharge (see Section 3.1 for detailed explanations), and so the cavity modes are swept through very fast. Consequently, it is hard to tell the difference between a mode splitting and two different modes appearing very close to each other in time.

The effects of radial density profile on the cavity modes were studies by Paoloni [18,19]. The first model used in the theory was a cylindrical cavity with a vacuum layer between a uniform plasma and the conducting wall. The $m = 0, \pm 1$ modes were studies (where the fields vary as $e^{jm\theta}$), and the conclusion was that for the magnetosonic wave the $m = 0$ and $m = -1$ modes each has a definite cut-off frequency; however, for a sufficiently thick layer of vacuum, the $m = -1$ mode has no cutoff. In our experiments the cavity modes disappear when the input frequency is below 7 MHz. This does not necessarily mean that the $m = 1$ mode does not propagate below 7 MHz. Perhaps the transmitting antenna used here does not couple strongly to this mode at low frequencies. It is also possible that the vacuum layer in our tokamak has not reached the thickness requirement of the theory.

The second model used in the theory was a cylindrical cavity with a non-uniform radial density profile [19]. It was found that the radial variation of the wave fields depended on the assumed radial density profile. For the low radial and poloidal modes, the fields at the outer radius of the cylinder are much smaller in the case of the parabolic profile than in a uniform plasma, where the parabolic and uniform profiles have the same line-average density. This means that if a loop antenna is placed at the outer radius of the cylindrical cavity, the antenna coupling to the cavity modes is weaker for the parabolic density profile because of the lower field linkage compared to a uniform density profile.

The effect of the finite conductivity in the tokamak chamber wall is an important factor in the wave heating. As indicated in the summary of r.f. heating by Stix [3], the eddy current dissipation in the tokamak wall competes with the wave absorption processes in the plasma. In Appendix c, the losses in the stainless steel wall of the Caltech tokamak have been estimated in terms of the quality factor, Q, of the tokamak cavity for the $\ell = 1$, $m = 0$, and $k = 0$ mode. The quality factor Q is defined as

$$Q = 2\pi \frac{\text{energy stored}}{\text{energy lost per cycle}}$$

The estimated Q for the particular mode in Appendix c is a lower limit for the Q for the various other cavity modes. When the estimated Q due to wall loss is compared with the cavity Q measured in the experiment, the estimated Q is two to three times the measured Q, indicating the absorption processes in the plasma are comparable or higher than the

dissipation in the wall (Section 5.4). Therefore, a large part of the input r.f. energy should be absorbed by the plasma.

2.3 Circuit Model of the Antenna-Cavity Coupling:

For a cavity filled with a linear scalar dielectric, the amplitudes of the various cavity modes can be described by a set of equations derived from the Maxwell's equations and the boundary conditions at the cavity walls. This set of equation is the same as those for an R-L-C electric circuit; hence the cavity can be modelled by an equivalent resonance circuit [20]. The use of the circuit model of a cavity is only for the convenience of those who have good intuition about the behavior of electrical circuits. To justify the use of a simple R-L-C resonance circuit to represent a cavity filled with a magnetized plasma would be a very involved task. Therefore, we shall summarize the approach used by Slater [21] to justify the modelling of a linear scalar dielectric filled microwave cavity by a R-L-C circuit, and assume that a similar derivation can be carried out for a linear tensor dielectric in a cavity. The validity of the circuit representation of the tokamak can be tested when the experimental results are compared with the model.

The electromagnetic fields in the cavity can be expressed in terms of a set of complete orthonormal functions, called the normal modes of the cavity: $\{\underline{E}_\ell + \underline{F}_\ell\}$ and $\{\underline{H}_\ell\}$ where $\nabla\cdot\underline{E}_\ell = 0$, $\nabla\cdot\underline{H}_\ell = 0$, $\nabla\times\underline{F}_\ell = 0$. The orthonormal conditions are expressed as follows:

$$\int_V \underline{E}_\ell \cdot \underline{E}_m \, dV = \delta_{\ell m}$$

$$\int_V \underline{F}_\ell \cdot \underline{F}_m \, dV = \delta_{\ell m}$$

$$\int_V \underline{H}_\ell \cdot \underline{H}_m \, dV = \delta_{\ell m}$$

where V is the cavity volume. These normal modes are the solutions of the wave equation,

$$\nabla^2 \underline{E}_\ell + k_\ell^2 \underline{E}_\ell = 0$$
$$\nabla^2 \underline{H}_\ell + k_\ell^2 \underline{H}_\ell = 0$$

and
$$k_\ell \underline{F} = \nabla \psi_\ell$$
$$\nabla^2 \psi_\ell + k_\ell^2 \psi_\ell = 0$$

Associated with each of the eigenmodes is a characteristic angular resonance frequency, $\omega_\ell$ , which can be related to the wave number by $k_\ell^2 = \varepsilon\mu\omega_\ell^2$. The fields in the cavity can be expanded in terms of the normal modes with the following coefficients: $E_\ell = \int_V \underline{E}\cdot\underline{E}_\ell dV$, $H_\ell = \int_V \underline{H}\cdot\underline{H}_\ell dV$, $F_\ell = \int_V \underline{E}\cdot\underline{F}_\ell dV$

$$\underline{E} = \sum_\ell (E_\ell \underline{E}_\ell + F_\ell \underline{F}_\ell) \qquad (2.3.1)$$

$$\underline{H} = \sum_\ell H_\ell \underline{H}_\ell \qquad (2.3.2)$$

The solutions of the fields must satify both the Maxwell's equations and the boundary conditions. There are two types of boundaries in the problem: conducting surfaces, denoted by S, and insulating surfaces, denoted by S'. The boundary conditions are

$$\underline{n} \times \underline{E}_\ell = 0 \quad \text{and} \quad \underline{n}\cdot\underline{H}_\ell = 0 \qquad (2.3.3)$$

at a perfectly conducting surface, S, and

$$\underline{n} \times \underline{H}_\ell = 0 \quad \text{and} \quad \underline{n}\cdot\underline{E}_\ell = 0 \qquad (2.3.4)$$

at a perfectly insulating surface S'. As shown by Slater, if equations (2.3.1) and (2.3.2) are substituted into the Maxwell's equations, the resulting integro-differential equations for the expansion coefficients are as follows:

$$(\varepsilon\mu\frac{d^2}{dt^2} + k_\ell^2)\, E_\ell = -\mu \frac{d}{dt}[\int \underline{J}\cdot\underline{E}_\ell \, dV - \int_{S'} (\underline{n}x\underline{H})\cdot\underline{E}_\ell \, da] - k_\ell \int_S (\underline{n}x\underline{E})\cdot\underline{H}_\ell \, da \qquad (2.3.5)$$

$$(\varepsilon\mu\frac{d^2}{dt^2} + k_\ell^2)\, H_\ell = -k_\ell[\int \underline{J}\cdot\underline{E}_\ell \, dV - \int_{S'} (\underline{n}x\underline{H})\cdot\underline{E}_\ell \, da] - \varepsilon \frac{d}{dt} \int_S (\underline{n}x\underline{E})\cdot\underline{H}_\ell \, da \qquad (2.3.6)$$

These are the differential equations for simple harmonic motion (terms on the left-hand side) with dampings and external forces(terms on the right-hand side). The convenience of these equations is that the boundary conditions at S or S' can be readily substituted into the equations. To demonstrate the damping terms, consider a cavity filled with a lossy dielectric represented by a finite conductivity, $\underline{J} = \sigma\underline{E}$. Equation (2.3.5) becomes

$$(\varepsilon\mu\frac{d^2}{dt^2} + \sigma\mu\frac{d}{dt} + k_\ell^2)\, E_\ell = 0$$

When the time dependence of $E_\ell$ is taken to be $e^{j\omega t}$, the following solution for $\omega$ is obtained

$$\omega = \pm\omega_\ell\sqrt{1 - (1/2Q)^2} + j\omega_\ell/2Q \,, \quad \text{where } Q = \varepsilon\omega_\ell/\sigma$$

This equation is analogous to a R-L-C circuit if the following equivalent circuit parameters are used [22]

$$L_\ell = \mu k_\ell^2 V$$
$$C_\ell = \varepsilon/(k_\ell^4 V)$$
$$R_\ell = \sigma\mu k_\ell^2 V/\varepsilon$$

The losses due to the finite conductivity of the cavity wall can be included by substituting the boundary condition on the conducting surface S, $\underline{n}x\underline{E} = \underline{H}(1 + j)\sqrt{\omega\mu/2\sigma}$, into the surface integral over S in equation 2.3.6. The effects of the wall loss in the tokamak are discussed in

Appendix c.

Next let us find the input impedance of cavity using equations (2.3.5) and the proper boundary condition. Consider a cavity coupled to an outside system by a waveguide or coaxial line. The input impedance of the cavity can be obtained from the fields at an insulating surface, S', parallel to the cross section of the transmission line near the input of the cavity. As shown by Slater, once the boundary conditions of equation (2.3.4) are imposed, the fields at S' can be expanded in terms of the transverse components of the normal modes of the wave guide, $\underline{E}_{tn}$ and $\underline{H}_{tn}$, i.e.

$$\underline{E} = \sum_n v_{\ell n}\, \underline{E}_{tn} \qquad \underline{H} = \sum_n i_n Z_{1n} \underline{H}_{tn}$$

where $v_{\ell n}$'s are the time independent expansion coefficients of the electric field, $i_n$ are the coefficients of the magnetic field, and $Z_{1n}$ is the characteristic impedance of the wave guide for the $n^{th}$ mode. After some manipulations the surface integral of equation (2.3.5) can be related to the expansion coefficients

$$\int_{S'} (\underline{n} \times \underline{H}) \cdot \underline{E}_\ell \, da = \sum_n i_n v_{\ell n}$$

When the above integral is substituted into equation (2.3.5), the following solution of the expansion coefficients of the electric field, $E_\ell$, is obtained

$$E_\ell = \sum_n (i_n\, v_{\ell n}/\omega\varepsilon)/j[1 - (\omega_\ell^2 / \omega^2)]$$

$$\underline{E} = \sum_n V_n E_{tn} \quad \text{(the transverse electric field at S')}$$

where

$$V_n = \sum_m i_m Z_{nm}$$

$$Z_{nm} = \sum_\ell \frac{v_{\ell n} v_{\ell m}/\varepsilon\omega_\ell}{j[1 - (\omega_\ell^2 / \omega^2)]}$$

The quantities $i_n$ and $V_n$ can be interpreted as the 'current' and the 'voltage' of the $n^{th}$ mode of the wave guide. $Z_{nm}$ are the impedance coefficients of the various modes in the wave guide. If only one mode, say the $i^{th}$ mode, in the wave guide is dominating, and loss terms, such as dielectric and wall losses, are introduced into equations (2.3.5) and (2.3.6) the resultant cavity input impedance is as follows:

$$Z_{ii} = \sum_{\ell} \frac{(\nu_{\ell i}^2/\varepsilon\omega_\ell)}{j[1 - (\omega_\ell^2/\omega^2)] + 1/Q_\ell}$$

where $1/Q_\ell = 1/Q_{wall} + 1/Q_{dielectric}$. This is just the equation satisfied by the input impedance of a R-L-C resonance circuit if the following analogies are made:

$$\omega_\ell^2 = 1/L_\ell C_\ell \quad \text{and} \quad R_\ell = Q_\ell/\omega_\ell L_\ell$$

where $L_\ell$, $C_\ell$, and $R_\ell$ are the equivalent circuit parameters of the $\ell^{th}$ cavity mode. $\nu_{\ell i}^2$ represents the coupling between the wave guide and the cavity. In our experiment, the cavity is coupled to the outside system by a loop antenna which is modelled by a transformer with a certain mutual inductance, $M_\ell$, to the $\ell^{th}$ cavity mode; thus, we can make the following analogy between the coupling coefficient $\nu_{\ell i}^2$ and $M_\ell^2$ for high Q cavities, i.e., $\omega \sim \omega_\ell$, [23]

$$M_\ell^2/L_\ell = \nu_{\ell i}^2/\varepsilon\omega_\ell^2$$

The equivalent circuit of the antenna-cavity system is shown in Figure 2.4. Each of the eigenmodes is denoted by a subscript, for example, $R_{p_i}$, $L_{p_i}$, and $C_{p_i}$ are the equivalent circuit elements of the $i^{th}$ mode. The subscript 'p' denotes that the cavity is filled with a magnetized plasma. Unlike the simple microwave cavity where the circuit elements can be calculated theoretically, the equivalent circuit elements

of the tokamak are more difficult to calculate and have not actually been computed. Since the physical quantities measured in the experiments are not the circuit elements themselves, but rather functions of these circuit elements, such as the Q of the cavity and the resonance frequency, only the measurable quantities need to be calculated. In particular, one would like to know whether the complex input impedance of the antenna-tokamak system satisfies the form of the complex input impedance function derived from the equivalent circuit model.

By using this model, one can get an expression for the input impedance of the antenna, $Z_L$, when the various eigenmodes impedances are reflected into the primary of the transformer. The contribution to $Z_L$ from the each of the R-L-C circuits is a simulation of the plasma loading. For the circuit shown in Figure 2.4, $Z_L$ can be written as follows:

$$Z_L = R_{ant} + j\omega L_{ant} + \sum_i (\omega M_i)^2 / [R_{p_i} + j(\omega L_{p_i} - \frac{1}{\omega C_{p_i}})] \qquad (2.3.7)$$

where $R_{ant}$ and $L_{ant}$ are the resistance and inductance of the antenna. For the convenience of comparison with experimental results, it is desirable to rewrite equation (2.3.7) in terms of the following quantities which are measured in the experiments.

$$Q_{p_i} = \omega_i L_{p_i} / R_{p_i}$$

$$\omega_i^2 = 1/L_{p_i} C_{p_i}$$

$$Q_a = \omega L_{ant} / R_{ant}$$

Two dimensionless quantities are used for convenience, the coupling coefficient, $\kappa_i$, and the normalized frequency, $\Omega_{p_i}$,

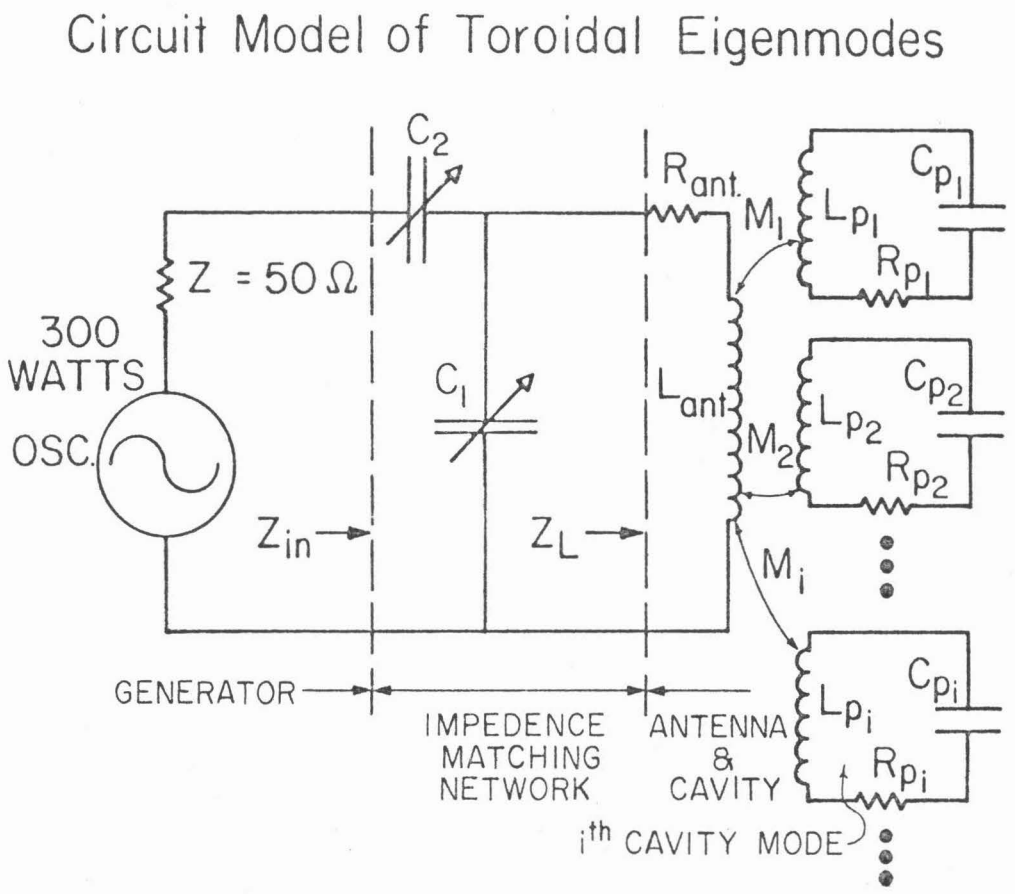


Figure 2.4

Cirduit model of the antenna-cavity coupling. Each cavity mode is represented by a R-L-C resonance circuit. $M_i$ is the mutual inductance between the antenna and the $i^{th}$ cavity mode.

$$\kappa_i^2 = M_i^2/L_{p_i} L_{ant}$$

$$\Omega_{p_i} = \omega_i/\omega$$

The real and imaginary parts of $Z_L$ can be expressed in terms of these parameters:

$$R_L = R_{ant}[1 + \sum_i \frac{Q_a \kappa_i^2 Q_{p_i} \Omega_{p_i}}{\Omega_{p_i}^2 + Q_{p_i}^2 (1 - \Omega_{p_i}^2)^2}] \qquad (2.3.8)$$

$$X_L = X_{ant}[1 - \sum_i \frac{(1 - \Omega_{p_i}^2) \kappa_i^2 Q_{p_i}^2}{\Omega_{p_i}^2 + Q_{p_i}^2 (1 - \Omega_{p_i}^2)^2}] \qquad (2.3.9)$$

Near the resonance of the $j^{th}$ cavity mode, equations (2.3.8) and (2.3.9) can be approximated as

$$R_L \simeq R_{ant} + M_j^2 \omega_j^2 / R_{p_j} \qquad (2.3.8a)$$

$$X_L \simeq X_{ant}[1 - \sum_{i \neq j} \frac{(1 - \Omega_{p_i}^2) \kappa_i^2 Q_{p_i}^2}{\Omega_{p_i}^2 + Q_{p_i}^2 (1 - \Omega_{p_i}^2)^2}] \qquad (2.3.9a)$$

At a particular frequency, only the term with a resonance frequency closest to the applied frequency will dominate the resistive loading, whereas the reactance depends on the coupling coefficient and Q of all the other modes. Depending on magnitudes of the contribution to the input reactance from the modes above and below the resonance frequency, i.e. $\Omega > 1$ or $\Omega < 1$, the total reactance from all the cavity modes, $X_L - X_{ant}$, can be greater or less than zero. If the reactance contribution from modes with resonant frequency, $\omega_j < \omega_i$, is greater than the contribution from the other modes, for instance, the input reactance, $X_L$, will show an increase to the basic antenna inductive reactance from the effects of the cavity modes.

## 2.4 Transient Measurements of Steady State Quantities

The impedance measurements made in our experiment are transient measurements. The tokamak operates in a pulse mode with the duration of the plasma current about 12 milliseconds. Furthermore, as mentioned in the introduction, the cavity eigenmodes are swept through very rapidly due to the changing plasma density. (This point will be detailed in Section 4.2). Therefore, the input impedance of the cavity modes is changing in a very short time. However, the concept of impedance is defined for a steady state situation, and so it is appropriate at this point to examine the conditions under which the impedance concept is valid. To get an estimate of how long one must wait to achieve steady state condition in a transient measurement, consider the following idealized problem. A R-L-C resonance circuit for one of the eigenmodes is subjected to a step of r.f. voltage input at the resonance frequency, $\omega_o$, of the circuit. The voltage-current relationship can be written in the following integro-differential equation:

$$L \frac{dI}{dt} + IR + \frac{1}{C} \int_0^t I \, dt = V_o e^{j\omega_o t} U(t) \qquad (2.4.1)$$

where

$$U(t) = \begin{cases} 0 & t < 0 \\ 1 & t > 0 \end{cases}$$

The equation can also be expressed in the following form:

$$L \frac{d^2I}{dt^2} + R \frac{dI}{dt} + \frac{1}{C} I = V_o \, j\omega_o \, e^{j\omega_o t} U(t) \qquad (2.4.2)$$

First, the homogeneous solution to the differential equation is found using Laplace's transform

$$s^2 + (R/L)s + 1/LC = 0$$

and so the solution of the form $I_0 e^{st}$ can be written as

$$s = -(\omega_0/2Q) \pm j\omega_0 \sqrt{1 - (1/2Q)^2} \qquad (2.4.3)$$

where $\omega_0^2 = 1/LC$, and $Q = \omega_0 L/R$. In our case the Q is very high and so the imaginary term is approximately equal to $\pm\omega_0$.

In the high Q approximation, the general solution to equation (2.2.5) can be written as follows:

$$I = (V_0/R)(1 - e^{-\omega_0 t/2Q}) e^{j\omega_0 t} \qquad (2.4.4)$$

From this equation one can see that the time required for the circuit to reach steady state is 2 to 3 times $2Q/\omega_0$. Thus the time, T, to sweep through the half power points of the resonance must be longer than $2Q/\omega_0$. The longer T is compared to $2Q/\omega_0$, the more accurately the steady state impedance can be measured. The condition for accurate impedance measurement is

$$T >> 2Q/\omega_0 \qquad (2.4.5)$$

Fortunately, the density decay is slow enough for this condition to be satisfied in our experiments. In Section 5.6, equation (2.4.5) will be applied to the experimental data and the validity of the impedance measurements will be discussed.

## 2.5 Impedance Matching

The impedance matching network, consisting of the two tuning capacitors, $C_1$ and $C_2$ in Figure 2.4, is used to tune out the imaginary part of the impedance in the antenna circuit, and to transform the real part of the impedance to 50 ohms. For a particular setting of $C_1$ and $C_2$, only one value of $L_{ant}$ and $R_{ant}$ can be matched to 50 ohms. Therefore, one must be specific as to the condition under which the antenna is matched. The most simple way to match the antenna is in vacuum when no plasma is present. However, it is found that once the plasma is formed around the antenna, the antenna then becomes mismatched. Even when there are no cavity resonances present during the discharge, the plasma causes a sufficient change in impedance to the antenna that retuning $C_1$ and $C_2$ is needed. This kind of tuning will be denoted as "off-resonance" matching. A precise definition of the "off-resonance" matching is to match the generator impedance at a specific time in the plasma discharge, when no cavity mode is resonant. The reason for specifying the time in the discharge is that the plasma condition is changing as a function of time, and so the impedance contributed from the plasma when no cavity resonance is present is also changing as a function of time. From now on the sum of the "off-resonance" plasma impedance plus the antenna impedance will be denoted by $Z_{off} = R_{off} + jX_{off}$. It is found from the experiments that the changes in $Z_{off}$ resulting from the changes in the plasma conditions are slow enough that "off-resonance" matching for fairly long periods in the discharge (typically 3 milliseconds) is possible. In this way, one setting of $C_1$ and $C_2$ can ensure that the generator is properly "off-resonance"

matched for the first two milliseconds in the plasma discharge where most of the cavity modes appear.

There is one more type of matching, namely to match the generator impedance to the impedance of the antenna plus the added contribution from the plasma at one of the resonance peaks. Because the impedance contribution from each of the eigenmodes is different from the others, only one mode can be properly matched for a particular setting of $C_1$ and $C_2$. The details of this type of tuning are discussed in Section 4.5. For future reference, the term "on-resonance" matching is coined to denote this type of matching.

In the experiment, the directional coupler used has a characteristic impedance of 50 ohms, and it measures the impedance of the antenna and the plasma loading after being transformed through the matching network. This measured impedance is the term $Z_{in}$ shown in Figure 2.4. The quantity of interest is the impedance looking directly into the antenna, i.e., $Z_L$ (see Figure 2.4). The transformation relating these two impedances is readily shown to be

$$R_L = R_{in} X_{C_1}^2 / D \tag{2.5.1}$$

$$X_L = X_{C_1}\left[1 - \frac{X_{C_1}(X_{C_1} + X_{C_2} + X_{in})}{D}\right] \tag{2.5.2}$$

where $D = (X_{C_1} + X_{C_2} + X_{in})^2 + R_{in}^2$ and $X_{C_1} = 1/\omega C_1$, $X_{C_2} = 1/\omega C_2$.

The ideal matching procedure for "on-resonance" matching is first to match the impedance of the generator at the "off-resonance" condition, which is an easier process than "on-resonance" matching. From the measured

complex reflection coefficient $\rho$, $Z_L$ can be calculated. From the values of $Z_L$ at the resonance peaks, the $X_{C_1}$ and $X_{C_2}$ can be calculated for "on-resonance" matching, i.e., $R_{in} = 50$ ohms, $X_{in} = 0$. This procedure was not followed in this thesis because of the lack of an on-line computer system to calculate $Z_L$ and the new $C_1$ and $C_2$. The actual "on-resonance" matching reported in this thesis was done by minimizing the reflected voltage from the directional coupler at one of the modes through trial and error. More discussions on "resonance" matching and data of impedance at "on-resonance" matching are presented in Section 5.7.

## 2.6 Relations between Circuit Parameters

The actual physical quantities that are measured in the experiment are the amplitude and the phase of the incident and reflected voltages into the matching network from the generator, the antenna current, and the plasma density. From these measured quantities, the following circuit parameters, shown in Figure 2.4, can be calculated: the input impedance $Z_{in}$, the resonance plasma loading resistance $M^2\omega_i^2/R_{pi}$, the cavity $Q, Q_{p_i}$, the coupling coefficient $\kappa$, and the antenna efficiency $\eta$.

To obtain the resistance information from the measured incident and reflected voltage into the antenna and the antenna current requires some basic equations used in transmission line theory. The incident and reflected waves into the capacitor matching network are measured by a r.f. directional coupler, which has a characteristic impedance of 50 ohms. Since the generator and the directional coupler is also 50 ohms, the incident and reflected power into the antenna circuit can be written as

$$P_{inc} = V_{inc}^2/50 \tag{2.6.1}$$

$$P_{ref} = V_{ref}^2/50 \tag{2.6.2}$$

where $P_{inc}$ and $P_{ref}$ are the incident and reflected powers, respectively. If we call the antenna current $I_a$, then the resistance can be obtained as

$$R = (P_{inc} - P_{ref})/I_a^2 \tag{2.6.3}$$

To find the complex input impedance, first define the complex reflection coefficient. The complex reflection coefficient, $\rho$, can be related to the amplitude and the phase of the incident and reflected voltages as

$$\rho = (V_{ref}/V_{inc})\, e^{j\phi} \tag{2.6.4}$$

where $\phi$ is the phase between the incident and the reflected voltages [24]. The complex input impedance can be obtained from the complex reflection coefficient by the following transformation:

$$Z_{in} = Z_o[(1+\rho)/(1-\rho)] \tag{2.6.5}$$

where $Z_{in} = R_{in} + jX_{in}$, and $Z_o$ is the characteristic impedance of the transmission line, i.e., $Z_o = 50$ ohms for our experiment. Using this formula to solve for $R_{in}$ and $X_{in}$ for our case, the following equations are obtained:

$$R_{in} = Z_o[(1-|\rho|^2)/(1 - 2|\rho|\cos\phi + |\rho|^2)] \tag{2.6.6}$$

$$X_{in} = Z_o[2|\rho|\sin\phi/(1 - 2|\rho|\cos\phi + |\rho|^2)] \tag{2.6.7}$$

where $|\rho|$ is the magnitude of the reflection coefficient. These two

equations are used in Sections 4.4 and 5.5 to calculate the complex impedance from the experimental data.

The cavity Q can be estimated from the plasma density at the cavity resonance, the rate of density change as a function of time, and the 3 dB time width of the resonance peak. The reason density information can be used to get the cavity Q is because of the nature of the dispersion relation of the magnetosonic wave (Figure 2.2). As shown in Figure 2.2, a change in the density can be interpreted as a kind of frequency sweep in the cavity. During the plasma discharge, the density is changing as a function of time (Figure 3.2). In the experiments where the input frequency of the antenna is fixed, the cavity modes are swept through as a series of resonance peaks by the density decay. Thus, the cavity Q can be derived as a function of the plasma density. To demonstrate this point, examine the approximate cut-off relation, $k = 0$, for the modes. As shown in Section 2.1, equation (2.1.5) is a good approximation of the cut-off relation for the frequency range for our experiment, $\omega_{ci} < \omega < 3\omega_{ci}$. Restating equation (2.1.5):

$$f \simeq A_{\ell mo} / \sqrt{n_e}$$

The Q of the cavity can be written as

$$Q \equiv f_o / \Delta f_{3\ dB} \tag{2.6.8}$$

where $f_o$ = the cavity resonance frequency. Using the cut-off relation the Q can be related to the density as

$$Q \simeq 2n_e / \Delta n_{e\ 3\ dB}$$

Such a measurement gives the loaded Q of the cavity $Q_L$, rather than the

unloaded Q, $Q_o$, but the two are related as follows. Consider the relation between $Q_L$ and $Q_o$ of an "off-resonance" matched antenna. When the system is "off-resonance" matched, $C_1$ and $C_2$ are chosen so that $Z_{in}$ looks like 50 ohms during the plasma discharge when no cavity resonance is present, i.e., when $Z_L = Z_{off}$. $Z_{off}$ is the "off-resonance" impedance defined in Section 2.5. Because the tuning is off resonance, $Z_L$ looks like 50 ohms when transformed through $C_1$ and $C_2$. By the same token, the generator impedance, which is 50 ohms, looks like the complex conjugate of $Z_{off}$ (i.e., $R_{off} - jX_{off}$), when transformed back through $C_1$ and $C_2$. Finally, when the generator impedance is transferred through the antenna into the resonance circuit of the $i^{th}$ eigenmode, an additional resistance of $M^2\omega^2/R_{off}$ is in the R-L-C circuit. This additional resistance, as shown in Figure 2.5c, will add in series with the $R_p$, thus lowering the Q of the cavity. From the resonance circuit shown in Figure 2.5c, one can write the loaded cavity Q as follows:

$$Q_L = L_p \omega/R_p \left(1 + \omega^2 M^2/2R_{off}R_p\right) \qquad (2.6.10)$$

Solving for $Q_o = \omega L_p/R_p$

$$Q_o = Q_L \left(1 + \omega^2 M^2/2R_{off}R_p\right) \qquad (2.6.11)$$

All the terms in this equation are known. $R_{off}$ is the antenna resistance plus the contribution from the plasma during the "off-resonance" condition. $\omega^2 M^2/R_p$ is the loading of the antenna due to the plasma at the peak of a resonance. Both of these can be determined by experiment.

Now the antenna coupling coefficient can be calculated for one of the cavity modes:

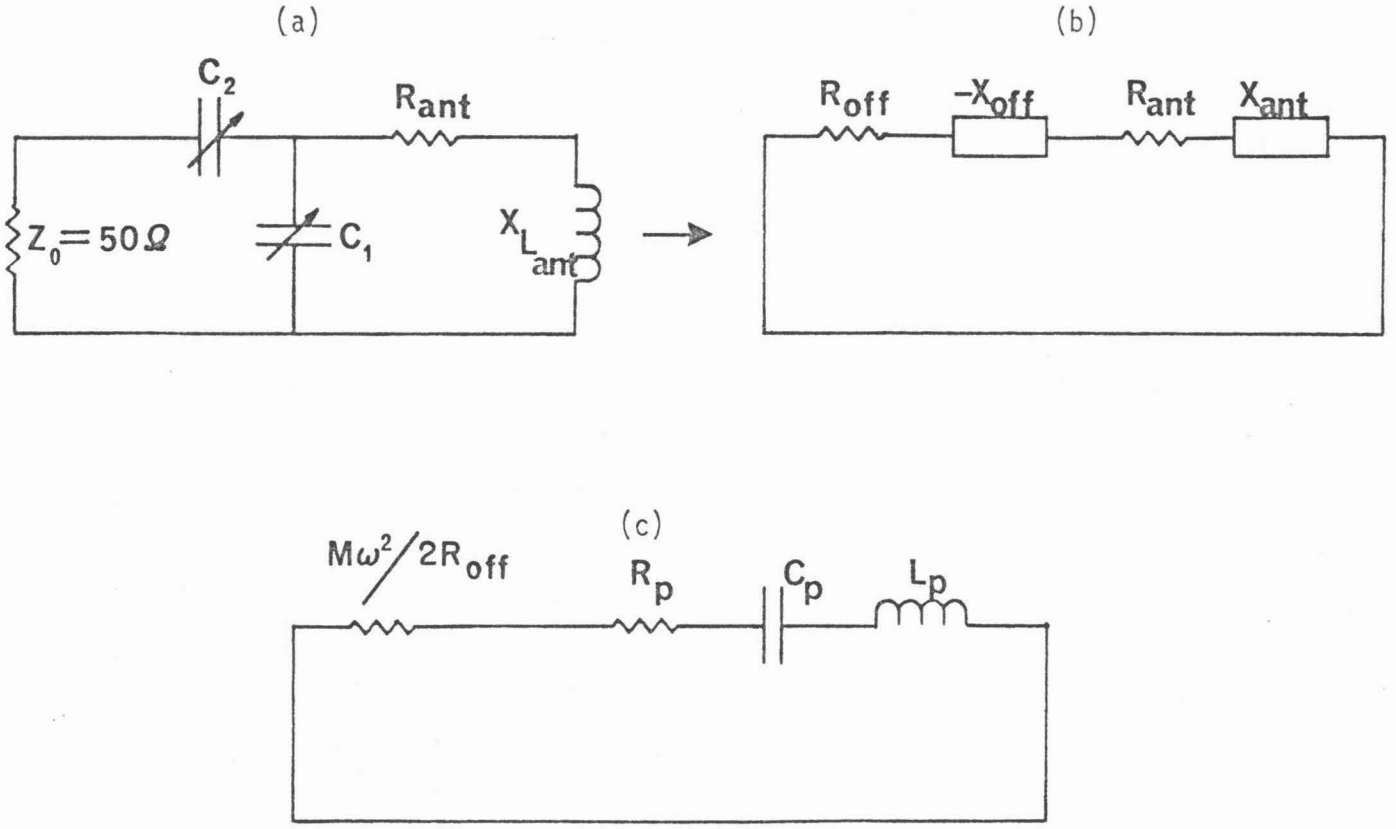


Figure 2.5

Circuit model relating the loaded Q and the unloaded Q. (a) is the equivalent circuit of the antenna, the matching network, and the generator impedance. (b) is the equivalent circuit looking back at the generator impedance through the matching network. (c) is the circuit in (b) transformed through the mutual inductance M into one of the cavity resonance circuits.

$$\kappa_i^2 = (R_L/R_{ant} - 1)/Q_{p_i} Q_a \qquad (2.6.12)$$

## 2.7 Antenna Efficiency

Another physical quantity of considerable interest is the efficiency of the transmitting antenna. The efficiency $\eta$ is defined as the amount of power coupled into the cavity, divided by the total power delivered to the antenna by the r.f. generator. $\eta$ can be obtained straightforwardly by considering the circuit in Figure 2.6. Here the plasma impedance has been transformed into the antenna circuit, and the current i flows in the loaded antenna. The settings on the matching capacitors determine the magnitude of the power delivered to the antenna, with the maximum power transfer when the impedances of both sides are matched. At a cavity resonance, the plasma loading impedance is real, and the value is $M^2\omega^2/R_p$. The only dissipative elements in the circuit are $R_{ant}$ and $M^2\omega^2/R_p$. Thus $\eta$ can be written as

$$\eta = \frac{i^2 M^2 \omega^2}{i^2 R_p [R_{ant} + (M^2\omega^2/R_p)]} \qquad (2.7.1)$$

It is more enlightening to write $\eta$ in terms of $\kappa$, $Q_a$, and $Q_p$

$$\eta = \frac{\kappa^2 Q_a Q_p}{1 + \kappa^2 Q_a Q_p} \qquad (2.7.2)$$

This equation is very useful in designing an efficient antenna system. After deciding on a particular antenna shape, this equation gives the directions for improving the efficiency. In Section 6.2 the designing problem will be discussed further.

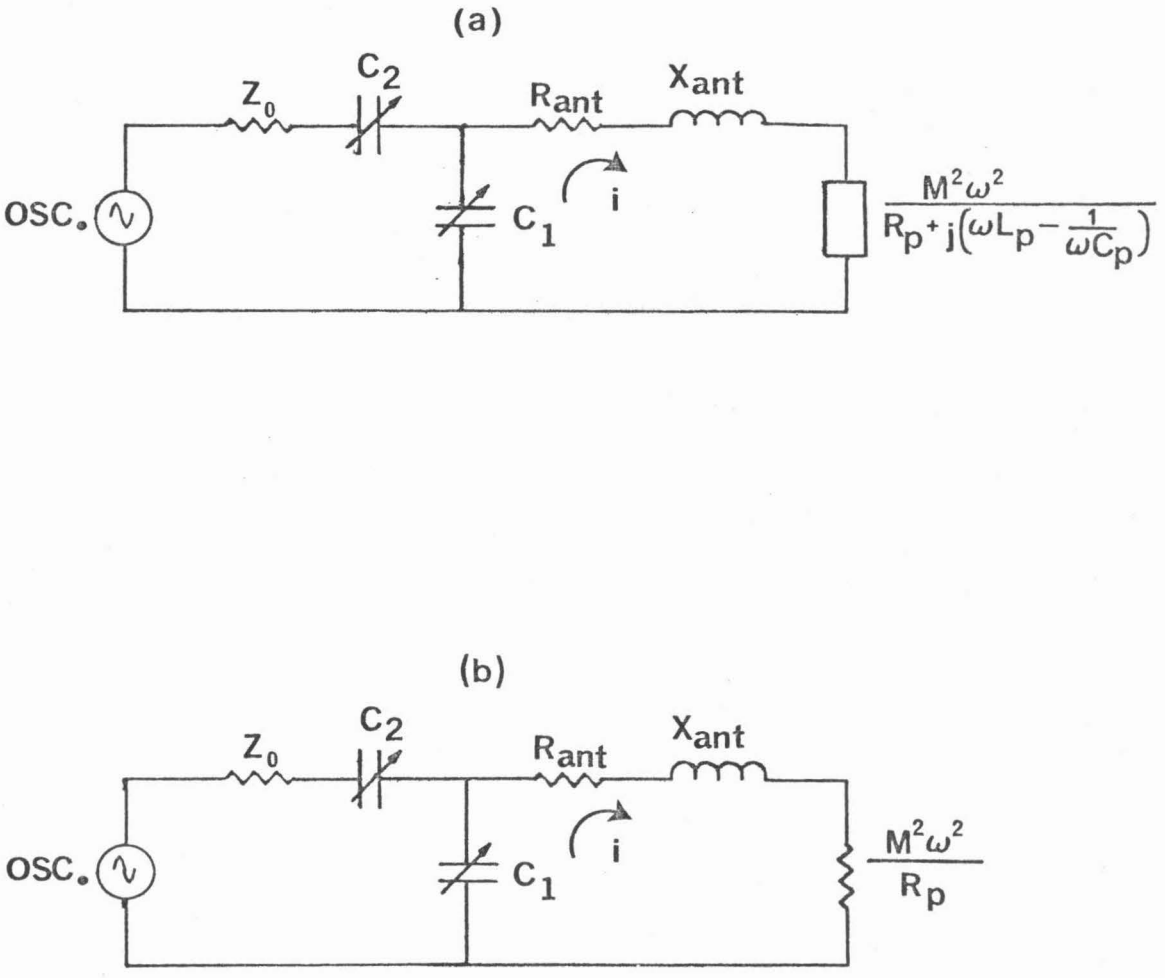


Figure 2.6

(a) Impedance of the RLC resonance circuit transforms through the mutual inductance M into the antenna circuit. i is the antenna current. $Z_o$ is the generator impedance. (b) At resonance, the transformed impedance is real and equal to $M^2\omega^2/R_p$. The antenna efficiency, $\eta$, is $\frac{M^2\omega^2}{R_p R_{ant} + M^2\omega^2}$.

## 2.8 Simulation of Cavity Resonances

It is useful to see what general effects the impedance function [equation (2.3.1)] will predict before actually discussing the experimental results. The essence of the discussion in Section 2.3 is that the form of the impedance function observed in the experiment should be reasonably close to the form of equation (2.3.1). The unknowns are the various circuit parameters, such as the antenna Q, the Q of the cavity modes, the antenna coupling coefficient $\kappa$, etc., and they can be measured experimentally. The values of the circuit parameters used in the simulation are either estimated from theoretical considerations, or measured in experiment.

The simulation starts with the equivalent R-L-C circuits for the resonance cavity. Since the cutoff relation of the eigenmodes is approximately $f \propto 1/\sqrt{n}$ and $\omega_{op} \propto 1/\sqrt{C_p}$, where $\omega_{op}$ is the resonance angular frequency of the R-L-C circuit, the change of the capacitor as a function of time is assumed to be proportional to the density. A typical set of density evolution data is fitted by a polynomial, $n = n(t)$, and the time dependence of the normalized frequency $\Omega_{p_i}$, is taken to be proportional to this density function, $n(t)$. The proportionality between the frequency, $\Omega_{p_i}$, and the density, $n(t)$, for the $i^{th}$ mode is such that when the resonance condition for the $i^{th}$ mode is satisfied at a certain density value, $\Omega_{p_i} = 1$. The density dependence of the cavity modes is computed from the simple cold plasma theory. Each of the cavity resonances is simulated by one of the R-L-C circuits with its own resonance frequency. The resonance effects of all the R-L-C circuits are substituted and summed in equations (2.3.8) and (2.3.9).

The coupling coefficient $\kappa_i^2$ and the cavity $Q_{p_i}$ can be estimated from theory [25]. The values of $\kappa_i^2$ and $Q_{p_i}$ used in this simulation are the same for all modes for the sake of simplicity, even though they are actually different for the various modes in the experiment. Equations (2.3.8) and (2.3.9) are solved on a computer, and the results of the simulation for $Z_L$ are shown in Figure 2.7 for the typical density evolution and "off-resonant" tuning. The resistance and the reactance, R and X, shown in the $6^{th}$ and $7^{th}$ traces in Figure 2.7 are related to $Z_L$ by the following relations:

$$Z = R + jX$$

$$Z = Z_L - Z_{ant} = (R_L - R_{ant}) + j(X_L - X_{ant}) \qquad (2.8.1)$$

The values of the various parameters used in the computation are as follows: $Q_a = 100$, $Q_p = 400$, and $\kappa^2 = 8 \times 10^{-5}$. Note that the cavity $Q_p$ used in this calculation is the estimated unloaded cavity $Q_o$ (see Section 2.6 for the definition of loaded and unloaded cavity Q). The experimental Q which will be compared directly with this calculation is not the unloaded Q, but rather the cavity Q loaded by the generator impedance. Therefore, the estimated loaded $Q_L$ is computed for proper comparison with the experimental data. The loaded $Q_L$ can be related to the unloaded $Q_o$ by equation (2.6.11)

$$Q_L = Q_o/(1 + \kappa^2 Q_a Q_o/2)$$

The loaded cavity $Q_L$ for this calculation is 150.

To simulate the "off-resonance" tuning effect, the reactance of the matching capacitor, $X_{C_i}$ and $X_{C_2}$, are calculated for $R_{in}$ = 50 ohms

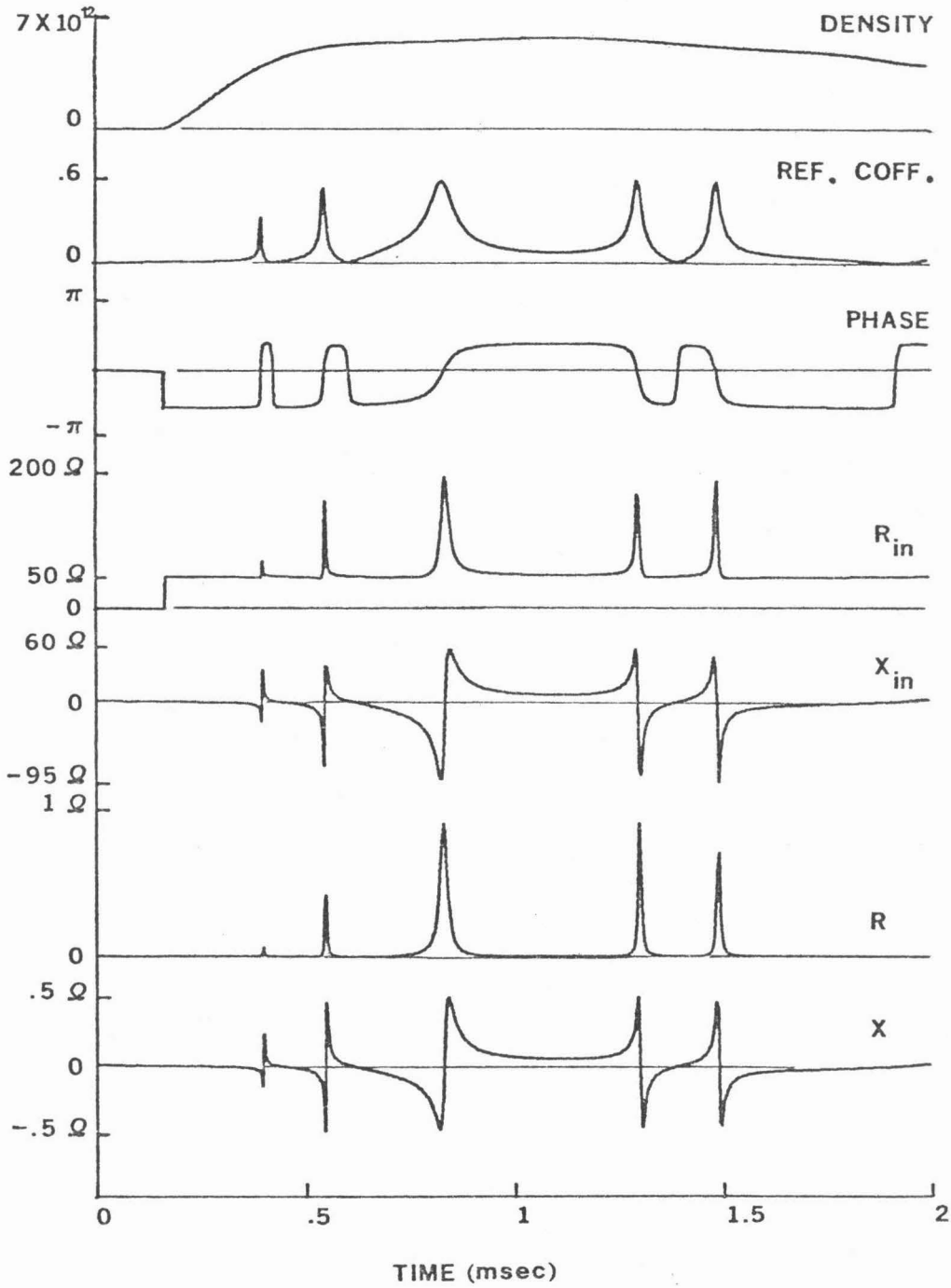


Figure 2.7

Computer simulation of various equivalent circuit parameters. In the computation, $Q_a = 100$, $Q_p = 400$, and $\kappa^2 = 8 \times 10^{-5}$.

and $X_{in} = 0$ when the cavity modes are not present, i.e., $R_L = R_{ant}$, and $X_L = X_{ant}$. The equations for the capacitive reactances are

$$X_{C_1} = R_L(1+Q_a^2)/[Q_a - \sqrt{(1+Q_a^2)R_L/R_{in} - 1}\,] \tag{2.8.1}$$

$$X_{C_2} = [\sqrt{\frac{(1+Q_a^2)}{R_{in}}}\,R_L - 1]\,R_{in} \tag{2.8.2}$$

where $R_{in} = 50$ ohms, $R_L = .3$ ohm $= R_{ant}$, and $Q_a = 100$. For this calculation $X_{C_1} = 32.5$ ohms and $X_{C_2} = 384$ ohms. By substituting the resultant values of $X_{C_1}$ and $X_{C_2}$ and the simulated values of $R_L$ and $X_L$ including the cavity resonances into the following equations, $R_{in}$ and $X_{in}$ for this model can be obtained:

$$R_{in} = R_L/[(R_L/X_{C_1})^2((X_{C_1}/R_L - Q_a)^2 + 1)] \tag{2.8.3}$$

$$X_{in} = [X_L(1 - X_L/X_{C_1}) - R_L^2/X_{C_1}]/[(R_L/X_{C_1})^2((X_{C_1}/R_L - Q_a)^2 + 1)] - X_{C_2} \tag{2.8.4}$$

By inverting the conformal transform of equation (2.6.5), the complex reflection coefficient can be calculated from $Z_{in}$ in the following manner:

$$\rho = (Z_{in} - Z_o)/(Z_{in} + Z_o)$$

where $Z_o = 50$ ohms.

The time dependence of the density evolution used in the calculations is shown in the top curve in Figure 2.7. Some of the general features of the computed solutions which will be compared with the experimental data later in Section 5.5 are noted as follows. First, for a simple pole resonance, there is a relation between the real and the imaginary parts of the impedance. Corresponding to every peak in the

real part of the impedance, the imaginary part should go through a steep change. Since the reflection coefficient is related to the impedance by a complex transform, this same behavior should also exist between the amplitude and the phase of the complex reflection coefficient. As shown in traces 2 and 3, whenever the amplitude of the reflection coefficient reaches a maximum, the slope of the phase as a function of time also is a maximum. Curves 4 and 5 show the similar behavior in the real and imaginary parts of the impedance. Second, the direction of the change of the reactance is a function of the sign of the slope of the density evolution. To clarify this point, consider curves one and five in Figure 2.7. The first curve which is the density evolution has a positive slope during the first millisecond when the density is increasing, and has a negative slope after the first millisecond when the density decays. This change in the sign of the slope is reflected in the reactance curves, traces 5 and 7. During the density buildup, the reactance goes negative first, then jumps to a positive value when a resonance is passed through. During the density decay, the reactance is positive before passing through a resonance.

## 2.9 Q Circles

Another way to see the simple pole resonance effect of a cavity mode is by plotting the input resistance of the cavity against the input reactance in the complex impedance plane. As a cavity resonance is passed through, the resultant curve is a circle, known as a Q circle [20]. Depending on how the resonance is passed through, there is a definite direction in tracing out the Q circle, i.e., whether it is clockwise or counterclockwise. The dependence of the direction of the change of the

reactance on the sign of the slope of the density evolution mentioned in Section 2.8 can be clearly demonstrated by the direction in which the Q circles are traced out. The Q circles for the resonances appearing during the density buildup are formed opposite to the direction of rotation of those occurring at the density decay. The Q circles of the experimental data are plotted in Figures 5.7 to 5.9, and this reversal of direction in which the Q circles are traced out has been observed experimentally (see Section 5.5).

# III. GENERAL EXPERIMENTAL SETUP

## 3.1 Tokamak Characteristics

A tokamak is a toroidal plasma confinement device which can be described as having the shape of a doughnut (Figure 1.1). The vacuum chamber of the Caltech tokamak is made of stainless steel with the major radius about 46 cm and the minor radius approximately 15 cm. A toroidal magnetic field is created by a current carrying coil wound on the surface of the torus. The current in the toroidal field winding is produced by a capacitor bank containing up to 50 kJ of energy.

A second winding, known as the ohmic heating winding, is wound in the toroidal direction. The windings are placed on a single surface above the toroidal field windings. The purpose of the ohmic heating coil is to produce a changing magnetic flux linking the plasma, but to have no field inside the vacuum to disturb the plasma confinement. By Faraday's induction law, the changing magnetic field linking the plasma will induce a toroidal electric field in the plasma; thus, a toroidal plasma current will be produced. This plasma current serves two purposes: First, it will provide a poloidal magnetic field which, when added to the toroidal field, will give a rotational transform to the field as illustrated in Figure 3.1. The rotational angle $\dot{\imath}(a)$ at the edge of the plasma

$$\frac{B_T}{B_p} = \frac{2\pi R}{a\dot{\imath}(a)} \tag{3.1.1}$$

so that

$$\dot{\imath}(a) = \frac{2\pi R}{a}\frac{B_p}{B_T} \tag{3.1.2}$$

where R = major radius, and a = minor radius. The safety factor $q = 2\pi/\dot{\imath}$

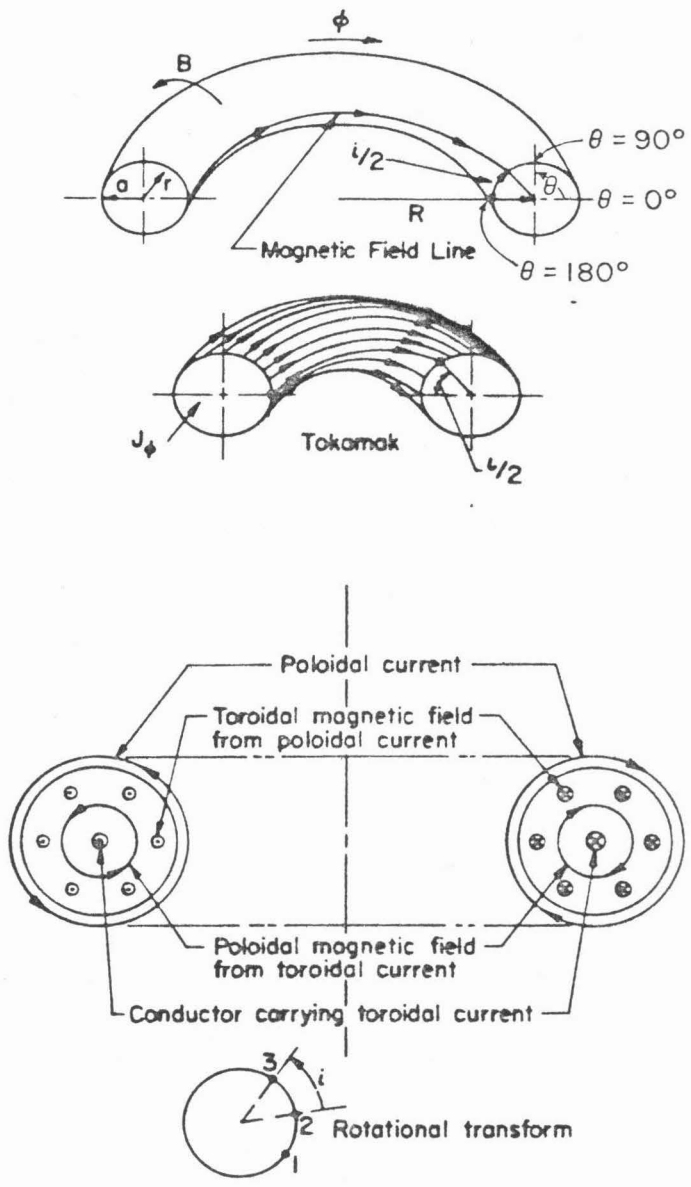


Figure 3.1
Rotation transform in a tokamak. The pitch angle $\iota = 2\pi RB_p/aB_T$. The safety factor q is $2\pi/\iota$. $\theta$ = the poloidal angle, and $\phi$ = the toroidal angle. (From Principles of Plasma Physics, by N.A. Krall and A.W. Trivelpiece)

must be greater than 2 or 3 for stable operation. For the Caltech tokamak, q is typically between 5 and 7, depending on the plasma current. Second, the current will also heat the plasma through dissipation of the plasma resistance; thus the name, ohmic heating current. The ohmic heating winding is energized by a second capacitor bank containing up to 8 kJ of energy.

Due to the toroidal geometry of the tokamak, the induced toroidal plasma current produces a poloidal field which is stronger in the "hole of the doughnut" than on the outside of the torus. This results in a magnetic pressure which pushes the plasma outward. Therefore, a third set of coils is used to produce an approximately vertical magnetic field in the plasma. This field and the plasma current produce a $\underline{J} \times \underline{B}_v$ force which compensates the outward magnetic pressure. The vertical field winding is energized by a third capacitor energy supply. The time dependence of the vertical field must be designed so as to insure equilibrium throughout the discharge period, even when the discharge parameters change. With the proper vertical field, the plasma current lasts for about 12 milliseconds.

The Caltech tokamak operates in a pulsed mode with a repetition rate of once a minute, being dictated essentially by the time to charge the capacitor banks. As mentioned previously, the energy for the different windings is stored in capacitor banks. A digital timing unit is used to control the discharge sequence of the various banks. First, the toroidal field is created. Then, a 16 kHz, one millisecond burst, called the preionization pulse, is applied to the ohmic heating winding to partially ionize the gas. This is followed by discharging the ohmic heating capacitor bank into the ohmic heating winding, producing a plasma current

up to 15 kA. Simultaneously, the vertical field is applied to provide the proper plasma equilibrium.

The vacuum chamber of the Caltech tokamak is cleaned by a process called "discharge cleaning". The method employed, first proposed by Robert Taylor of UCLA, is to bombard the vacuum chamber wall by a rapidly pulsed (2-3 times a second) low temperature hydrogen plasma [26]. The object of the process is to reduce the loosely bonded high mass impurities (carbon and oxygen) on the chamber wall so that during the actual tokamak discharge fewer impurities will be present in the plasma. Such impurities can be detrimental in a plasma confinement device because they greatly increase the radiation losses in the plasma. The rate of energy loss in the plasma due to Bremsstrahlung radiation is

$$P_b = 4.8 \times 10^{-37} Z_{eff}^2 n_e T_e^{1/2} \text{ watts/m}^3 \qquad (3.1.3)$$

where $T_e$ is the electron temperature in keV, $n_e$ is the electron density, $Z_{eff}$ is defined as

$$Z_{eff} = \sum_k Z_k^2 n_k / n_e \qquad (3.1.4)$$

$n_k$ is the density of the $k^{th}$ species ion, $Z_k$ is the degree of ionization of the $k^{th}$ species, and $n = n_e/Z_{eff}$ [27].

One can see that to minimize the Bremsstrahlung radiation power loss in a plasma, the $Z_{eff}$ must be minimized. This is the reason for using discharge cleaning. The $Z_{eff}$ of the Caltech tokamak plasma is believed to be quite low as the result of low power discharge cleaning.

A side effect of the discharge cleaning is that the plasma density drops very quickly after the initial plasma density buildup. The exact cause of this behavior in the plasma density is not completely understood

and is currently under investigation. As shown in Figure 3.2, the electron density peaks at $7 \times 10^{12}$ particles per $cm^3$ in the first .3 millisecond, then drops to $1 \times 10^{12}$ particles per $cm^3$ in the next two milliseconds. This behavior in the plasma density has important consequences in the wave excitation experiments. From the dispersion curves in Figures 2.2 and 2.3, one can see that for an input frequency between one and three times the ion cyclotron frequency, no cavity mode can propagate in the Caltech tokamak beyond the first two milliseconds in the plasma discharge when the plasma density falls below $1.5 \times 10^{12}$ particles per $cm^{-3}$. This means that all the impedance measurements of the cavity resonances must be made within the first two milliseconds in the plasma discharge.

## 3.2 Plasma Diagnostics

### a. Plasma Current and Toroidal Field Measurements

The plasma current is measured with a Rogowski coil placed on the vacuum chamber surface. The Rogowski coil is made by winding a coil on a long plastic tube, which then encircles the plasma. By Faraday's induction law, the voltage measured from the coil is

$$V = \pi\rho^2\left(\frac{N}{L}\frac{dI_p}{dt}\right) \tag{3.2.1}$$

where $\rho$ is the radius of the tube, L is the length of the tube, N is the number of turns of the wire, $I_p$ is the plasma current. To get the plasma current, the signal is electronically integrated.

The toroidal magnetic field can be accurately calculated from the toroidal winding current which is measured with a Rogowski coil. The

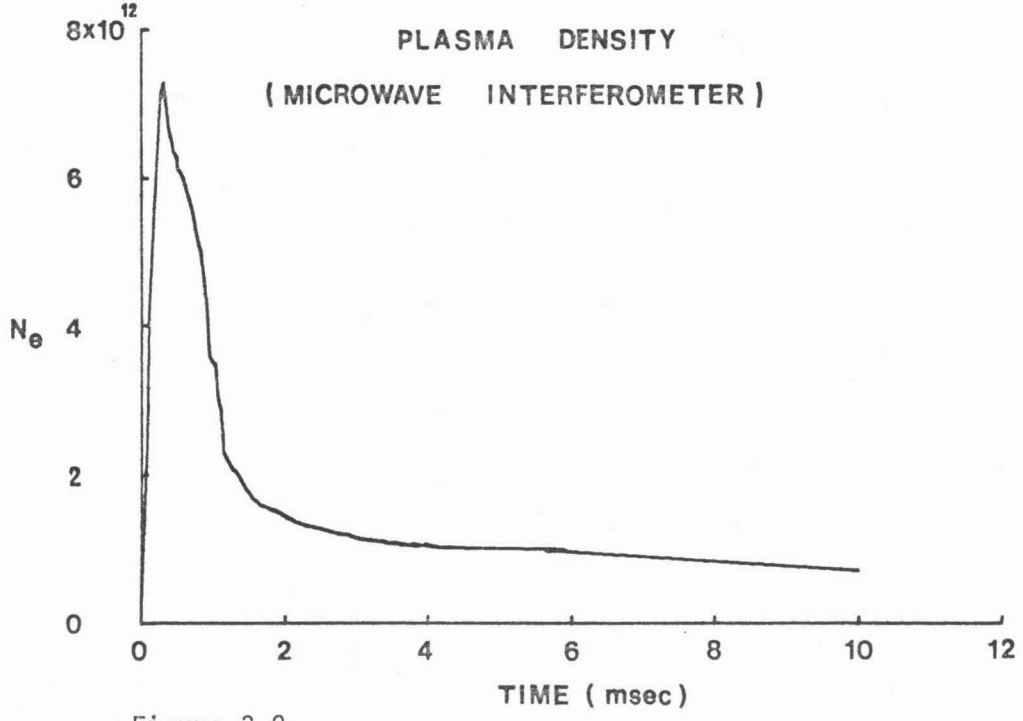


Figure 3.2
Electron density evolution as a function of time (4 mm microwave interferometer).

toroidal field variation as a function of the major radius, R, is an inverse relation, i.e., $B_T \propto 1/R$. From the dimension of the Caltech tokamak, R = 45 cm and a (the minor radius) = 15 cm, the toroidal magnetic field varies by a factor of two from the inner wall to the outer wall.

b. One-Turn Voltage

The voltage induced by the ohmic heating coil to drive the plasma current is another important quantity. To measure this voltage, a single turn wire is placed around the outside of the vacuum chamber in the direction of the plasma current. It encircles the hole in the "doughnut", thus enclosing all the flux produced by the ohmic heating air core transformer. The voltage from this one-turn loop is just the EMF produced by the changing ohmic heating flux.

One of the purposes of the so-called one-turn voltage is to infer the average electron temperature of the plasma through a measurement of the plasma resistance. The plasma temperature is related to the resistivity of the plasma as follows:

$$T_e = [1.65 \times 10^{-9}\ Z_{eff} \ln \Lambda/\eta]^{2/3} \qquad (3.2.2)$$

where $\eta$ is the resistivity of the plasma, $\Lambda$ is $\dfrac{12\pi(\varepsilon_o k_B T/e^2)^{3/2}}{n_e^{1/2}}$, and $Z_{eff}$ is the effective charge of the plasma due to high mass impurities in the plasma [28]. The $Z_{eff}$ defined in equation (3.1.4) for a hydrogen plasma is greater than one. Although we do not have a direct measurement of the $Z_{eff}$, the $Z_{eff}$ in the Caltech tokamak is believed to be quite low because of the discharge cleaning.

c. Plasma "Magnetic" Position Measurement

One would also like to know the position of the plasma column with respect to the vacuum chamber wall in order to keep the plasma well centered. This position is measured by placing two coils, the in-out coil and the up-down coil, on the torus. The in-out coil is a cosine coil, so named because it is a Rogowski coil with the number of windings per unit length following a cosine function of the poloidal angle $\theta$ (see Figure 3.1). The up-down coil is a sine coil. The cosine coil is wound on a plastic tube such that there are more turns near $\theta$ = 0 and 180°; moreover, the direction of the winding is changed at $\theta$ = 90 and 270°. Therefore, the signal from the left half of the windings is of opposite sign to the right half. If the plasma moves toward the one side of the chamber, the signal picked up by the coil on that side will increase. Thus the total output voltage is a function of position [29]

$$V = f(r,\theta) \frac{dI_p}{dt} \qquad (3.2.3)$$

By electronically integrating the signal with respect to time, the output is a position signal. The sine coil works the same way except it is rotated 90" in the poloidal direction from the cosine coil.

Because of the toroidal geometry the magnetic flux produced by the plasma current is greater at $\theta$ = 180° than $\theta$ = 0°, i.e., it is stronger on the inside of the torus than on the outside; therefore, the winding density is no longer symmetric with $\theta$ for the proper calibration of the output voltage. The cosine coil has less windings on the inside of the torus, i.e., $\theta$ = 180°, than the outside, $\theta$ = 0°.

d. Line Average Electron Density Measurement

The line average electron density in the Caltech tokamak is measured by a microwave interferometer (Figure 3.3). The phase shift between the reference signal and the signal through the plasma contains the density information. The plasma density is a function of the position, and so the average phase difference between the two legs of the interferometer is

$$\Delta\psi = Lk - \frac{\omega}{c}\int_0^L \eta_p \, dX \tag{3.3.4}$$

where L is the width of the plasma, $\eta_p$ is the index of refraction of the plasma, and k is the free space wave number. For an ordinary wave, i.e., the electric field of the wave is parallel to the d.c. magnetic field, the index of refraction can be written as follows:

$$\eta_p = 1 - \frac{\omega_p^2(x)}{\omega^2}$$

so that

$$\Delta\psi = Lk - \frac{\omega}{c}\int_0^L \sqrt{1 - \frac{\omega_p^2(x)}{\omega^2}} \, dx \tag{3.2.5}$$

Since $\omega_{pe}^2/\omega_{pi}^2 \propto m_i/m_e$, the contribution is mostly from the electrons. When the applied wave frequency is much greater than the electron plasma frequency, i.e., $\omega^2/\omega_{pe}^2(x) >> 1$, the above equation can be approximated by the following:

$$\Delta\psi \simeq \frac{\omega}{2c}\int_0^L \frac{\omega_{pe}^2(x)}{\omega^2} \, dx = \frac{\omega}{2c}\frac{\overline{\omega_{pe}^2}}{\omega^2} \tag{3.2.6}$$

where $\overline{\omega_{pe}^2} = \int_0^L \omega_{pe}^2(x) \, dx$ is the average electron plasma frequency. This phase shift can be seen as a series of interference fringes at the

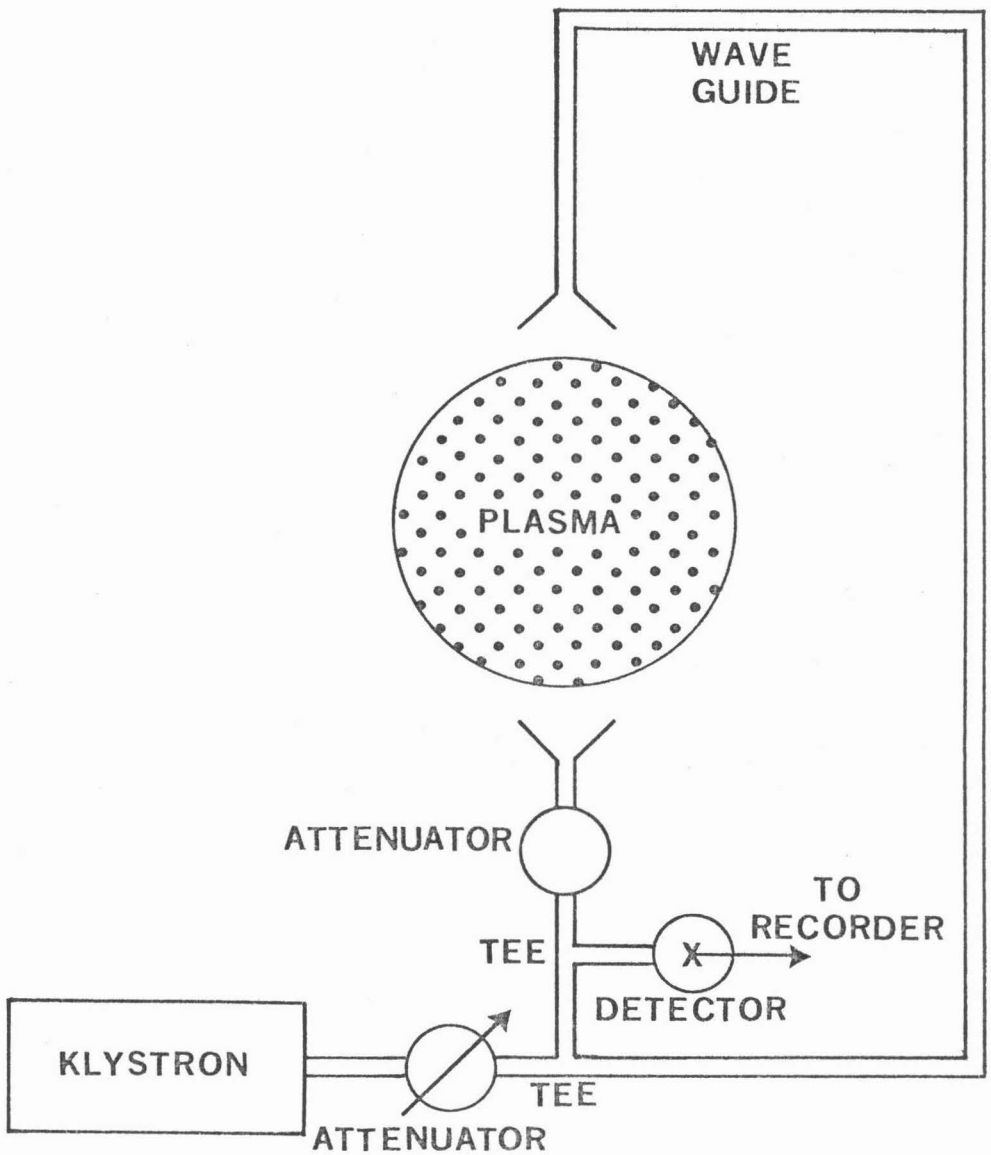


Figure 3.3
Interferometry arrangement for microwave measurement of the plasma density. (4 mm microwave interferometer)

detector output. One fringe corresponds to a phase shift of $\Delta\psi = 2\pi$. The corresponding average electron density $\bar{n}_e = \frac{1}{L}\int_0^L n_e(x)\,dx$, is

$$\bar{n}_e = \left(\frac{m_e \varepsilon_o \omega}{e^2}\right) \frac{2c}{L} \Delta\psi \qquad (3.2.7)$$

when $\omega^2/\omega_{pe}^2(x) >> 1$ is imposed. Thus the electron density is a linear function of the phase shift or the number of output fringes when the microwave frequency satisfies the above condition, $(\omega^2/\omega_{pe}^2(x)) >> 1$. The frequency of the microwave interferometer used on the Caltech tokamak is 60 GHz. and the maximum average electron density is about $7 \times 10^{12}$ particles per $cm^3$, which corresponds to an electron plasma frequency of 24 GHz. If it is assumed that the density profile is a parabolic function of distance, the relation between the peak density and the average density is $n_{peak} = (3/2)n_{avg}$. So the peak density corresponding to our case is approximately $1 \times 10^{13}$ particles/$cm^3$, which gives an approximate electron plasma frequency of 36 GHz. Therefore, the assumption of $(\omega^2/\omega_{pe}^2(x)) >> 1$ is a good one even for the peak density.

The fringe counting for the microwave system on the Caltech tokamak has an uncertainty factor of ±1/4 fringe. The source of the uncertainty comes from the noise superimposed on the interference signal from the detector. The origin of the noise is not completely understood. Some of it may be due to actual fluctuation in the plasma density. By carefully matching the fringes for the initial density buildup with the decay fringes, the time dependence of the plasma density can be determined fairly well.

e. Langmuir Probe Measurement

The conditions at the edge of the plasma are mild enough that Langmuir probes can be used to measure the local electron density and

temperature. Data have been taken for the first 5 cm into the plasma by R. Kubena [30] without any major probe damage. The results when extrapolated agree fairly well with the density measurements from the microwave interferometer mentioned in Section 3.2c, and the electron temperature data from the plasma resistance measurement depicted in Section 3.2b.

## 3.3 Summary of Plasma Parameters

From the diagnostics just described, the Caltech tokamak plasma has the following characteristics:

| | |
|---|---|
| Toroidal field: | 3 to 6 kG (4 kG on center) at R = 30 cm and R = 60 cm, respectively |
| Plasma current: | 15 kA (peak)<br>12 msec (duration) |
| Line average electron density: | $7 \times 10^{12}$ to $1.5 \times 10^{12}$ $cm^{-3}$ (decays during the first two msec) |
| Average electron temperature: | 50 to 100 eV (assuming $Z_{eff} = 1.5$) |

where R is the major radius of the torus.

## 3.4 Digital Data Acquisition System

All experimental data from the Caltech tokamak experiments, such as the signals from various diagnostics, the crystal detected r.f. signals, etc., are recorded on a multichannel digital transient recorder which converts the various analog signals into digital data that are stored in its semiconductor memories. Each of the 16 channels of the

transient recorder has a 1024 word memory with 8 bits amplitude resolution per word. Four of the channels have a one-microsecond per word clock rate, so the maximum frequency response with four-word resolution is about 200 kHz. The rest of the channels have a clock rate of 5 microseconds per word, so the frequency response with four-word resolution is about 40 kHz.

The digital output signals from the transient recorder memories can then be used in several ways. Analog signals can be reconstructed with D-A converters for continuous display on scope monitors after each plasma shot. The transient recorder can also drive an analog pen plotter, so that hard copies of the signal can be produced. If calculations need to be done with the data, the digital data can be written on magnetic tape for later processing at the Caltech central computer facility (IBM 370, model 158).

# IV. EXPERIMENTAL SETUP FOR THE R.F. MEASUREMENTS

## 4.1 Experimental Arrangement for Transmission Measurement

The first step in the study of the magnetosonic cavity modes was to observe them with a receiving probe located 180° toroidally from a transmitting antenna (Figure 4.1).

A simple single-turn transmitting loop antenna made of tungsten was first used (Figure 4.2). The race track shape antenna had the dimension of 3.75" x 1". The design of the antenna was governed by three factors. First, it must fit into a 4"x 1"x 6" port. Second, to get good coupling with the plasma, the loop area should be maximized. Finally, the antenna should be kept away from the center region of the plasma where most of the damage to the antenna will occur. This made the shape long and narrow. R.F. signals are carried to the tungsten antenna by parallel copper wires enclosed in a glass-to-stainless steel transition tube. The stainless steel tube provides the mechanical feed-through from the outside into the vacuum chamber. The glass is to give electrical insulation for the antenna from the tokamak. The measured resistance of the entire antenna structure is about 2 ohms at 10 MHz.

The antenna can be moved radially in and out of the plasma through a vacuum O-ring seal. All transmission measurements are done with the antenna located no more than 1.25 inches into the vacuum chamber in order to prevent any plasma damage to the antenna. This is the low density region in the tokamak, according to Langmuir probe data, ($n_e < 5 \times 10^{11}$ particles/cm$^2$).

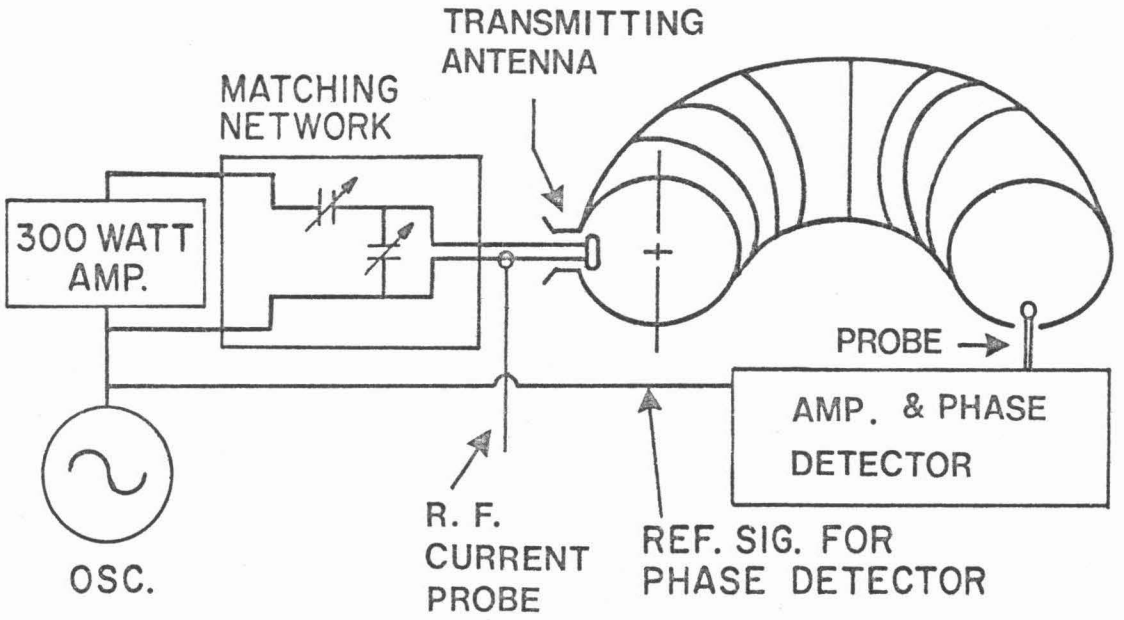


Figure 4.1

Experimental arrangement of the transmission measurement.

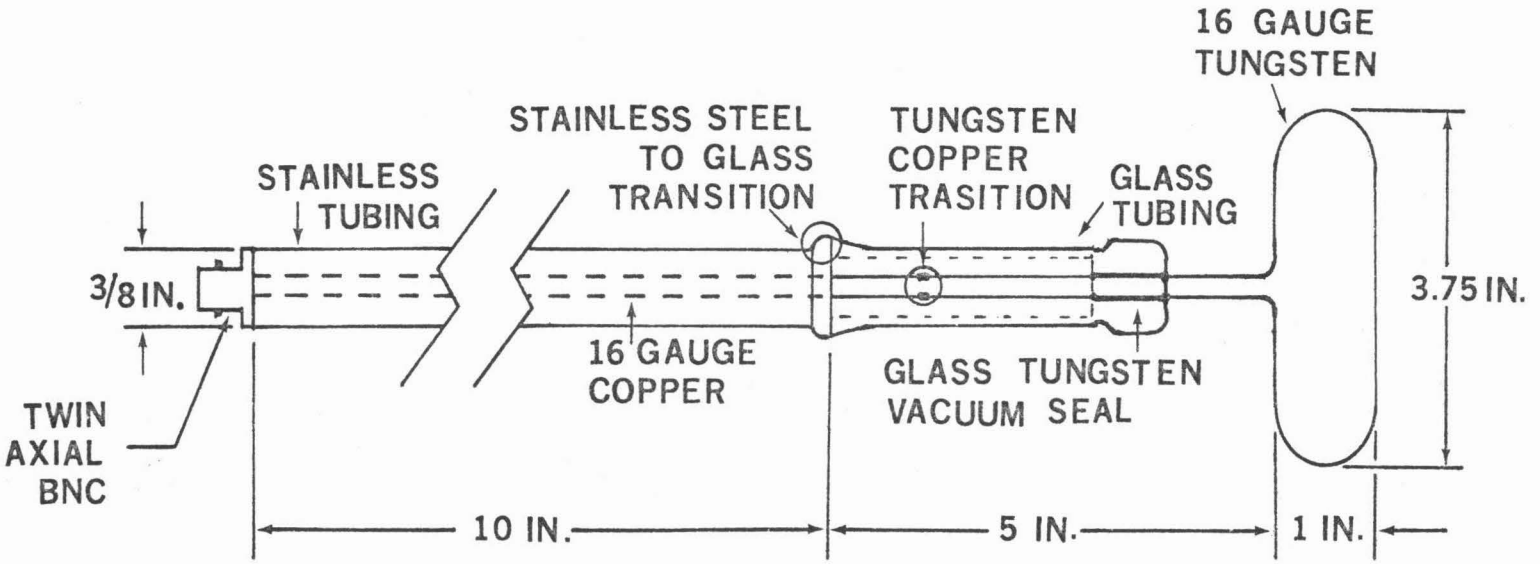


Figure 4.2

Single- turn tungsten antenna used initially as the transmitting antenna in the transmission measurement.

A matching network consists of a variable series capacitor used to tune out the antenna inductance, and a R.F. transformer to match the antenna impedance to 50 ohms. An ENI 300-watt wide-band amplifier driven by a Hewlett-Packard 8601A sweeper oscillator is used to excite the wave. The input r.f. frequency to the transmitting antenna is fixed for each plasma discharge. This way only one variable, the plasma density, is changing during the experiment. To study the frequency dependence of the cavity modes, the input frequency is changed between plasma shots.

To detect the cavity resonances, a small six-turn loop probe is placed in the tokamak. The receiving probe is kept small so that it couples weakly to the cavity. This way the probe does not influence the cavity while it is measuring the r.f. signal. As shown in Figure 4.1, the receiving probe is located 180° toroidally from the transmitting antenna. The output of the probe is passed through a tunable bandpass filter, with a bandwidth of 300 kHz; thus any broadband noise from the plasma can be reduced. The r.f. signal is then split into two branches. One branch goes into a square law crystal detector which has an output operational amplifier with a slew rate of 4V in 2 μsec, for amplitude detection. The other line is fed into a phase detector which can respond to a $2\pi$ phase shift in 4 μsec so the phase between the transmitted and the received signals can be examined. As mentioned in Section 3.4, the output of the phase and amplitude detectors is digitized and recorded in the multichannel transient recorder. The experimental data of the transmission measurements are presented in Section 5.1.

## 4.2 Antenna and Matching Network Design

The initial measurement of the plasma loading resistance was made with the single-turn tungsten antenna, which has a resistance of 2 ohms at 10 MHz. The impedance matching circuit consists of a series of air variable capacitors used to tune out the antenna inductance, and a broad-band ferrite core r.f. transformer made to match the antenna resistance to the amplifier impedance. With this setup, only a minute amount of plasma loading at the cavity resonances was detected. However, the large increase in the transmitted signal measured by the six-turn probe at the cavity resonances led us to think that there must be better power coupling between the antenna and the tokamak at the cavity resonances than when there were no cavity modes. This effect should show up as antenna loading by the plasma at the cavity resonances. It was believed that the sum of the resistance from the antenna, the matching network, and the r.f. transformer was so high that the plasma loading was overshadowed.

To understand the effect of the antenna resistance on the plasma loading resistance measurement, consider equation (2.3.8a) at one of the cavity mode frequencies:

$$R_L = R_{ant}[1 + Q_a \kappa_i^2 Q_{p_i}]$$

where it is assumed that the various cavity modes are separated far enough in their eigenfrequencies that only one mode dominates in the resistivity loading. From this expression, one can see that in order to measure the plasma loading effect, $Q_a \kappa_i^2 Q_{p_i} > 1$. Let us estimate the magnitude of this factor for the tungsten antenna. For the

tungsten antenna, $Q_a$ is around 10, $\kappa^2$ is estimated to be $5 \times 10^{-6}$, and $Q_p$ is assumed to be 500, so their product is $2.5 \times 10^{-2}$, which is much smaller than one. Furthermore, consider the efficiency of the antenna $\eta$ in equation (2.7.2)

$$\eta = \kappa^2 Q_a Q_p / [1 + \kappa^2 Q_a Q_p]$$

for one of the modes. In order to have efficient wave generation in the tokamak, the same inequality, i.e., $\kappa^2 Q_a Q_p > 1$, must be satisfied in order to generate more energy in the tokamak than is dissipated by the antenna. Therefore, the antenna and the matching network was redesigned to improve the factor $\kappa^2 Q_a$.

The coupling coefficient $\kappa^2$ can be increased by increasing the antenna size. However, as mentioned in Section 4.1, the loop area of the antenna is determined by the port size on the tokamak, and the maximum distance the antenna can protrude into the plasma without suffering damage to the antenna. Therefore, the coupling coefficient of the antenna cannot be increased very much. There are two ways to increase the antenna Q, $Q_a$: either increase the inductance or decrease the resistance. The antenna inductance is increased by going from a single-turn loop to a two-turn loop. The maximum number of turns on the loop antenna is determined by the size of the conductor used and the width of the port, which is one inch on the tokamak. The antenna resistance is decreased by using material with better conductivity, and by increasing the size of the conductor. The conductor used in the antenna is changed from 16 gauge tungsten wire to 1/8-inch diameter copper tubing. To prevent plasma

damage to the copper antenna and to insulate the antenna electrically from the plasma, the copper antenna is enclosed in pyrex glass. The measured Q of the bare copper antenna is about 130 at 10 MHz, and the inductance of the antenna is about .46 microhenry.

However, once the copper antenna is placed in a glass-to-stainless steel transition tube which provides the mechanical feedthrough from the outside to the vacuum chamber, the antenna Q drops by a factor of two. The additional losses come from the eddy current losses in the stainless steel tube which has a 50 times higher resistivity than copper. To reduce the eddy current losses, a copper lining of .025 inch thick is placed on the inner wall of the stainless steel tube, thus reducing the eddy current losses. With the copper lining, the Q of the antenna is about 100 at 10 MHz, and the inductance of the antenna is .46 microhenry.

It is just as important to reduce the losses in the impedance matching network. There were two problems with the original matching network. First, the equivalent series resistance of the air variable capacitor and the added resistance from the transformer are quite high. Second, the winding ratio on the transformer is fixed, thus the impedance of the generator can be matched only at one frequency, since the antenna resistance is a function of frequency. Therefore, the improved matching network must have two essential features. It must have low resistance and it must be able to match the antenna and the generator for the entire range of frequencies of interest. It was finally decided to use vacuum variable capacitors which have low series resistance and multiturn

adjustment capability that assures precise tuning. The new matching network is shown in Figure 4.3. This particular circuit was chosen because of its simplicity and the minimum number of circuit elements needed. Details on the dimensions of the antenna and the values of the capacitors in the matching network are covered in Appendix a.

## 4.3 Plasma Loading Resistance Measurements

As shown in Section 2.7, the plasma loading resistance at one of the cavity resistances, $R_L = M^2\omega^2/R_p$, is a crucial quantity in determining the efficiency of the antenna in delivering the r.f. power into the tokamak. The efficiency, $\eta$, depends on the plasma loading resistance and the antenna resistance, $R_{ant}$, in the following way [equation (2.7.1)]

$$\eta = M^2\omega^2/R_p \; [R_{ant} + M^2\omega^2/R_p]$$

Therefore, in order to have good efficiency in wave generation in the tokamak, it is essential for the resonance plasma loading resistance to be greater than the antenna resistance $M^2\omega^2/R_p > R_{ant}$. And so the plasma loading resistance must be measured in the experiment and compared with the antenna resistance.

One way to obtain the plasma loading resistance is to measure the incident power, the reflected power into the antenna, and the antenna current. As indicated in equations (2.6.1) and (2.6.2), the incident and reflected power into the antenna can be derived from the incident and reflected voltages measured with a VHF directional coupler placed between the generator and the antenna matching network.

$$P_{inc} = V_{inc}^2/50 \qquad P_{ref} = V_{ref}^2/50$$

The antenna current is measured with a high frequency Tektronix current probe. Once the antenna current is known, the plasma loading resistance can be calculated as follows:

$$R = (P_{inc} - P_{ref}) / I^2 - R_{ant} \qquad (4.3.1)$$

where I is the antenna current, and $R_{ant}$ is the antenna resistance.

The experimental setup for the plasma loading resistance measurements is shown in Figure 4.3. As mentioned previously, the incident and reflected voltages are measured by a VHF directional coupler with a characteristic impedance of 50 ohms. The directional coupler is placed between the r.f. amplifier and the antenna impedance matching network, and so any change in the antenna resistance due to the plasma would show up as a change in the reflected voltage. The output of the directional coupler is fed into a r.f. crystal detector and a phase detector. The crystal detector measures the amplitude modulation on the r.f. signal coming from the directional coupler. The output of the crystal detector is fed into the multichannel transient recorder to be digitized and recorded. The phase measurement of the incident and reflected voltages is for obtaining the complex plasma loading impedance, and the details of this measurement are covered in the next section (Section 4.4).

When the low resistance copper antenna is used, the r.f. current in the antenna can get as high as 30 amperes. The r.f. current probe used is only linear up to 2 amperes, so a 15 to 1 current divider is placed in parallel with the antenna. The current divider is simply a piece of small diameter wire with resistivity 15 times higher than the 1/8 inch copper used in the antenna. Since the current probe is mounted on the divider,

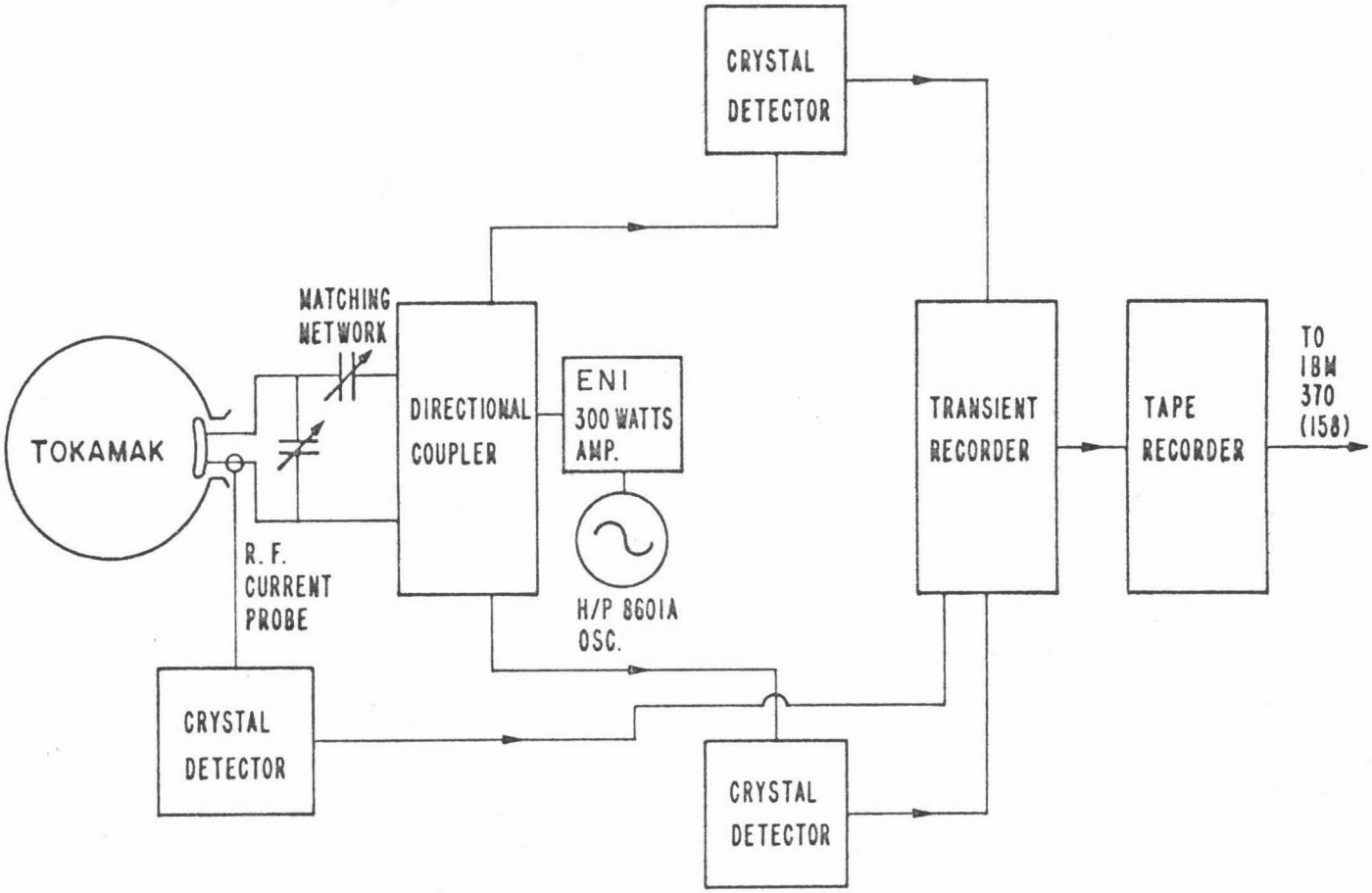


Figure 4.3

Experimental arrangement for plasma loading resistance measurement. The input r.f. power into the antenna is measured by the VHF directional coupler. The antenna current is measured by a high frequency current probe.

which is in parallel with the antenna, any added resistive losses due to the current probe has little effect on the antenna resistance. The results of the plasma loading resistance measurements are presented in Section 5.3.

## 4.4 Phase Measurement

To obtain the complex loading impedance of the plasma at a cavity resonance, the phase difference between the incident and the reflected voltage into the antenna must be measured. As shown in Section 2.6, the ratio of the amplitudes of the incident and reflected voltages into the antenna gives the magnitude of the reflection coefficient, and the phase difference between the incident and the reflected voltage into the antenna gives the phase of the reflection coefficient.

$$\rho = (V_{ref}/V_{inc})\, e^{j\phi} = |\rho|\, e^{j\phi} \qquad (4.4.1)$$

where $\phi = \phi_{ref} - \phi_{inc}$. The complex input impedance can be obtained from the complex reflection coefficient by a complex transform. The resistance, $R_{in}$, and the reactance, $X_{in}$, measured at the antenna matching network (see Figure 2.4) are related to the complex reflection coefficient by equations (2.6.6) and (2.6.7).

As shown in Figure 4.4, the signals from the directional coupler which measures $V_{ref}$ and $V_{inc}$ are split with one branch going to the crystal detectors, and the other going to a phase detector. The phase detector is built to measure phase in a pulsed system. The phase detector is capable of following a $2\pi$ phase shift in 4 microseconds. As shown in the block diagram of the detector (Figure 4.5), the input r.f. signals

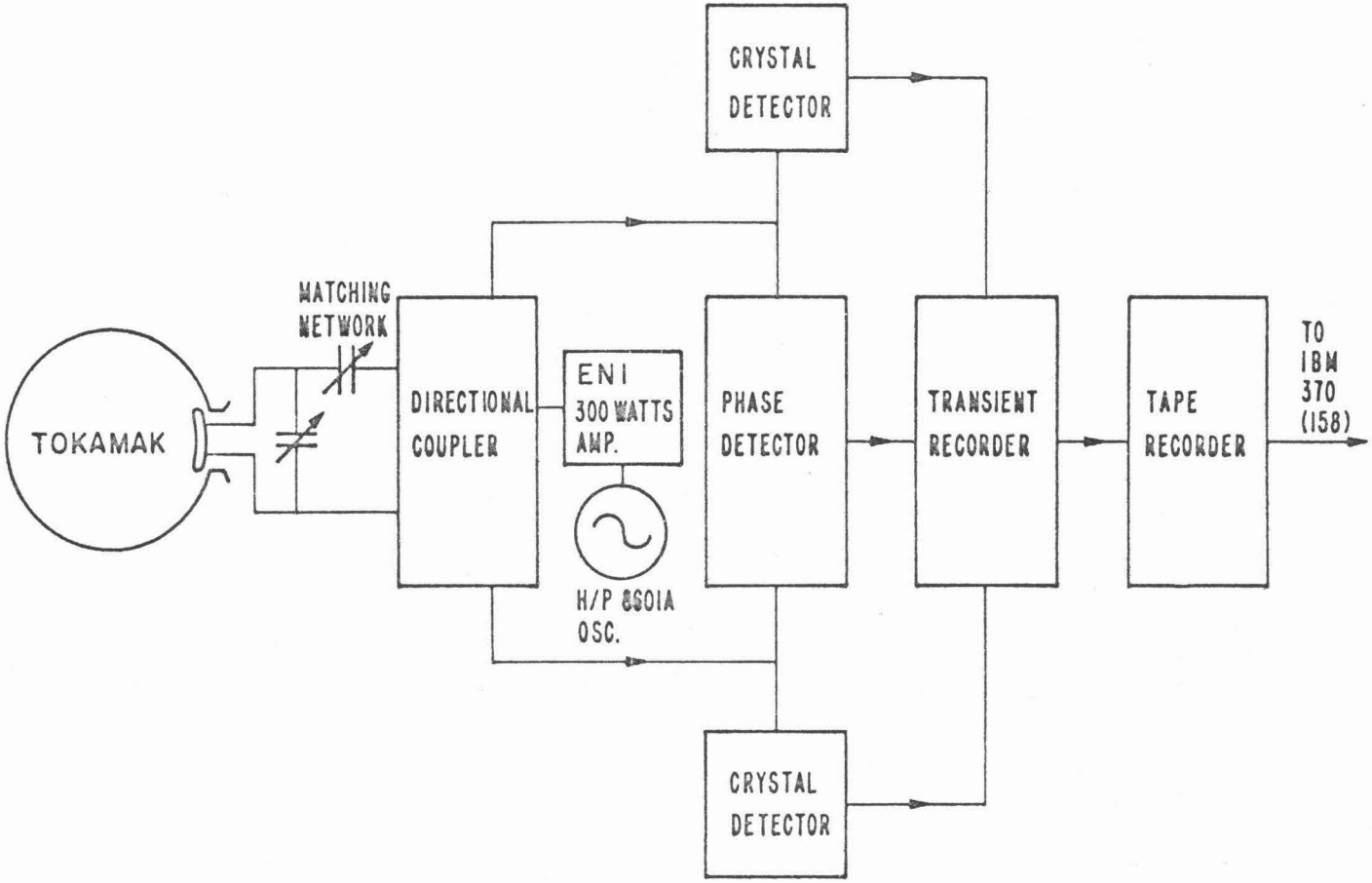


Figure 4.4

Experimental arrangement for complex plasma loading impedance. The phase between the incident and reflected waves is measured by a r.f. phase detector (see Figure 4.5). The amplitudes of the incident and reflected voltages are measured by crystal detectors.

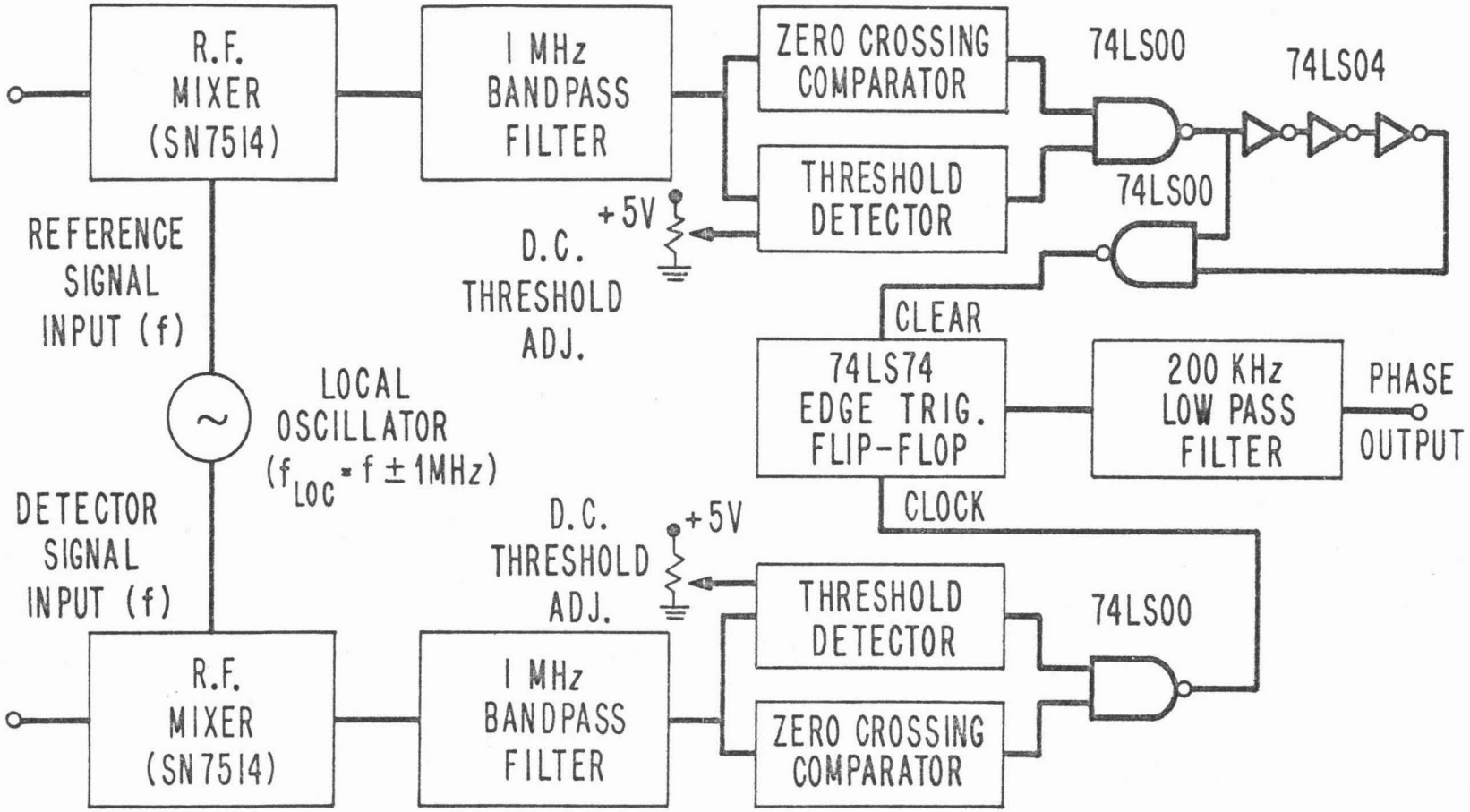


Figure 4.5

R.F. phase detector (5 - 50 MHz). Zero crossing comparators are used to shape the 1 MHz sinusoidal signal into a square wave. The threshold detector has no output if the input 1 MHz signal is below the voltage set by the threshold adjustment, thus disabling the phase detector. 200 KHz low pass filter is a 5-pole Butterworth filter with 10-90 % risetime in 4 μsec.

are mixed down to 1 MHz with a local oscillator, so that the output voltage of the detector is not frequency dependent. A sensitive zero crossing comparator is used to ensure that the phase output is not amplitude dependent. The input frequency range of the detector is between 5 and 50 MHz, which covers the frequency range of interest, 7 to 20 MHz. The output voltage of the detector is a linear function of the phase, and the detector is capable of measuring phase shifts up to $2\pi$. When the complex reflection coefficient is calculated from the measured amplitude and phase of the incident and reflected voltages, the complex plasma loading impedance can be obtained from the conformal transforms in equations (2.6.6) and (2.6.7).

The quantity of interest in the experiment, as indicated in Section 2.6, is the plasma loading impedance, $Z_L$ (see Figure 2.4). $Z_L$ can be obtained from $Z_{in}$ by substituting the measured values of $C_1$ and $C_2$ of the impedance matching network into equations (2.5.1) and (2.5.2). The plasma loading impedance, Z, can be derived from $Z_L$ by subtracting out the antenna impedance, $Z_{ant}$:

$$Z = Z_L - Z_{ant} \tag{4.4.2}$$

The experimental results of these measurements are presented in Section 5.5.

# V. EXPERIMENTAL RESULTS

## 5.1 Transmission Measurements

The toroidal eigenmodes were first observed in transmission. As described in Section 4.1, the transmitted signals were detected by a six-turn loop probe located 180° around the toroidal axis from the transmitter (Figure 4.1). The input frequency into the transmitting antenna was held constant. The cavity modes were swept through by the change in density as a function of time. The modes appear as a series of peaks on the r.f. output of the receiving probe. The received r.f. signals were passed through band-pass filter with 300 kHz bandwidth and then fed into a crystal detector for amplitude detection. The output of the crystal detector is just the amplitude modulation on the r.f. signal, i.e. a series of peaks.

A few of the typical transmission measurements for various input frequencies are shown in Figure 5.1. The top curve in Figure 5.1 is a trace of the electron density evolution as a function of time for a typical plasma discharge. The density evolution for different plasma shots is not completely reproducible, so the purpose of this trace is only to give the general features of a plasma discharge.

The density values at which the cavity resonances are swept through are found to be a function of the applied frequency. At the lower applied frequencies, the transmission peaks cluster near the high density region, whereas they become more spread out and appear in the low density region at the higher applied frequencies. The reason for this behavior can be understood by studying the dispersion relations of the magnetosonic wave. From the dispersion curves in Figure 2.2, one can see that in

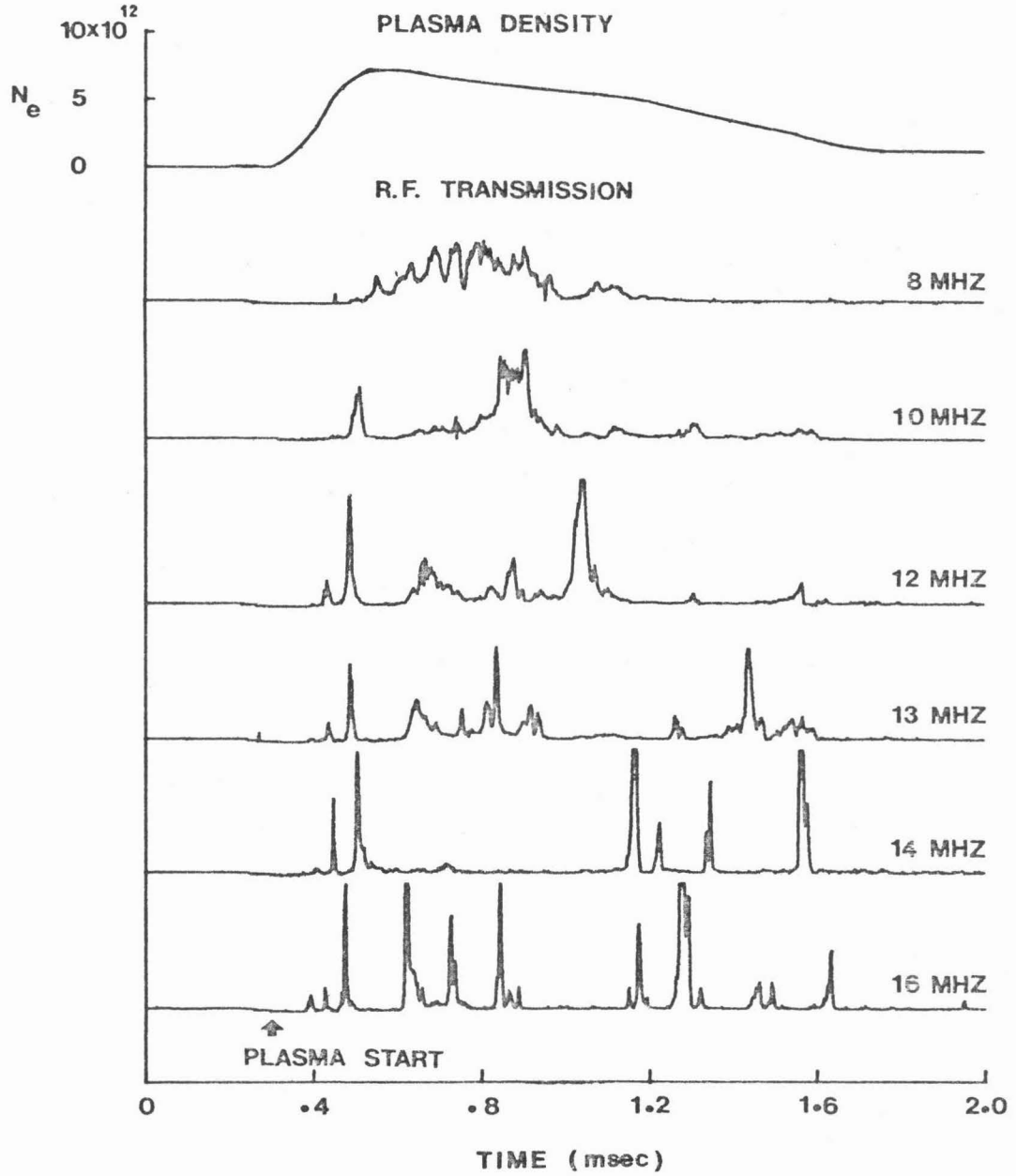


Figure 5.1
Transmission measurements versus a typical density evolution as a function of time.

order to excite a particular mode at a given frequency, a certain plasma density is required. To excite the same mode at a lower frequency means the plasma density must be higher. This is just the observed experimental result. When the input frequency is low, the resonance peaks gather around the high density region, and as the input frequency increases, the peaks move into the low density region.

This inverse relation between frequency and plasma density can be simply summarized by the cut-off relation of the modes, i.e., k = 0. The approximate cut-off relation is expressed in equation (2.1.5),

$$f_{\ell m0} \simeq A_{\ell m0}/\sqrt{n_e}$$

where $\ell$ is the radial mode number, m is the poloidal mode number, N = 0 is the axial mode number, and $n_e$ is the electron density. The equation shows that for higher density, the cut-off frequency is lower; by the same token, the low frequency modes propagate only near the density maximum. One of the observations in the experiment is that no cavity mode was observed at frequencies below 7 MHz.

To compare with the theory for a cold uniform cylindrical plasma-filled cavity model, the cut-off curves for various poloidal modes are superimposed on the experimental data in a density versus frequency plot (Figure 5.2). The data points in the figure are obtained by the following procedure. The transmission peaks and the plasma density are recorded as in Figure 5.1 for a series of plasma discharges, typically between 4 and 6 shots, with the same input r.f. frequency. The time at which a cavity resonance appears during the discharge is recorded. The

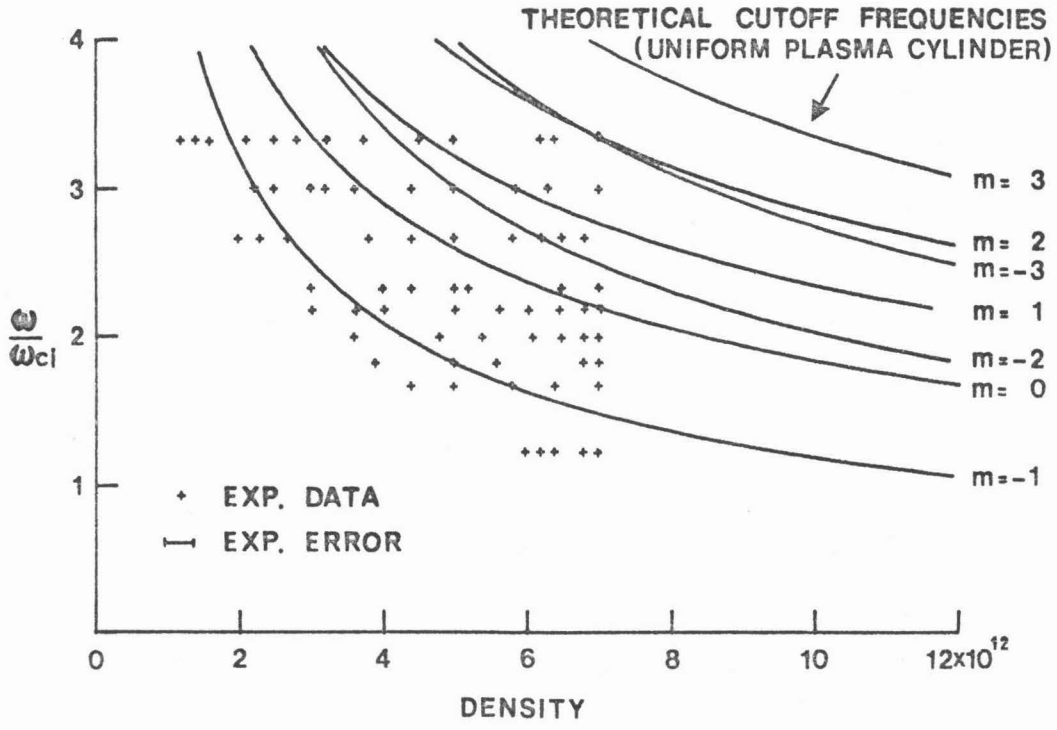


Figure 5.2

Theoretical magnetosonic cavity mode cutoffs (i.e. toroidal mode number N=0) in a cold plasma versus experimental data. These curves are for the lowest radial mode ($\ell$=1).

values of the density at which the cavity resonances appear can be obtained from the measured line average density values at these recorded moments in time. Once both the frequency and the density for the modes are known, a point can be plotted on the density-frequency graph (Figure 5.2). The input frequency has been normalized to the ion cyclotron at the center of the tokamak, i.e., 6 MHz. Only the consistent peaks--that is, peaks that appear in the same general density region for all the shots, are used. To get the frequency dependence of the modes, the input frequency is changed between series of fixed frequency shots.

The agreement between the experimental data and the theory as shown in Figure 5.2 is fairly good, though not perfect. There are data points below the general region of the cut-off curves. The reason for the small number of discrepancies between theory and experiment is the simplicity of the theory used. The toroidal effects, radial density profile, poloidal magnetic field effects, and many others have not been properly accounted for in the theory. There is also a small amount of uncertainty in the experimental data as indicated in Figure 5.2. This comes from the experimental errors in the electron density measurement where the density uncertainty is about $\pm\frac{1}{4}$ fringe at the output of the microwave interferometer (see Section 3.2d).

Since the plasma-filled cavity can be modeled by the equivalent R-L-C circuit which has a simple pole at resonance, there must be some relation between the amplitude and phase of the transmitted signal at the cavity resonances. Passing through a resonance, the phase should undergo rapid change whenever the amplitude shows a peak. This effect

can be detected by measuring the phase difference between the received wave and the input oscillator signal at the transmitter (see Figure 4.1). The result of a typical phase measurement and amplitude signal versus time is shown in Figure 5.3.

Several properties of the amplitude and phase detectors, and the experimental conditions can aid in the understanding of some of the features of the data shown in Figure 5.3. The amplitude signal is inverted because the crystal detector used in the experiment is inverting. As shown in Figure 4.5, the phase detector has a threshold detector where if the input signal is below a preset d.c. value, the output of the phase detector sits at the highest output level (corresponding to the zero value shown in Figure 5.3). This is the reason that the phase signal always returns to zero when the amplitude drops below a certain level. The phase measurements were done with approximately 20 watts r.f. power into the transmitting antenna, so the received amplitude signals were rather low. As the signal level approaches the d.c. threshold level of the phase detector, there is a transition region of 10 mV around the threshold voltage where the phase detector output is an oscillating signal. This is the result of the TTL transition region for the nand gate (74LS00) when it switches between zero and one states. This can explain some of the noise-like oscillation when the phase detector is turning on and off. Furthermore, the phase detector has a "dead" region

of 20 degrees when the phase goes beyond 360 degrees and returns at zero degree. Finally, there were cases of the data where the peaks in the amplitude do not occur exactly at the same time as the steepest rate of change of phase. There is no good explanation for such cases.

One proposed way to identify the various poloidal modes, which are separated fairly far from each other, is to reduce the step size of the change in input frequency between shots. This way a resonance peak seen at a particular density for a given input frequency can be identified with a peak at a slightly different density, when the input frequency is changed by a small amount. In other words, to decrease the size of the frequency step taken between plasma shots so that the data points in Figure 5.2 would be more closely spaced along the frequency axis. In priciple, as the frequency steps are reduced to small values, the peaks that belong to the same mode can be picked out. (In our experiment some correlations between peaks can be made). By overlaying the theoretical dispersion curves on the data one can guess that a particular set of data corresponds to a certain mode. However, this method is not used here because the various theories are not adequate for such a detailed comparison. For example, the dispersion curves depend on the assumed radial density profile used in the theory.

The theory used in this thesis is for a uniform plasma density. However, if a vacuum region is introduced between the plasma and the cavity wall, the locations of the dispersion curves would shift. If the

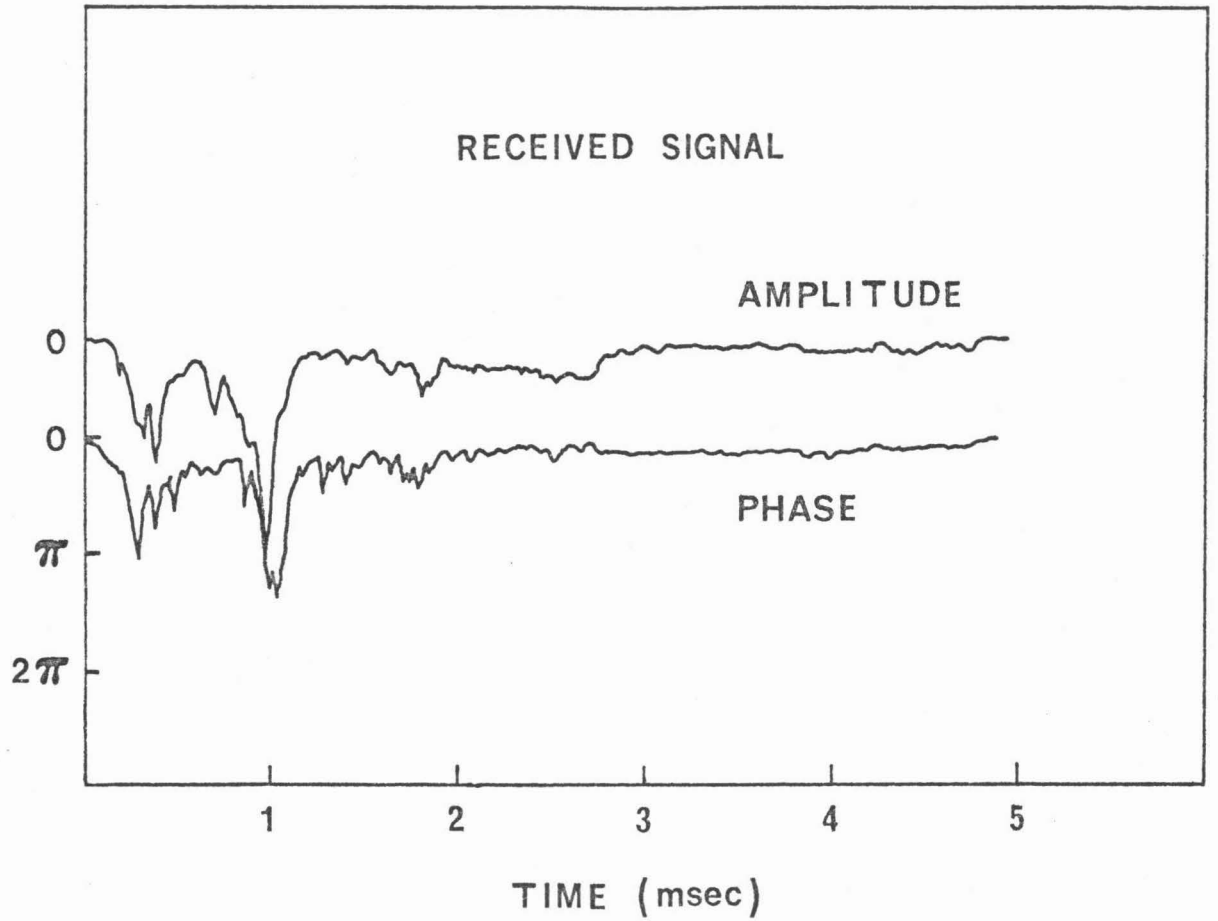


Figure 5.3

Amplitude and the phase of the received signal in the transmission measurement.

vacuum is large enough, as was shown by Paoloni [18], the m = 1 mode has no low frequency cut-off (see Section 2.2).

The unambiguous method for mode identification is to use probes to measure the spatial dependence of the fields in the tokamak. This measurement was not made in our experiment because of lack of time, so there is no definite mode identification.

## 5.2 Plasma Loading Impedance in the Absence of the Cavity Modes

In this section the experimental results of the "off resonance" antenna impedance for different input frequencies are presented. The "off resonance" antenna impedance, $Z_{off} = R_{off} + jX_{off}$, is defined in Section 2.5 as the sum of the antenna impedance and the plasma loading impedance during the absence of any cavity resonances. $R_{off}$ and $X_{off}$ are determined by substituting the capacitance values, $C_1$ and $C_2$, of the impedance matching circuit used to match the generator impedance "off resonantly" into equations (2.5.1) and (2.5.2). (The condition for impedance matching in these equations is when $R_{in}$ = generator impedance = 50Ω.) To obtain the "off resonance" loading impedance due to the plasma alone, $\Delta Z = \Delta R + j\Delta X$, the antenna impedance must be subtracted from $Z_{off}$,

$$\Delta R = R_{off} - R_{ant} \tag{5.2.1}$$

$$\Delta X = X_{off} - X_{ant} \tag{5.2.2}$$

An interesting experimental finding is that the "off resonance" plasma loading reactance, $\Delta X$, is greater than zero, i.e. the antenna inductance is <u>increased</u> by the plasma effect. A possible explanation for the

increase in the antenna input inductance with the onset of the plasma is given in Section 2.3. As indicated in equation (2.3.9a), if the reactance contribution from the cavity modes with resonant frequencies higher than the applied frequency is greater than the contribution for the other modes, the basic antenna inductive reactance will show an increase from the effects of the cavity modes. The values of $\Delta R$ and $\Delta X$ for different input frequencies are given in Tables 5.1 and 5.2.

The experimental procedure for measuring the "off resonance" impedance, $Z_{off}$, was as follows. First the antenna was matched to the generator impedance in the absence of the plasma. The matching process was to adjust the capacitors $C_1$ and $C_2$ so that a minimum in the reflected voltage from directional coupler was observed (see Figure 4.3). Once the plasma was formed around the antenna, the generator impedance was no longer matched, and the reflected voltage from the directional coupler increased. At this point $C_1$ and $C_2$ were readjusted to minimize the reflected voltage in the presence of the plasma. The values of $C_1$ and $C_2$ were recorded and then substituted into equations (2.5.1) and (2.5.2) so that the "off resonance" impedance could be obtained.

The effects of "off resonance" plasma loading impedance for various input frequencies are summarized in the 7th and 8th columns of Tables 5.1 and 5.2. The data in these tables were taken under similar conditions but on different days, and so they serve as a comparison for each other. The first column indicates the input frequencies. Corresponding to each frequency, the input impedance of the antenna was measured with and without a plasma, as indicated in column 2. First the antenna impedance was obtained in the vacuum chamber by measuring the values of the tuning capacitors $C_1$ and $C_2$ (see columns 3 and 4). The

antenna resistance, $R_{ant}$, and inductance, $L_{ant}$, can be derived by substituting $C_1$ and $C_2$ into equations (2.5.1) and (2.5.2). As shown in the tables, when the plasma is present the capacitors must be retuned, and the "off resonance" impedance $Z_{off} = R_{off} + jX_{off}$ is computed from the retuned values of $C_1$ and $C_2$. $Z_{ant}$ is shown on the top line of

| Freq. (MHz) | Condition | $C_1$(pf) | $C_2$(pf) | L($\mu$H) | R($\Omega$) | $\Delta$R($\Omega$) | $\Delta X_L$($\Omega$) | $R_{cur}$($\Omega$) |
|---|---|---|---|---|---|---|---|---|
| 10 | Vacuum | 531 | 45.7 | .44 | .31 | | | |
| | Plasma | 502 | 47 | .462 | .36 | .05 | 1.38 | .5 - .9 |
| 12 | Vacuum | 360 | 36 | .445 | .4 | | | |
| | Plasma | 347 | 38 | .46 | .485 | .085 | 1.13 | .6 - 1. |
| 14 | Vacuum | 270 | 28.7 | .433 | .456 | | | |
| | Plasma | 255 | 30.7 | .453 | .57 | .114 | 1.76 | .8 - 1.5 |
| 16 | Vacuum | 207 | 23.5 | .43 | .514 | | | |
| | Plasma | 190 | 25 | .46 | .668 | .154 | 3. | .9 - 1.2 |
| 18 | Vacuum | 165.6 | 20.5 | .42 | .6 | | | |
| | Plasma | 148.8 | 22 | .459 | .82 | .22 | 4.41 | .9 - 1.2 |

Table 5.1 Summary of the plasma loading impedance for 'off resonant' matching condition. R and L are the input resistance and inductance of the antenna measured under various conditions. The top line of each double rows is the data taken in vacuum and the second line corresponds to data taken in the plasma. $\Delta R = R_{off} - R_{ant}$ and $\Delta X_L = X_{off} - X_{ant}$ are the 'off resonant' plasma loading impedance. $R_{cur}$ is the range of the peak loading resistance obtained by using equation 4.3.1. The antenna is 1.1 inches into the tokamak chamber.

| Freq. (MHz) | Condition | $C_1$(pf) | $C_2$(pf) | L(μH) | R(Ω) | ΔR(Ω) | ΔX(Ω) | $R_{cur}$(Ω) |
|---|---|---|---|---|---|---|---|---|
| 10 | Vacuum | 525 | 44.5 | .445 | .3 | | | |
| | Plasma | 490 | 45.2 | .474 | .350 | .05 | 1.823 | .4 - .8 |
| 12 | Vacuum | 364 | 35.1 | .441 | .38 | | | |
| | Plasma | 352 | 37.5 | .453 | .456 | .076 | .86 | .8 - 1.2 |
| 14 | Vacuum | 264 | 27.8 | .444 | .448 | | | |
| | Plasma | 244 | 28.2 | .476 | .53 | .082 | 2.77 | .6 - 1. |
| 16 | Vacuum | 200 | 23.9 | .443 | .563 | | | |
| | Plasma | 192 | 26 | .455 | .7 | .137 | 1.2 | .6 - 1.3 |
| 18 | Vacuum | 161 | 20 | .432 | .604 | | | |
| | Plasma | 150 | 24.9 | .448 | 1. | .4 | 1.81 | .7 - 1.2 |

Table 5.2 Summary of another data set taken under similar conditions as the data presented in Table 5.1. This data set was taken on a different day than those given in Table 5.1.

columns 3 and 4 for each set of data with a given frequency, and $Z_{off}$ is on the bottom line. The contributions from the plasma alone to the "off resonance" impedance are shown in columns 7 and 8, where $\Delta R = R_{off} - R_{ant}$ and $\Delta X = X_{off} - X_{ant}$.

Two points must be emphasized about the condition under which these data were taken. First, as shown in Figure a.1 of Appendix a, the antenna impedance is a function of its distance into the tokamak vacuum chamber. This is because when the antenna is out of the vacuum chamber it sits in a 6 x 4 x 1" stainless steel port. This port can influence the antenna impedance by lowering its inductance and increasing its resistive losses through eddy current losses in the port wall. Also, the plasma loading depends on how far the antenna is into the chamber, since it is a function of the coupling coefficient of the antenna. When the antenna is completely out of the tokamak chamber and into the port, for example, the plasma loading is zero. The data presented in Tables 5.1 and 5.2 were taken with the antenna approximately 1.1 inches into the vacuum chamber.

## 5.3 Plasma Loading Resistance at the Cavity Resonances

The experimental results of the plasma loading resistance, R, at the various cavity modes are presented in this section. The plasma resistance is obtained from the power-current measurements discussed in Section 4.3. The equation used to compute the plasma loading resistance is reiterated here for the convenience of the readers (equation (4.3.1)):

$$R = (P_{inc} - P_{ref})/I_a - R_{ant}$$

where $P_{inc}$ and $P_{ref}$ are the incident and reflected power, respectively, $I_a$ is the antenna current, and $R_{ant}$ is the basic antenna resistance.

The presentation of the experimental data for the plasma loading resistance at the cavity resonances is divided into two parts. First, one set of experimental data taken at a given input frequency is presented as an example of the measured data and the computed results of the loading resistance. The general features of the data for other frequencies are described. Second, the magnitudes of the plasma loading resistance for the various cavity modes at different input frequencies are summarized in Tables 5.1 and 5.2. For each input frequency there are many cavity modes excited, each with a different loading resistance. Therefore, only the range of peak loading resistance for various cavity resonances at each input frequency is given in these tables. This range of the "resonant" loading resistance is denoted by $R_{cur}$, where the subscript 'cur' is to identify the power-current method used to determine the resistance, and to differentiate this result from the range of "resonant" loading resistance $R_{res}$ obtained from the measured complex reflection coefficient. The computed values of $R_{cur}$ and $R_{res}$ from experimental data are compared in Table 5.3.

Figure 5.4 shows a typical plasma discharge, where the input r.f. frequency is 11 MHz and the antenna is "off resonantly" tuned with the tuning capacitors $C_1$= 424 pf and $C_2$= 44 pf (see Figure 2.4). The "off resonance" tuning condition is indicated in the reflected voltage data, the 4th trace, where the reflected voltage is a minimum between the cavity resonances. Under the "off resonance" tuning condition, when

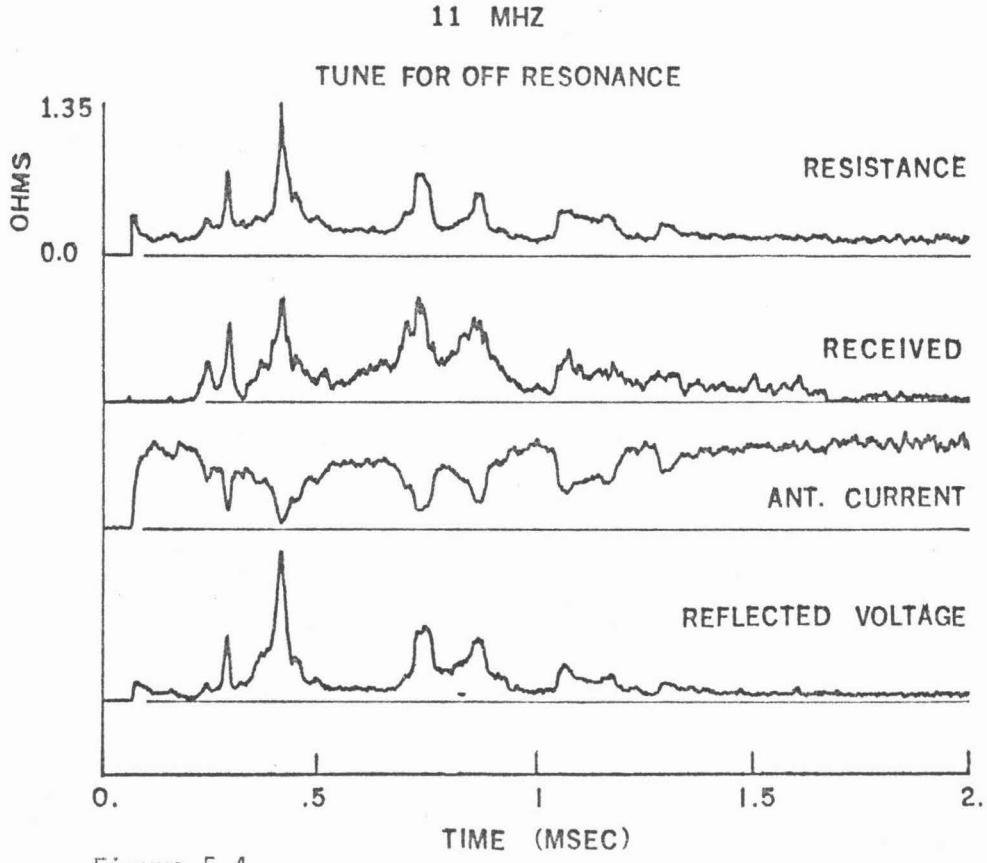


Figure 5.4

Calculated plasma loading resistance from the input power into the antenna and the antenna current data. Antenna is matched to 50Ω in the absence of the cavity resonances.

a cavity resonance appears, the generator impedance is no longer matched, and so the cavity resonances show up as increases in the reflected voltage from the directional coupler and decreases in the antenna current. These are the observed behaviors of the measured reflected voltage and antenna current as shown in traces 3 and 4.

The relation between the reflected voltage and the antenna current, i.e., an increase in the reflected voltage corresponds to a decrease in antenna current, can be understood as follows. Since the incident voltage is relatively constant throughout the plasma discharge, the amplitude of the reflection coefficients, $|\rho| = (V_{ref}/V_{inc})$ should be proportional to the amplitude of the reflected voltage. The antenna current can be expressed in terms of the reflection coefficient as:

$$I = V/Z$$

$$I = \frac{V}{Z_o}\left(\frac{1 - \rho}{1 + \rho}\right) \qquad (5.3.1)$$

where equation (2.6.5) is used to related Z and $\rho$, and $Z_o$ is the characteristic impedance. For a mismatch condition, the reflected voltage increases so the magnitude of the reflection coefficient will increase accordingly. The term $1/(1 + \rho)$ of equation (5.3.1) can be approximated by $(1-\rho)$ if the mismatch is small. Thus equation (5.3.1) can be written in the following approximate form:

$$I \simeq \frac{V}{50}(1 - 2\rho)$$

where $Z_o$ is taken to be 50 ohms. From this relation one can see that if

there is an increase in the reflected voltage, there must be a corresponding decrease in the antenna current. As a confirmation of this relation, the antenna current in trace 3 of Figure 5.4 has a minimum whenever the reflected voltage shows a maximum.

The general features of the time dependence of the peaks of the resonant loading resistance correlate well with the time dependence of the peaks in the transmitted signal. Whenever a peak in the transmitted signal occurs, a corresponding peak in the loading resistance appears at the same time. Moreover, the density dependence of the resistive loading peaks is the same as the transmission peaks. When the input frequency is low, most of the resistive peaks occur near the density maximum, whereas at the higher frequencies, the peaks become more spread out.

An observation in the experiment is that the modes with the largest transmission amplitude are not necessarily the ones that show the largest input loading resistance. This is because the input loading resistance measures the power delivered into the cavity, whereas the receiving probe only detects one component of the field. Depending on the cavity mode that is excited, strong input loading does not necessarily correspond to a strong field component measured by the probe.

In Tables 5.1 and 5.2, the ranges of the peaks of the resonant loading resistance, $R_{cur}$, for the different modes at various input frequencies are summarized. The resistance values are calculated using equation 4.3.1 in the same fashion as the data shown in Figure 5.4. Only

loading peaks that are substantially above the noise level are kept. In the same tables, the "off resonance" plasma loading resistances, i.e., $\Delta R = R_{off} - R_{ant}$, for the same plasma shots are presented as a comparison to the peak "resonant" plasma loading resistance, $R_{cur}$.

## 5.4 Reproducibility of the Plasma Loading Resistance Measurement

Even with the same input frequency, the magnitude of the resistive loading at the various cavity modes has been observed to be different for different plasma shots. For two consecutive plasma discharges, the resistive loading may be strong at certain cavity modes on one shot, yet appears weaker for the same modes on the next shot. One possible explanation for this behavior in the plasma loading is that the radial density profile of the plasma is not completely reproducible for different plasma discharges. As shown by Paoloni in a recent paper, the coupling coefficient of the transmitting antenna depends on the radial density profile [18]. For the low radial and poloidal modes, which are believed to be the observed modes here, the radial dependence of the r.f. magnetic field for a uniform density profile is quite different than that of a parabolic density profile. The strength of the magnetic field components at the outer radius of a cylindrical cavity is weaker for a parabolic density profile than a uniform density profile. (The uniform density profile used here has the same line-average density as the parabolic profile.) Since the antenna is located at the outer edge of the tokamak, the coupling coefficient of the antenna should be higher for a uniform density profile than a parabolic profile. (For more details of the theory see the paper by Paoloni). The position of the plasma

column in the tokamak in some sense can be thought of as a radial density profile. The coupling coefficient will depend on whether during the first two msec of the discharge the plasma column is near the outer wall of the tokamak where the transmitting antenna is located, or it is formed initially near the inner wall. Since there is no radial profile measurement in our experiment, this is only a possible explanation of the fluctuation in the magnitude of the resonance loading resistance. It must be pointed out here that there were some judgmental factors in the data taking. Only shots with strong cavity mode loading were kept and those with weak loading were discarded. Therefore, the range of the cavity mode loading presented in Tables 5.1 and 5.2 are examples of the strong loading cases.

## 5.5 Complex Plasma Loading Impedance Measurement

As indicated in the introduction, the main emphasis of this thesis is on the measurement of the complex plasma loading impedance of the cavity modes. The real part of the impedance, as mentioned previously, is important in the determination of the efficiency of wave generation in the tokamak. The complex loading impedance is important in determining how to match the generator impedance to one of the cavity resonances. Only by matching the generator impedance to a cavity resonance can the maximum power be delivered to the cavity when the plasma loading is highest.

The experimental data in this section are presented in the same way as in Section 5.2. Experimental results for two input frequencies, 11 MHz and 16 MHz, are shown in Figures 5.5 and 5.6, and the general behavior of the complex input impedance for the various input frequencies are discussed. Then the complex impedance data for the various input

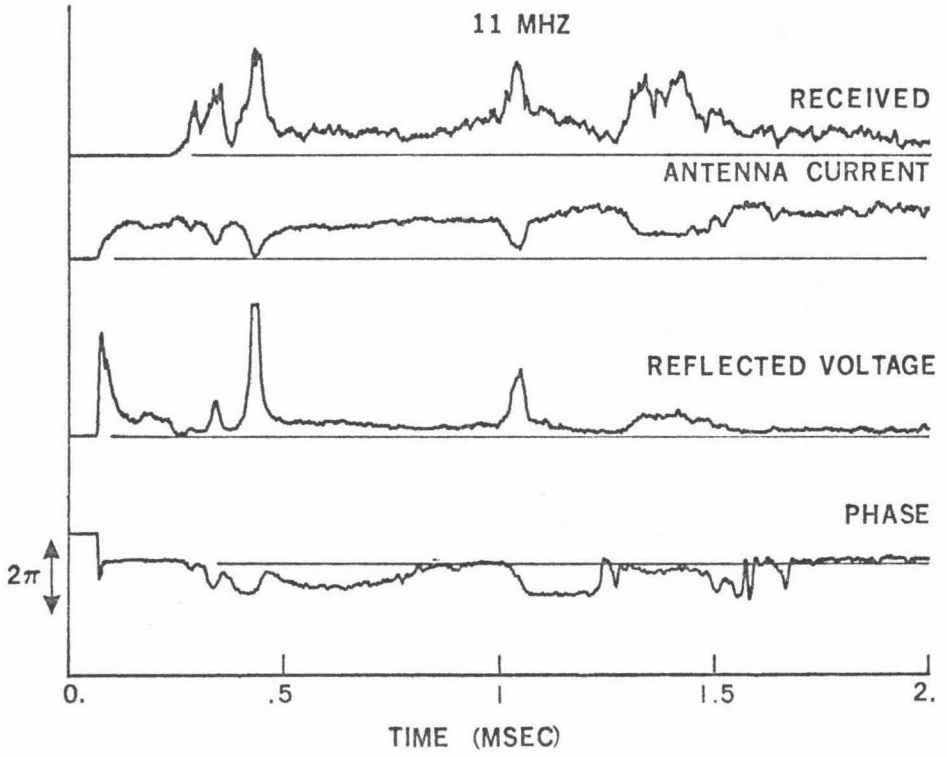


Figure 5.5

Measured phase different between the incident and the reflected waves using a VHF directional coupler.

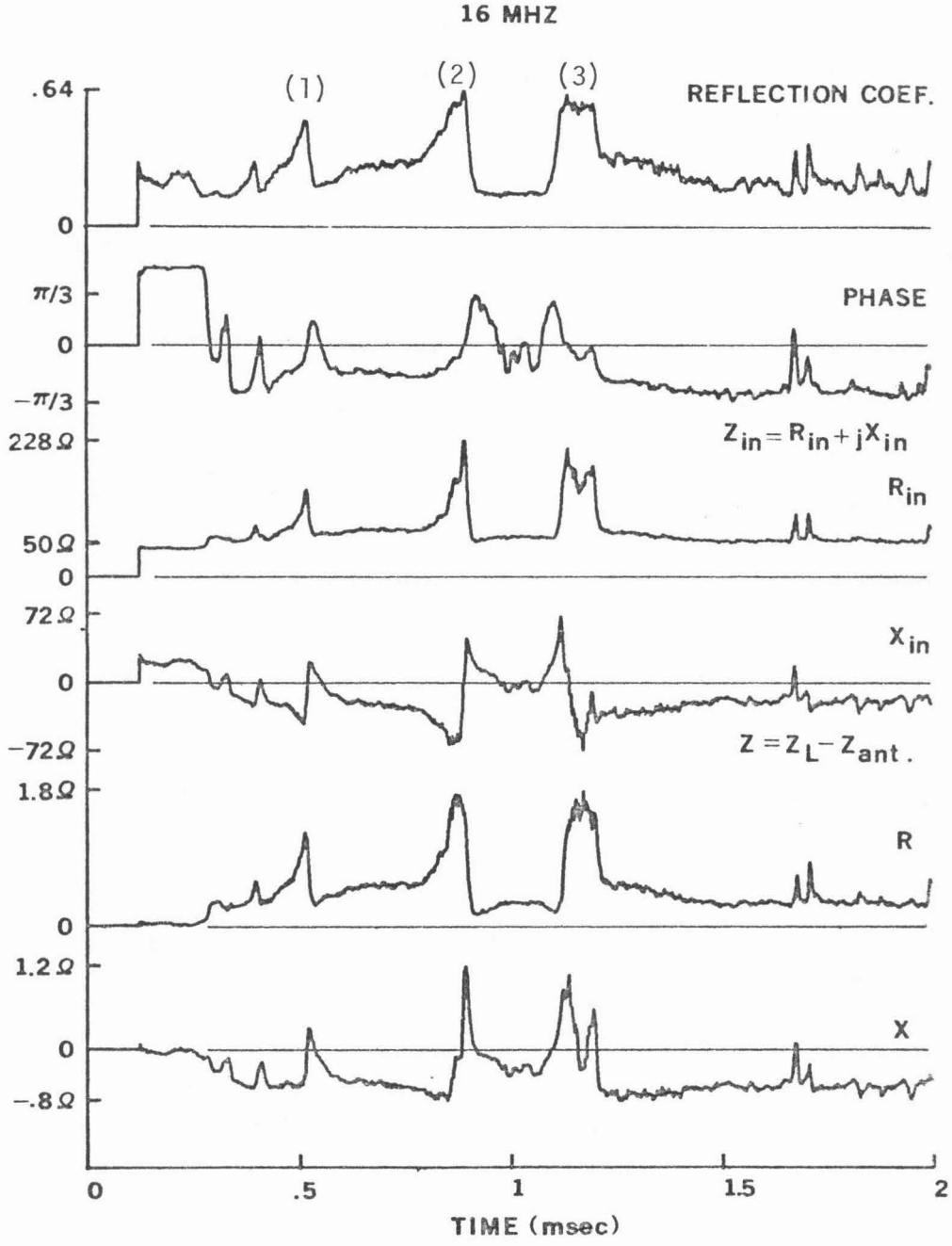


Figure 5.6

Computed complex plasma loading impedance from the complex reflection coefficient. The three identified peaks correspond to the three Q circles shown in Figures 5.7 to 5.9.

frequencies are summarized in Table 5.3.

The physical quantities actually measured in the complex plasma loading impedance experiment are the incident voltage, the reflected voltage, the phase difference between the incident and reflected waves, the antenna current, the transmitted signal, and the plasma density. The incident voltage, as mentioned earlier, is fairly constant during the plasma discharge. The antenna current is measured so that the resistive loading can be calculated using the power-current equation as a check for the real part of the complex loading impedance. Figure 5.5 shows a set of experimental data for an input frequency of 11 MHz. When the third and fourth traces of Figure 5.5 are compared with the second and third traces in Figure 2.7, one can see that there is general agreement between theory and experiment as to how the reflected voltage and the phase between the incident and reflected waves pass through a cavity resonance. Here it is assumed that the incident voltage is constant enough so that the reflection coefficient follows the trends of the reflected voltage. As expected, corresponding to every peak in the reflected voltage, there is a steep change in the measured phase.

Figure 5.6 contains a typical set of circuit parameter results computed from the measured data for an input frequency of 16 MHz. This set of data was taken with the antenna "off resonantly" matched. The first trace in the figure is the amplitude of the reflection coefficient, and it is calculated from the incident and reflected voltage data using equa-(4.4.1). The phase data in trace 2 are the direct output of the phase detector. From the complex reflection coefficient, the complex input impedance, $Z_{in}$, can be calculated from equations (2.6.6) and (2.6.7).

The results of this calculation are shown in traces 3 and 4. When these data are compared with the calculated values shown in the fourth and fifth traces in Figure 2.7, the general features of the data seem to agree well with the computed results from the circuit model. For the experimental data in Figure 5.6, the plasma density reaches a maximum at time = 1 msec. At this time the slope of the density evolution reverses in sign, so as stated before, both the phase and the reactance should reverse in direction. From the second trace of Figure 5.6 one can see that the direction of the change in phase is reversed at around time = 1 msec. Furthermore, the direction of change in the reactance shown in the fourth trace of Figure 5.6 is very similar to the fifth trace in Figure 2.7. The measured reactance goes negative before passing through a resonance during the density buildup and goes positive before passing through a resonance during the density decay. This is the same behavior as the computed results using a similar density evolution.

The next step in the calculation is to compute the plasma loading impedance $Z = R + jX$ by transforming $Z_{in}$ across the matching network using equations (2.5.1) and (2.5.2) and subtracting the impedance of the antenna, $Z_{ant}$. Before making this calculation, the capacitances of the elements in the matching network must be measured. For this set of data $C_1$ = 190 pf and $C_2$ = 34 pf. The results of the computation are shown in traces 5 and 6 of Figure 5.6. The maximum resistive loading is about 1.8 ohms here in comparison with 1.2 ohms, the value of the maximum plasma resistive loading obtained from the power-current method. From

Appendix a, the antenna resistance at 16 MHz is about .56 ohms, therefore the plasma loading is between two and three times the antenna resistance. This corresponds to a wave generation efficiency $\eta$ between 70% to 80%.

The ranges of the complex plasma loading impedance of the various input frequencies are summarized in Table 5.3 in a manner similar to that of Tables 5.1 and 5.2. The format of Table 5.3 is the same as Tables 5.1 and 5.2, except the plasma contribution to the "off resonant" loading impedance, $\Delta R$ and $\Delta X$, is not shown. They can be obtained by taking the difference of the values in the two lines under columns 5 and 6. The input frequencies of the experiments are given in column 1. The condition under which the data were taken is shown in column 2. The capacitances of $C_1$ and $C_2$ needed to match the generator impedance to the antenna and the antenna plus "off resonant" plasma are shown in two lines , columns 3 and 4, respectively. Column 7 shows the range of the peaks of the loading resistance $R_{cur}$ for the particular data set. It is obtained from the input power and the antenna current in the same fashion as the data presented in the 9th column of Tables 5.1 and 5.2 (see equation (4.3.1) for this calculation). This range of loading resistance $R_{cur}$ is presented here as a comparison to the real part of the complex loading impedance calculated from the complex reflection coefficient measured in the experiment. The complex plasma loading impedance $Z$ is calculated from equation (2.8.1), where the antenna impedance has been subtracted. The real and imaginary parts of the impedance are given as

$$R = R_L - R_{ant} \qquad X = X_L - X_{ant}$$

| Freq. (MHz) | Condition | $C_1$(pf) | $C_2$(pf) | L( μH) | R(Ω) | $R_{cur}$(Ω) | $R_{res}$(Ω) | $X_{res}$(Ω) |
|---|---|---|---|---|---|---|---|---|
| 10 | Vacuum | 532 | 44.5 | .44 | .293 | | | |
| | Plasma | 509 | 46.1 | .457 | .34 | .5 to 1. | .6 to 1.1 | -.52 to .6 |
| 12 | Vacuum | 364 | 34.8 | .442 | .375 | | | |
| | Plasma | 352 | 37 | .453 | .445 | .4 to .7 | .75 to 1.1 | -.6 to .8 |
| 14 | Vacuum | 262 | 28.4 | .446 | .472 | | | |
| | Plasma | 256 | 32 | .45 | .61 | .7 to 1.3 | .9 to 1.46 | -.7 to 1. |
| 16 | Vacuum | 199 | 23 | .446 | .53 | | | |
| | Plasma | 189 | 27 | .459 | .77 | 1. to 1.5 | 1.2 to 1.8 | -.8 to 1.2 |
| 18 | Vacuum | 161 | 20.8 | .43 | .65 | | | |
| | Plasma | 146 | 24 | .461 | .98 | .82 to 1.7 | .95 to 2. | -.9 to.8 |

Table 5.3 The ranges of the complex plasma loading impedance, $R_{res}$ and $X_{res}$, at the various cavity modes are given in columns 8 and 9. The resistive loading at the same cavity modes measured with the power-current method is shown in column 7. $C_1$ and $C_2$ are the values of the tuning capacitors. R and L are the antenna resistance and inductance with or without plasma. The data were taken under 'off resonant' tuning condition and the antenna is at 1.1 inches into the tokamak chamber.

where $R_L$ and $X_L$ are given in equations (2.5.1) and (2.5.2). The range of the complex loading impedance maxima at the various cavity resonances are given in columns 8 and 9. The 8th column shows the range of the plasma loading resistance maxima, $R_{res}$, for the various cavity modes. These ranges seem to agree generally with the data, $R_{cur}$, measured using the antenna current. The discrepancies between the data obtained from these two methods as shown in columns 7 and 8 can be attributed to errors in the calibrations of the instruments used in the measurements. Column 9 shows the range of the reactance, $X_{res}$, for the largest resonance peak measured in the particular plasma discharge. As shown in the sixth trace in Figure 5.6, this reactance changes sign rapidly as a cavity resonance is passed through.

As indicated previously, the cavity resonance effect can be seen more readily when the complex cavity input impedance is plotted in the complex impedance plane. When the real and imaginary parts of the impedance are plotted against each other as they pass through a resonance, the resultant curve is a circle, known as the Q circle. Figures 5.7, 5.8 and 5.9 are the experimental Q circles of the three major peaks which occur at time = .5 msec, time = .9 msec, and time = 1.1 msec in Figure 5.6. The time between the points in the Q circle plots is 2 microseconds. They are approximately circles, although there are some distortions. The distortions in the Q circles can be divided into two classes, depending on how fast the density is changing as a function of time. The first class is when the density is changing slowly enough with time that the condition for meaningful impedance measurement, the inequality (2.4.5), is satisfied:

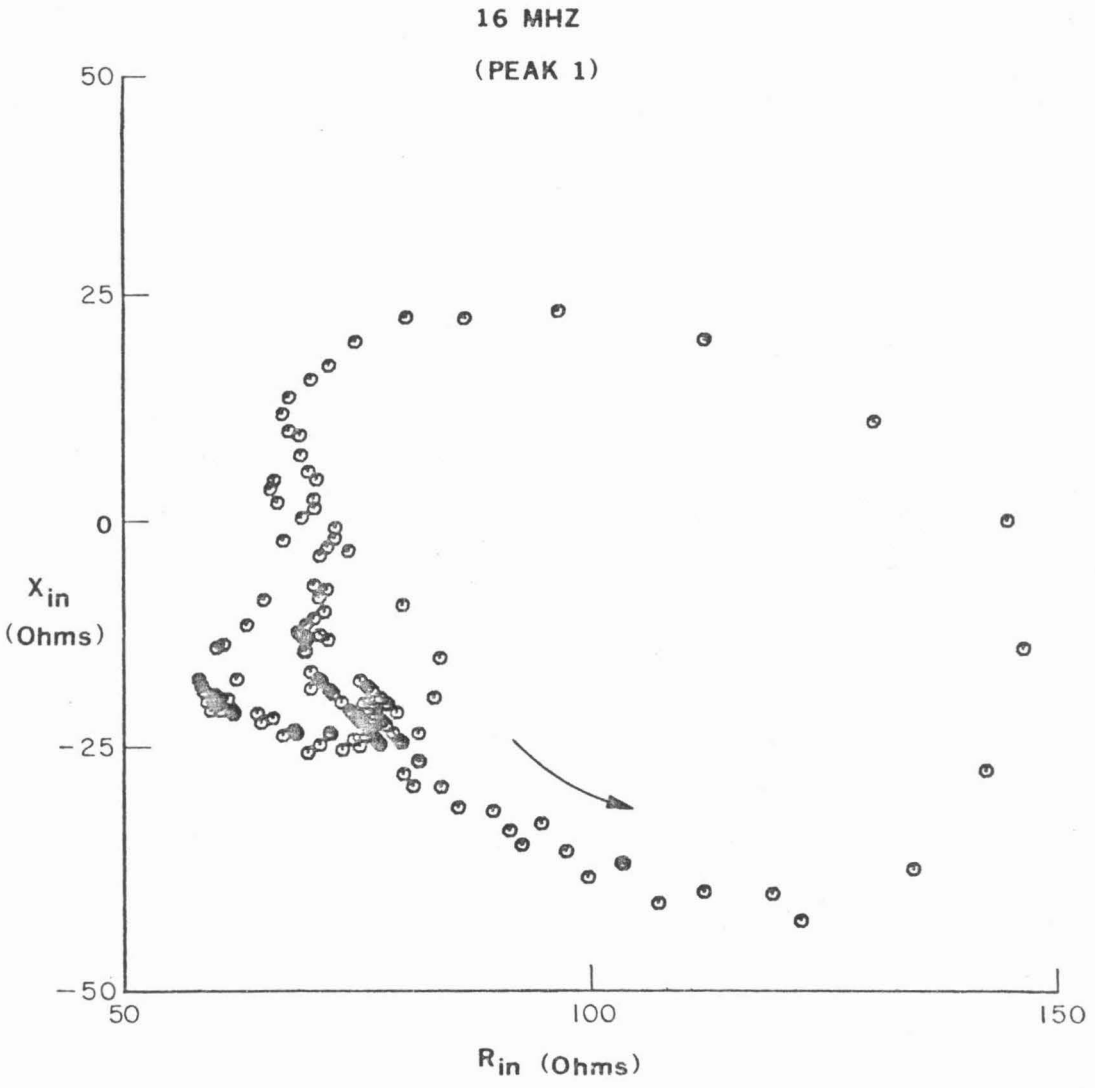


Figure 5.7
Q circle for the first peak shown in Figure 5.6. The circle is traced out counterclockwise, and the time between consecutive points is 2 μsec.

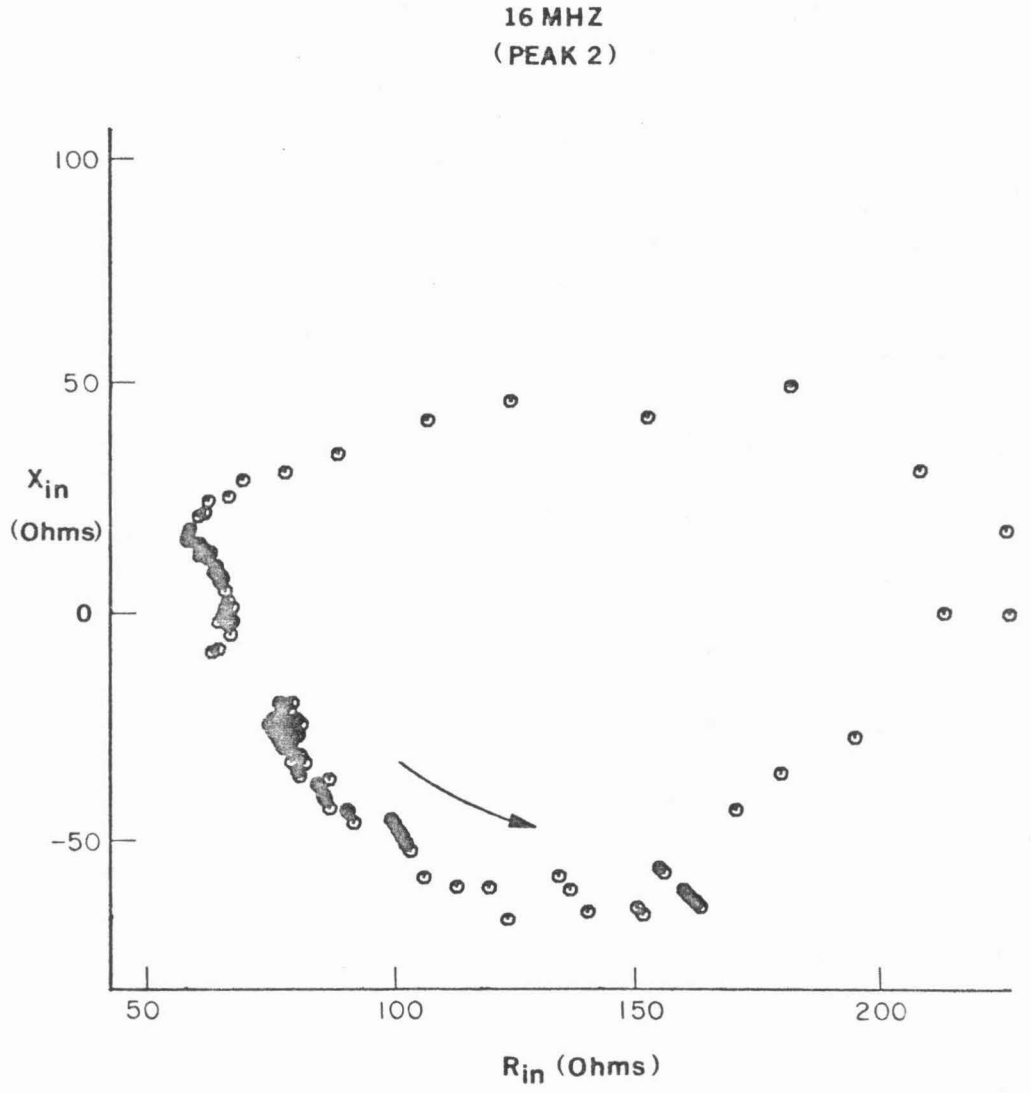


Figure 5.8
Q circle for the second peak shown in Figure 5.6. The circle is traced out counterclockwise, and the time between consecutive points is 2 μsec.

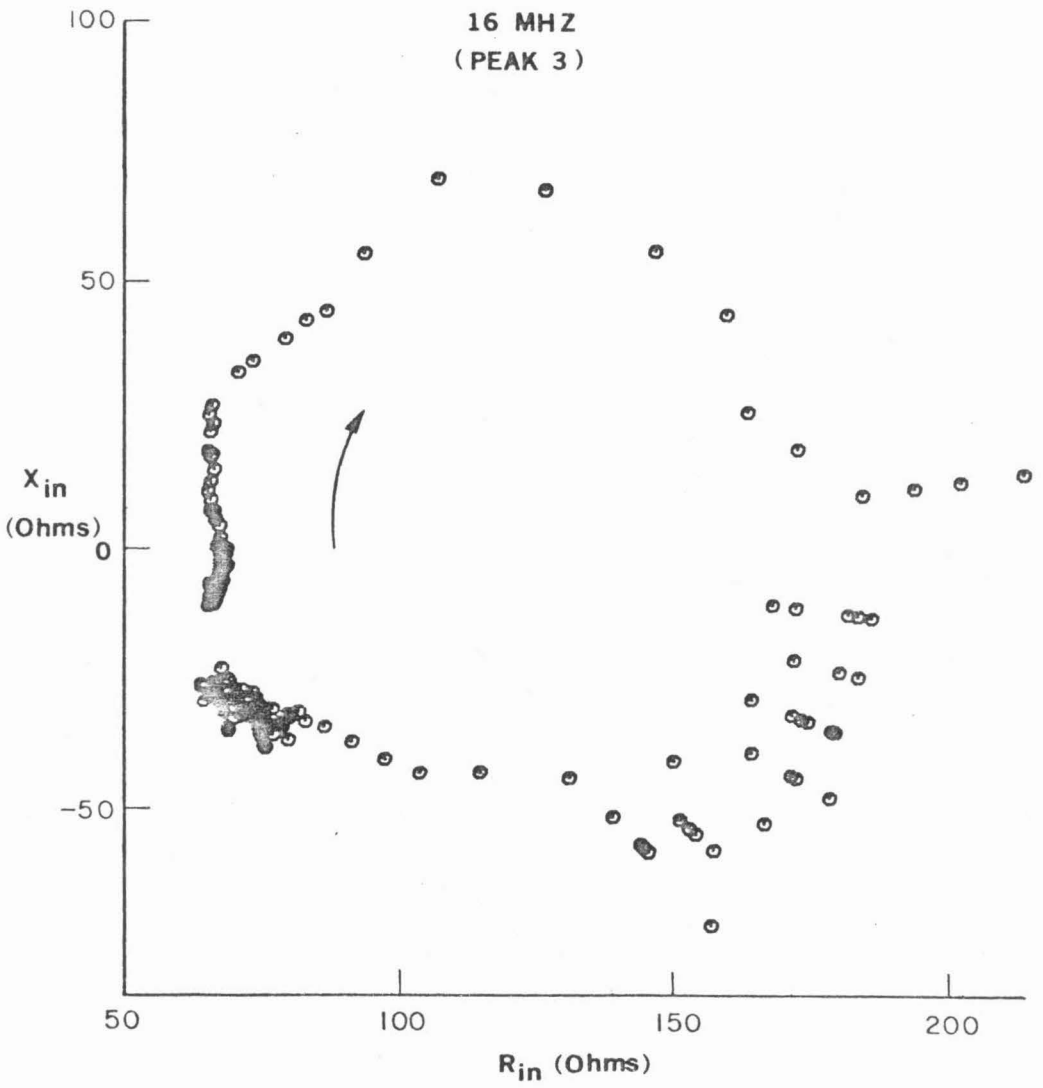


Figure 5.9
Q circle for the third peak shown in Figure 5.6. The circle is traced out clockwise, and the time between consecutive points is 2μsec.

$$T >> 2Q_L/\omega_o$$

where T is the time between the half-power points of the resonance peaks, $\omega_o$ is the resonance angular frequency, and Q is the loaded Q of the cavity. (This inequality is examined in detail for various cases in Section 5.6, where the Q of the cavity is calculated.) In this case the cavity modes are swept through much slower than the response time of the output operational amplifier of the crystal detectors, 4V per 2 μsec, and the response time of the phase detector, 2π per 4μsec. The Q circles shown in Figures 5.7, 5.8, 5.9, are observed under this kind of condition where the distortions from a circle are not large. The distortions of the Q circles shown in Figures 5.7 through 5.9 can be partly attributed to errors in the calibration of the square law crystal detector, the linear phase detector, and partly to density fluctuations. The effects of the density fluctuations are most obviously observed in Figure 5.9 where small oscillating points are superimposed on the main circular curve.

The second class of distortion in the Q circles is when the density changes so fast that the condition $T \sim 2Q/\omega_o$ is approached. In this case the limits of the response times of the phase and crystal detectors are also approached. The resultant Q circles are greatly distorted, usually becoming a very flat ellipse. Data of these kind are discarded, since the impedance information from them is not meaningful.

As mentioned before, the direction in which the Q circles are traced out as the cavity resonance is passed through is a function of

the sign of the slope of the density evolution. The first two peaks shown in Figures 5.7 and 5.8 are traced out counterclockwise as the cavity resonance is passed through. When the time is around one millisecond in Figure 5.6, the density reaches a maximum, so the slope of the density evolution is reversed in sign after this point. Therefore, the resonance shown in Figure 5.9 is traced out in the clockwise direction, opposite to the previous two peaks. This behavior is what the circuit model has demonstrated.

## 5.6 Cavity Q, Antenna Coupling Coefficient, and Antenna Efficiency

### a. Cavity Q

By using the approximate density-frequency relation for the cavity mode cutoffs, the Q of the plasma-filled cavity can be simply estimated. The method used to estimate the cavity Q is described in Section 2.6, and the Q is related to the density by the following equation:

$$Q = (2n_e/\Delta n_e)_{3dB}$$

As mentioned in Section 2.4, the Q obtained from the density measurements is the loaded Q of the cavity, and the unloaded Q of the cavity can be related to the loaded Q by equation (2.6.11) at a cavity resonance by

$$Q_o = Q_L(1 + \omega^2 M^2/2R_{off}R_p)$$

All the quantities in this equation have been measured experimentally or can be calculated from experimental data. $Q_L$ is derived from the density measurements. $R_{off}$ is the antenna resistance plus the resistive contribution from the plasma when the cavity resonances are not present.

It can be calculated from the values of the capacitors that are used in the matching network to tune the antenna "off resonantly". $R_{off}$ is derived from the following equation:

$$R_{off} = R_{in} X_{C_1}^2 / [(X_{C_1} + X_{C_2})^2 + R_{in}^2]$$

where $R_{in}$ is 50 ohms, and $X_{C_1}$ and $X_{C_2}$ are the capacitive reactance used to tune the antenna "off resonantly". The quantity $\omega^2 M^2 / R_p$ is merely the loading resistance measured at the resonance of one of the cavity modes. From equation (2.2.2a) this factor can be related to the difference between $R_L$ and $R_{ant}$ at the resonance frequency of one of the modes, i.e., at $\Omega_p = 1$:

$$\omega^2 M^2 / R_p = (R_L - R_{ant})_{max}$$

The 3 dB drop-off points in the reflected voltages can be obtained from the experimental data. As an example, the $Q_L$ and $Q_o$ for the three major resonance peaks are given in the second and third column or Table 5.4, respectively.

| Cavity Resonance Peaks | Loaded Cavity Q [$Q_L$] | Unloaded Cavity Q [$Q_o$] | Coupling Coefficient [$\kappa^2$] | Antenna Efficiency [$\eta$] |
|---|---|---|---|---|
| 1 | 240 | 470 | $5.6 \times 10^{-5}$ | 70 % |
| 2 | 240 | 560 | $6.5 \times 10^{-5}$ | 77 % |
| 3 | 170 | 400 | $8.3 \times 10^{-5}$ | 75 % |

Table 5.4 The estimated loaded Q, unloaded Q, antenna coupling coefficient, and the antenna efficiency for the three resonance peaks shown in Figure 5.6. The antenna $Q_a$ used in the computation is 90.

It must be emphasized that this way to obtain the Q of the cavity is only an estimate. Furthermore, there is an experimental error in the measured density, as stated in Section 3.1d. That is, there is an uncertainty factor of ±1/4 fringe in the fringe counting method of the density measurement with the microwave interferometer. The estimated Q for the cavity resonances with different input frequencies does not differ greatly. For the frequency range used in the experiment, between 10 and 16 MHz, the range of the loaded Q is between 120 and 250, and the range of the unloaded Q is between 400 and 700.

The contribution to the measured cavity Q can be divided into two parts: the damping of the wave by the plasma, and the energy losses due to the finite conductivity of the tokamak wall which is made of stainless steel. As noted in the introduction, there have been several theories on the damping mechanism of the magnetosonic wave by the plasma [4,8,25]. The theories are quite involved, so it is left to the interested reader to look up the references. It is important here to estimate the losses in the tokamak wall to see whether the wall loss is a dominating factor. The calculated cavity Q for a cold plasma-filled cylindrical cavity with stainless steel wall is presented in Appendix c. The estimation is for the m = 0 poloidal mode, the low radial and the axial modes. This is a lower limit on the estimated cavity Q. The calculated cavity Q with wall loss is about 1300, which is two to three times higher than the measured cavity. Therefore, although the wall loss is not small, it is not the dominating term in the measured cavity Q, and so a large part of the wave energy should be absorbed by the plasma.

Since the Q in the experiment has been obtained, it is appropriate at this point to go back to the inequality (2.4.5) and see whether the impedance measurements in our transient system are valid. Restating (2.4.5),

$$T >> 2Q/\omega_o$$

where T is time between the half voltage points in the resonance peaks, and $\omega_o$ is the resonance frequency. Every resonance datum taken in the experiments has been substituted into this inequality to check for the validity of the impedance measurement. Those data that do not satisfy the inequality because the resonances are swept through too quickly by the density are discarded. As an example, let us check the three peaks in Figure 5.6. Since the experiment was performed with the input antenna coupling strongly to the tokamak, the Q used in the calculation is the loaded $Q_L$ of the cavity.

For the first peak, T = 24 μsec, $Q_L$ = 240, and the angular frequency $\omega_o = 2\pi \times 16 \times 10^6$ rad/sec. Therefore, $2Q_L/\omega_o$ = 5 μsec, which is smaller than T, and so the impedance measurement of this resonance is valid.

For the second peak, T = 30 μsec, $Q_L$ = 240, and the angular frequency is the same as above. Therefore, $2Q_L/\omega_o$ = 5 μsec, which is again smaller than T.

For the third peak, T = 50 μsec, $Q_L$ = 170, and $\omega_o$ is the same as above, therefore $2Q_L/\omega_o$ = 4 μsec, which is smaller than T.

As one can see, all three of the peaks in this data set satisfy the inequality, and so the impedance measurement is valid. When this test is given to other data at various input frequencies, there are cases where the density changes so fast that this inequality is no longer satisfied.

These data can usually be picked out during the experiment and discarded right away. In future experiments this constraint will not occur, because a gas puffing system is presently being installed on the tokamak to keep the density higher and more constant as a function of time (see Section 6.2 for details).

b. Antenna Coupling Coefficient

With the complex impedance and the Q measurements, the coupling coefficient of the antenna can be calculated using equation (2.6.12)

$$\kappa^2 = (R_L/R_{ant} - 1)/Q_a Q_p$$

where again this is for an "off-resonantly" tuned system. Since the Q of the cavity is an estimate, the coupling coefficient should be called an estimate as well. As mentioned in Appendix a, the coupling coefficient is a function of the distance that the antenna protruded into the vacuum chamber. For the different cavity modes at various input frequencies, the coupling coefficient of the antenna when it is 1.1 inches into the tokamak chamber has a range between $3 \times 10^{-5}$ and $1 \times 10^{-4}$. As an example, consider again the data in Figure 5.6 which were taken with the antenna at 1.1 inches into the tokamak. The coupling coefficient, $\kappa^2$, for the three peaks shown in Figure 5.6 are given in the third column of Table 5.4.

c. Antenna Efficiency

Once both the cavity Q and the antenna coupling coefficient are estimated, the wave generation efficiency, $\eta$, of the present two-turn copper loop antenna can be estimated from equation (2.7.2),

$$\eta = \kappa^2 Q_a Q_p/(1 + \kappa^2 Q_a Q_p)$$

The antenna efficiency for the three resonance peaks in Figure 5.6 are given in column 5 of Table 5.4. The efficiency for the present antenna system has been observed as high as 80%. Possible ways to increase the antenna efficiency are elaborated in Section 6.2.

## 5.7 Matching Impedances at the Cavity Resonances

For future high power experiments, it is essential to be able to match the generator impedance at one of the cavity resonances where the resistive loading of the cavity is high. This process is much more difficult than matching "off resonantly", because during the passage through of a resonance both the real and imaginary parts of the impedance are changing very fast. Very precise tuning is required to transform the resistance to 50 ohms and tune out the reactance at one of the cavity resonances. In our experiment the difficulty is compounded by the fast density decay as a function of time. This makes tuning "on resonance" harder because sometimes it is difficult to tell whether the tuning is exactly on resonance or just slightly mistuned, because the resonance peaks are so sharp. Before presenting the data in our experiment, some improvements to the measurement system so that "on resonant" tuning will be easier are discussed.

First, if the change in the density is slower, the tuning process would be easier. Recently, a gas puffing system has been installed on our tokamak to puff neutral gas, which can diffuse across the confinement magnetic field, into the tokamak plasma. The neutral gas is ionized in the plasma, thus increasing the plasma density. By puffing the gas at the appropriate time in the plasma discharge, the fast decay in the density after the initial buildup as shown in Figure 3.3 can be compensated,

and the density evolution can be kept constant to about 10% for a substantial portion of the discharge. This way the cavity modes are swept through much slower by the density evolution, and so the resonant peaks appear broader. Second, the better procedure for "on resonant" tuning, as mentioned in Section 2.5, is first to match the impedance of the generator at the "off resonant" condition, which is an easier process than "on resonance" tuning. If an on-line computer system is available, the plasma loading impedance $Z_L$ at a cavity resonance can be calculated from the measured complex reflection coefficient, $\rho = V_{ref}/V_{inc}\ e^{i\phi}$, where $\phi$ is the phase difference between the incident and the reflected waves. By using equations (2.5.1) and (2.5.2), the input impedance at the antenna, $Z_L$, can be calculated from the input impedance at the impedance matching circuit, $Z_{in}$, and the values of the capacitors, $C_1$ and $C_2$, used to "off resonantly" tune the antenna. Once the values of $Z_L$ at the various cavity resonances are known, the capacitances $C_1$ and $C_2$ can be recalculated for matching to one of the cavity modes. Recently, a minicomputer was acquired for on-line operation with our tokamak. With the aid of the computer, "on resonant" matching will be easier for future experiments.

The actual "on resonant" tuning reported in this thesis was done by minimizing the reflected voltage from the directional coupler at one of the cavity modes through trial and error. The experimental data of the reflected voltage and r.f. current for the "on resonant" matching experiment appear just opposite to the data from the "off resonant" tuning experiment. Under the "off resonant" matching condition, the reflected voltage is minimized and the antenna current is maximized between the cavity modes; whereas for the "on resonant" matching condition, the

reflected voltage is minimized and the antenna current is maximized at one of the cavity modes. For the "on resonant" matching condition, the reflected voltage is high and the antenna current is low between the cavity modes, because the antenna is mismatched to the generator without the cavity modes. Since the matching conditions for the various cavity modes are different, only one mode can be exactly matched for a given setting of $C_1$ and $C_2$.

Two of the "on resonantly" tuned cases are given in Figures 5.10 and 5.11. As indicated before, only one mode is properly matched for each case. For the data in Figure 5.10, the tuning capacitances needed to tune "on resonantly" are $C_1$ = 210 pf and $C_2$ = 38 pf, and for the traces in Figure 5.11, $C_1$ = 336 pf and $C_2$ = 49.5 pf.

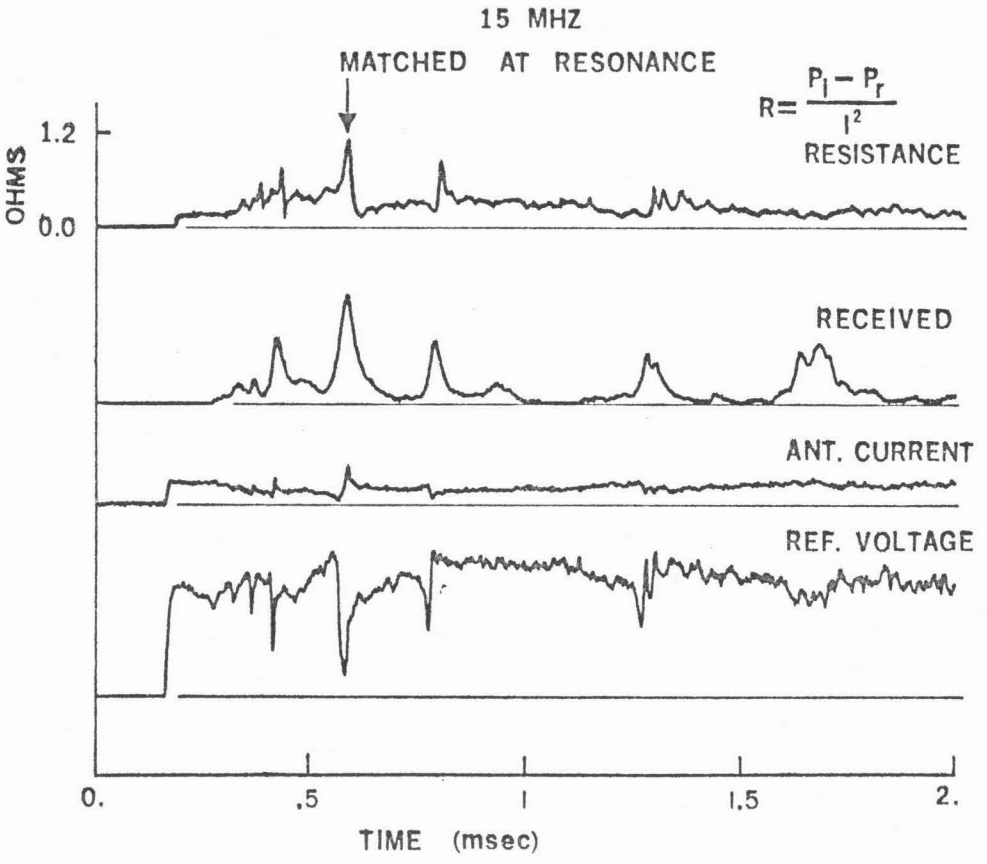


Figure 5.10

Antenna is matched to 50 ohms at one of the cavity resonances.

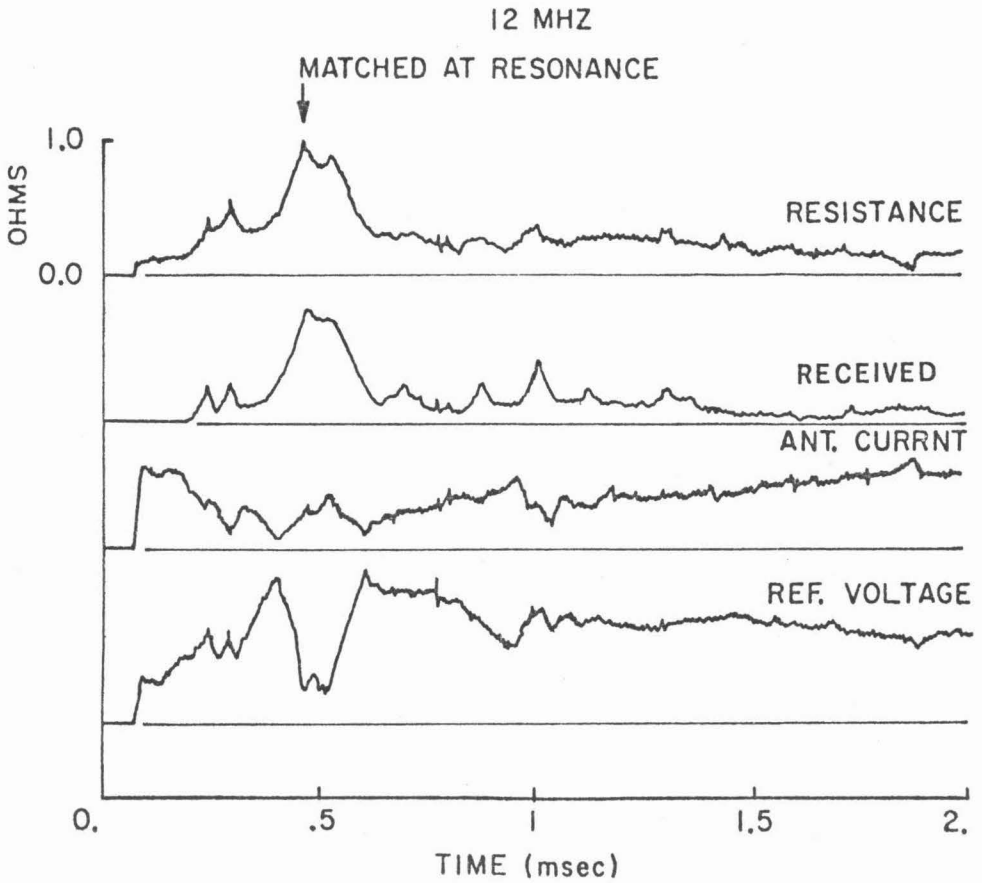


Figure 5.11

Antenna is matched to one of the cavity resonances.

# VI. CONCLUSIONS

## 6.1 Summary

This thesis has presented the results of some low power experiments in the propagation of the fast magnetosonic cavity modes in a research tokamak. A great deal of attention has been given to the study of the complex input impedance of the antenna, the antenna design, and the design of the impedance matching network. These measurements are of great importance to future high power experiments where efficient coupling of power to the plasma is essential. Through the high power heating experiments the feasibility of using magnetosonic waves as a method to heat the plasma to fusion ignition can be evaluated.

The toroidal cavity modes could be readily observed in transmission measurements, where they appeared as a series of maxima in the transmission amplitude. The measured eigenmode dispersion relation seemed to agree qualitatively with the results from the simple theory for a cold cylindrical uniform plasma cavity. Although mode numbers were not determined, the manner in which the phase between the transmitting and the receiving signal changed indicated that when passing through a cavity resonance the received amplitude peaks were due to cavity resonances.

After carefully designing a low-loss transmitting antenna and a low-loss matching network, the cavity resonances were seen in the input impedance of the cavity. When the antenna was "off resonantly" matched, the cavity modes appeared as maxima in the reflected voltage detected by the input directional coupler, and as minima in the antenna current. By dividing the input power by the antenna current squared, the loading

resistance of the plasma was calculated. The loading resistance at the various resonances was observed to be as high as three to four times the basic antenna resistance.

The phase difference between the incident and the reflected input voltages has been investigated. The phase information, along with the amplitude of the incident and reflected waves, gives the complex reflection coefficient. The complex input impedance was derived from the complex reflection coefficient. The real part of the complex impedance determined this way agrees well with the results from the loading resistance from power-current measurements. The complex impedance followed the predicted characteristics of a circuit model often used in microwave cavity theory. The model, along with a set of reasonable assumptions, gave the general features of the measured impedance function. The measurement of the complex plasma loading impedance is crucial to the understanding of how to match the generator impedance to one of the cavity modes.

In order to deliver the maximum amount of power at resonance, it is necessary to match the antenna impedance plus the plasma loading impedance to the generator impedance at one of the resonance peaks. This way the maximum amount of power can be fed into the tokamak when the plasma loading is high. Although this was a difficult experimental task, due to the fast changing nature of the impedance near resonance because of rapid decay of the plasma density, we were able to match impedances at a few of the resonances. In future experiments the "on resonant" matching of the generator could be aided by improvements recently acquired. First, an on-line computer has been acquired so that once the complex plasma loading impedance of the cavity modes is measured under the "off resonant" matched

condition, the required values of the circuit elements in the matching network can be readily computed. By resetting the matching circuit elements to the new values, the generator impedance can be matched to the antenna impedance at one of the cavity modes. Second, the density of the plasma can be held more constant by gas puffing, so that resonances would be swept through much more slowly.

From the approximate cut-off relation of the cavity modes in cold plasma theory, the loaded $Q_L$ of the cavity could be estimated. The unloaded $Q_o$ of the cavity could be derived from the $Q_L$ by a circuit transformation. The measured unloaded $Q_o$ of the various cavity modes ranges from 400 to 700. Finally, the antenna coupling coefficient $\kappa^2$ was obtained from the plasma loading impedance and the estimated cavity Q. The range coupling coefficients for the various cavity modes are between $3 \times 10^{-5}$ and $1 \times 10^{-4}$ for the 2-turn antenna.

The general conclusions for these experiments are that the possibility for efficient power coupling into the plasma-filled cavity looks very encouraging because of the reasonable plasma loading resistance found at the cavity resonances. The matching of the generator impedance to the antenna impedance at resonance does not seem to be a serious problem. The loading resistance at the cavity modes has been observed to be as high as three to four times the antenna resistance, and the generator impedance has been matched to a few of the cavity modes, if only briefly due to the changing density. This means that with the present antenna design, as much as 80% of the power can be delivered into the tokamak via the cavity resonances, and only 20% of the input power will be lost in the antenna.

## 6.2 Future High Power Heating Experiments

From the results of the low power experiments, one can see that a few improvements of the experimental setup must be made before an efficient high power heating experiment can be performed.

First, in order to improve the efficiency of the wave generation in the tokamak, the antenna design can be improved in the following ways. Looking back at the equation of the antenna efficiency, $\eta$

$$\eta = \kappa^2 Q_a Q_p / (1 + \kappa^2 Q_a Q_p)$$

Since the cavity $Q_p$ is not a controllable quantity, to increase $\eta$ the product $\kappa^2 Q_a$ must be maximized. The coupling coefficient, $\kappa$, can be increased by increasing the length of the antenna. The ultimate size is limited by the size of the tokamak chamber and the locations of the ports. The antenna Q, $Q_a = \omega L_{ant}/R_{ant}$ can be increased in two ways, i.e., decrease the antenna resistance or increase the antenna inductance. To decrease the antenna resistance, a bigger conductor for the antenna should be used. The limit on the size of the conductor is the size of the ports on the tokamak. The inductance of the antenna can be increased by increasing the number of turns on the loop antenna. Since the inductance increases approximately as the number of turns squared and the antenna resistance increases linearly as the number of turns, the antenna Q should increase linearly with the number of turns.

For the heating experiment it is essential to be able to couple to one of the cavity modes for a substantial amount of time. The present plasma condition in the Caltech tokamak makes the heating experiment difficult because of the fast density decay causing the cavity modes to be

swept through very quickly. To improve the situation, the plasma density must be kept as constant as possible. This can be done by gas puffing, where during the discharge a small amount of neutral gas is introduced into the tokamak. The gas is ionized, thus increasing the plasma density. By programming how the gas is puffed into the system, the plasma density can be tailored to specification.

Moreover, from the approximate cut-off relation of the magnetosonic wave, $f_{\ell mn} \sim 1/\sqrt{n_e}$, one can see that the input frequency can be swept to compensate for the change in the density. There are several ways to track the modes by frequency modulation. One way is to use a phase locked loop, i.e., by using the phase information from the transmission measurement as the control signal for a voltage controlled oscillator. As the density moves away from the required value for a cavity resonance, the phase of the transmitted signal would shift. This shift in phase can be used to change the input frequency so as to return to the resonance condition. Another method is to use positive feedback, i.e., to use the transmitted signal picked up by a receiving probe as the input for a broad-band amplifier driving the antenna, thus making the cavity resonance the frequency determining element of the oscillation system. If the gain of the amplifier is higher than the loss through the cavity, positive oscillation is excited. This oscillation will adjust its own frequency in order to stay on the cavity resonance.

At first sight the high Q nature of the input antenna might appear as a limitation for mode tracking because of the narrow bandwidth of the antenna with its tuning network. However, at the cavity resonances the plasma loading resistance increases substantially, and so the loading

resistance on the antenna will decrease the input Q. In the low power experiments, plasma resistive loading was observed as high as four times the antenna resistance. Thus for an antenna with Q = 100, the loaded Q at the cavity resonance is only 20. To compensate a change in the plasma density of 10%, a 5% change in the input frequency is required, or an antenna Q ($Q \sim 2n_e/\Delta n_e$) of 20 is needed at the cavity resonance.

## Appendix a

## TRANSMITTING ANTENNA AND MATCHING NETWORK CONSTRUCTION

The transmitting antenna is a two turn loop made of 1/8 inch copper tubing. The copper tubing is enclosed in a 1/32 inch thick layer of pyrex insulator. The functions of the glass are to protect the copper from plasma damage and to insulate the antenna from the plasma electrically. The approximate loop area of the antenna is 3.5 inches by 1 inch. Because of the glass coating, the antenna never intrudes more than 1.25 inches into the tokamak vacuum chamber. (Figure a.1)

The glass coating surrounding the copper is joined to a 1/2-inch OD Cajon (G304-8-GM-3) stainless steel-to-glass transition tube. The transition tube provides the mechanical feed-through for the antenna to go from vacuum to the outside. The glass portion is needed to give the antenna electrical insulation from the stainless steel wall of the tokamak. The transition tube goes through a vacuum o-ring and attaches to a 5/8" OD copper tubing. Finally, an Amphonel twin axial connector is screwed on the copper tubing to make the connection to the matching network.

A copper inner lining of 0.25 inch thick is pressed inside the 3 inches of Cajon stainless tubing to minimize the eddy current losses due to image currents produced inside the feed-through. The length of the entire antenna is kept to a minimum so that the antenna resistance can be reduced below the plasma loading resistance. The entire antenna measures 12 inches. The extra length is due to a mechanical carriage

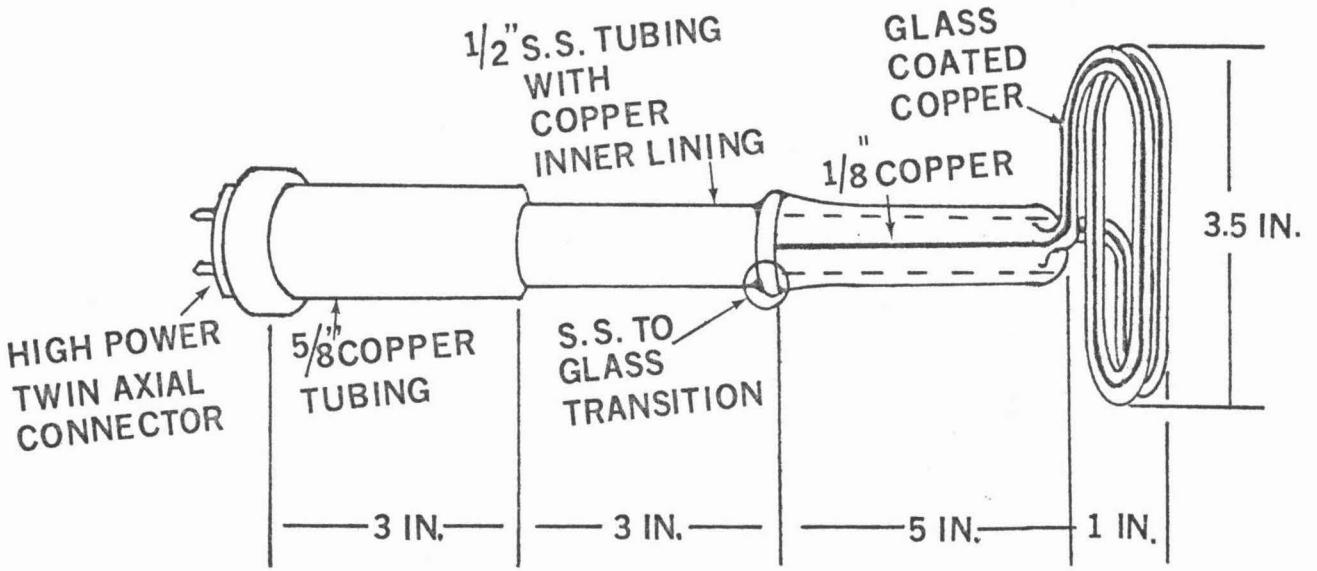


Figure a.1
Design of the two-turn copper antenna.

made for the antenna to move it smoothly in and out of the plasma. The ultimate limitation on the antenna size and the feed-through length is determined by the tokamak port size which is 4 x 6 x 1 inch.

The antenna resistance and inductance are a function of the distance that the antenna protrudes into the vacuum chamber of the tokamak. The reason for this dependence on the distance into the vacuum chamber is because of the 6 x 4 x 1 inch stainless steel port where the antenna sits when it is completely outside the tokamak vacuum chamber. The effect of the stainless steel port is to lower the antenna inductance and increase the antenna resistance through eddy current losses in the port wall. Therefore, as the antenna moves out of the port and into the vacuum chamber, the antenna inductance should show an increase with distance, and the antenna resistance should show a decrease of the distance. Data for the antenna impedance as function of the distance into the tokamak chamber are shown in Figure a.2. In Figure a.2, r = 0 corresponds to the case where the antenna sits just outside the tokamak chamber and completely inside the port; thus, r is the distance that the front surface of the antenna is inside the tokamak.

The antenna inductance measured in the experiment is approximately independent of the input frequency, and the antenna resistance increases with an increase in the input frequency. The frequency dependence of the antenna resistance is shown in Figure a.3. The data were taken with the antenna at 1.5 inches into the tokamak chamber

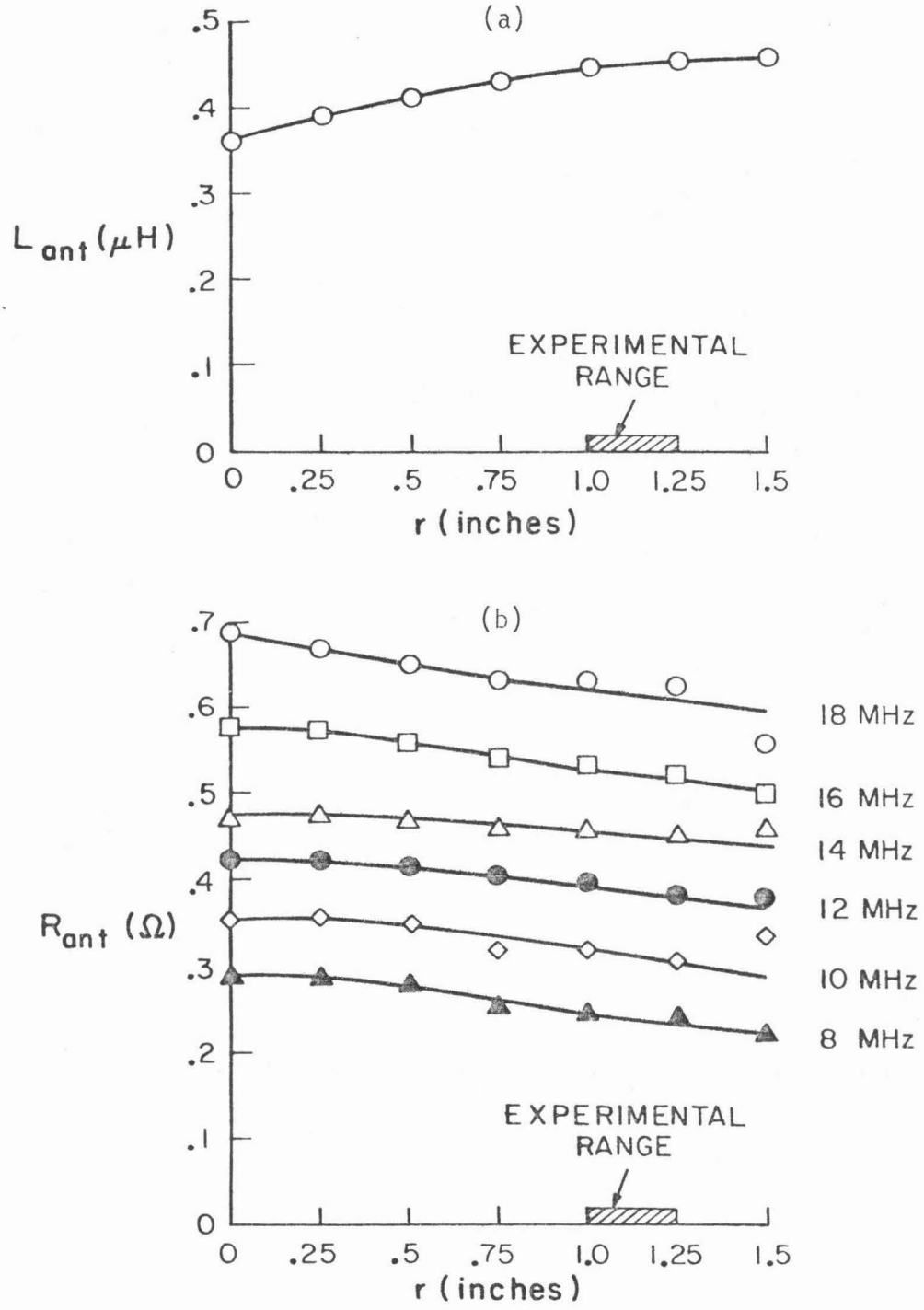


Figure a.2
The antenna inductance and resistance as a function of radial position into the vacuum chamber. r = 0 is the position that the antenna is just outside the chamber.

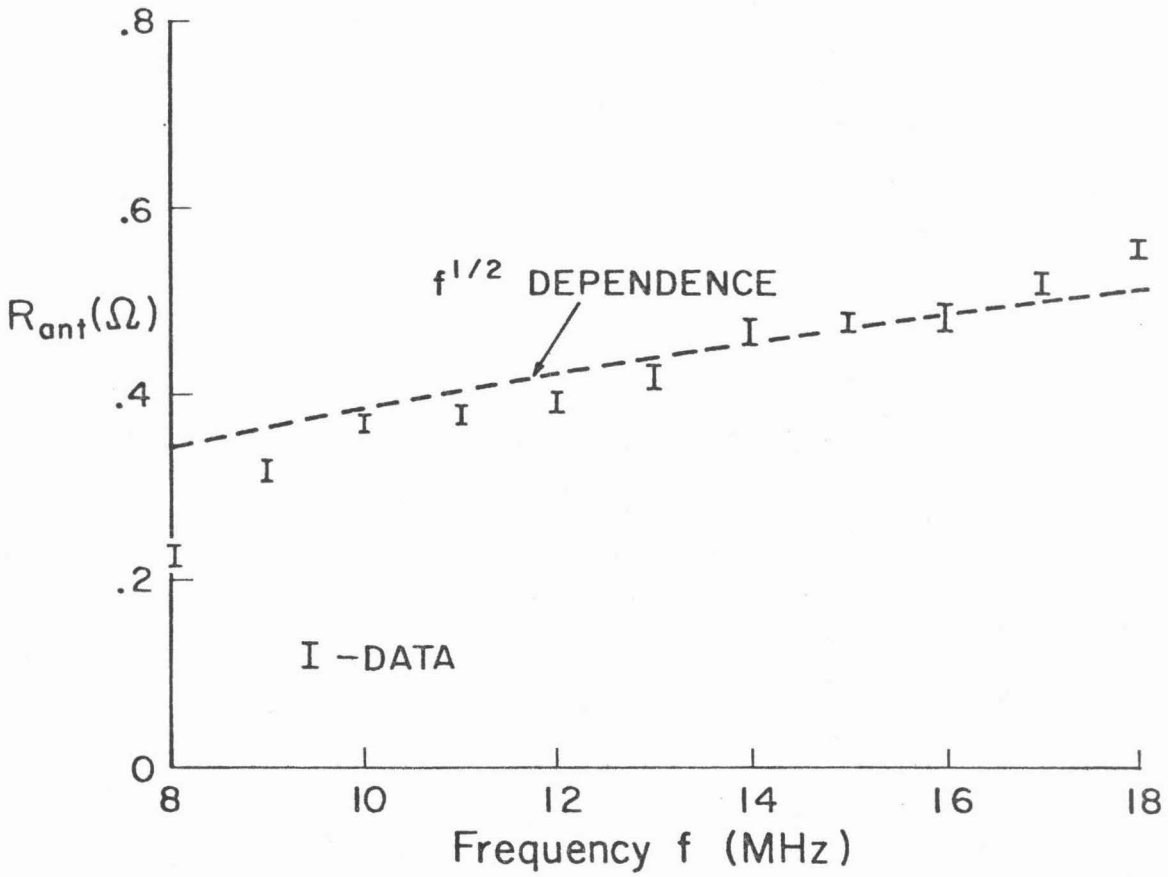


Figure a.3

Antenna resistance as a function of frequency. Data taken with the antenna at 1.5" into the tokamak. A $R_{ant} \propto f^{1/2}$ curve is superimposed on the data.

thus minimizing the effects of the stainless steel port. Superimposed on the experimental data is an $R_{ant} \propto f^{1/2}$ dependence fit, which is the expected frequency dependence from skin effect calculations.

The matching network is a two capacitor arrangement shown in Figure 2.4. Because of the low resistance and accurate tuning capability required, fifteen-turn Jennings vacuum variable capacitors are used. For tuning the antenna in the frequency range between 6 and 20 MHz, the capacitor in parallel with the antenna, $C_1$, ranges between 30 to 2000 picofarads, and the capacitor in series with the generator impedance ranges between 15 to 300 picofarads. The values of $C_1$ and $C_2$ for various tuning conditions are shown in Tables 5.1, 5.2, and 5.3.

## Appendix b

## COLD PLASMA THEORY OF THE MAGNETOSONIC CAVITY MODES
(based on unpublished memorandum by R. W. Gould, 1960)

Consider a uniform cold collisionless plasma, axially magnetized in a cylindrical geometry (Figure b.1). The axial magnetic field makes the plasma anistropic; thus, the dielectric property of the plasma must be expressed as a tensor quantity.

Define a general displacement, $\underline{D}$, with $e^{j\omega t}$ time dependence for the plasma [16].

$$j\omega\underline{D} = j\omega\underline{E} + \sum_n \underline{J}_n = j\omega\underline{\underline{\varepsilon}}\cdot\underline{E} \qquad (b.1)$$

where $\underline{J}_n = \sum_n q_n Z_n \underline{V}_n$ is the current density of the $n^{th}$ species of particles, $Z_n$ is the ionic charge, $q_n$ is the sign of the charge, and $\underline{\underline{\varepsilon}}$ is the dielectric tensor. Subtituting into equation b.1 the momentum equation where $\underline{V}_n$ has $e^{j\omega t}$ time dependence,

$$m_n \frac{d\underline{V}_n}{dt} = Z_n q_n e(\underline{E} + \underline{V}_n \times \underline{B}_o) \qquad (b.2)$$

into the current desnity $\underline{J}_n$, the dielectric tensor becomes the following

$$\underline{\underline{\varepsilon}} = \begin{bmatrix} \varepsilon_\perp & j\varepsilon_x & 0 \\ -j\varepsilon_x & \varepsilon_\perp & 0 \\ 0 & 0 & \varepsilon_{||} \end{bmatrix} \qquad (b.3)$$

where

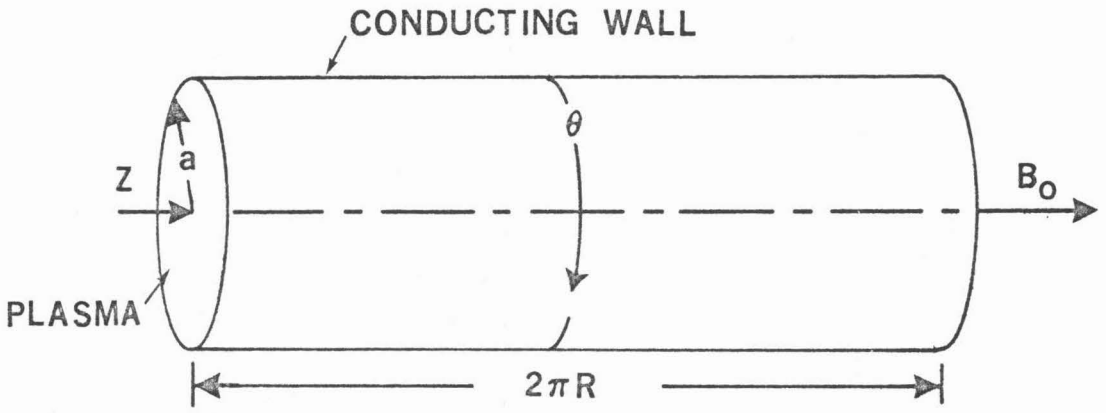


Figure b.1

Plasma filled cylindrical cavity with conducting wall. Periodic boundary condition is imposed in the z direction to simulate the closing of the torus. R = the tokamak major radius, and a = the tokamak minor radius.

$$\varepsilon_{\perp} = \frac{\varepsilon_o}{2}(R + L) \quad , \varepsilon_x = \frac{\varepsilon_o}{2}(L - R)$$

$$R = 1 - \sum_n \frac{\omega_{pn}^2}{\omega^2}\left(\frac{\omega}{\omega + q_n\omega_{cn}}\right) \quad , L = 1 - \sum_n \frac{\omega_{pn}^2}{\omega^2}\left(\frac{\omega}{\omega - q_n\omega_{cn}}\right)$$

$$\varepsilon_{11} = \varepsilon_o[1 - \sum_n \omega_{pn}^2/\omega^2]$$

In the tensor, two frequencies, $\omega_{pn}$ and $\omega_{cn}$, have been defined as follows

$$\omega_{cn} = |\underline{B}_o| Z_n e/m_n$$

$$\omega_{pn} = (n_n Z_n^2 e^2/\varepsilon_o m_n)$$

where $\omega_{cn}$ and $\omega_{pn}$ are the cyclotron and plasma frequencies respectively.

With the dielectric tensor, Maxwell's equations are cast in the following form

$$\nabla \times \underline{H} = \frac{\partial}{\partial t}(\underline{\underline{\varepsilon}} \cdot \underline{E}) \qquad (b.4)$$

$$\nabla \times \underline{E} = \frac{\partial}{\partial t}(\mu_o \underline{H}) \qquad (b.5)$$

When $e^{j(\omega t - m\theta - kz)}$ dependence of the fields is assumed in the cylindrical geometry, the following set of equations are obtained:

$$kE_\theta - \frac{m}{r} E_z = \omega\mu_o H_r \tag{b.6}$$

$$jkE_r + \frac{\partial E_z}{\partial r} = j\omega\mu_o H_\theta \tag{b.7}$$

$$\frac{1}{r}\frac{\partial}{\partial r}(rE_\theta) + \frac{jm}{r} E_r = -j\omega\mu_o H_z \tag{b.8}$$

$$k H_\theta - \frac{m}{r} H_z = -\omega(\varepsilon_\perp E_r + j\,\varepsilon_x E_\theta) \tag{b.9}$$

$$jk\cdot H_r + \frac{\partial H_z}{\partial r} = -j\omega(i\varepsilon_\perp E_r - \varepsilon_x E_z) \tag{b.10}$$

$$\frac{1}{r}\frac{\partial}{\partial r}(r\,H_\theta) + \frac{jm}{r} H_r = j\omega\varepsilon_{11} E_z \tag{b.11}$$

After some manipulation, the above equations can be reduced to two second order differential equations involving only the longitudinal components of the fields, $H_z$ and $E_z$. Following the notations used by R. W. Gould [17].

$$\left(\frac{1}{r}\frac{\partial}{\partial r}\left(r\frac{\partial}{\partial r}\right) - \frac{m^2}{r^2}\right)\phi_1 + \frac{j\omega\mu_o}{jd + \alpha_1 c}\phi_1 = 0 \tag{b.12}$$

$$\left(\frac{1}{r}\frac{\partial}{\partial r}\left(r\frac{\partial}{\partial r}\right) - \frac{m^2}{r^2}\right)\phi_2 + \frac{j\omega\mu_o}{jd + \alpha_2 c}\phi_2 = 0 \tag{b.13}$$

where $E_z = \phi_1 + \phi_2$, and $H_z = \alpha_1\phi_1 + \alpha_2\phi_2$. Here $\alpha_1$ and $\alpha_2$ are constants. Also $d = -\omega\mu_o\gamma_1/g$, $c = k\gamma_2/g$, $g = \gamma_1^2 - \gamma_2^2$, and $\gamma_1 = k^2 - \omega^2\mu_o\varepsilon_\perp$, $\gamma_2 = \omega^2\mu_o\varepsilon_x$. If a radial component of the wave vector, T, is defined as $T^2 = \omega\mu_o/(d - j\alpha c)$, then equations (b.12) and (b.13) are just the Bessel's equation, and the solution of $\phi_n$, where n can be 1 or 2, is as follows

$$\phi_n = \phi_o J_m(T_n r) e^{j(kz + m\theta - \omega t)}$$

where $\phi_o$ is a constant. The dispersion relation can be expressed as follows

$$[\gamma_1^2 - \gamma_2^2 + \gamma_1 T^2] - \frac{T^2}{\omega^2 \mu_o \varepsilon_{11}} [\gamma_1^2 - \gamma_2^2 + \gamma_1 T^2 - k^2(\gamma_1 + T^2)] = 0 \tag{b.14}$$

As indicated in this equation, for every value of $T^2$ there exist four possible solutions of k.

Since only frequencies near the ion cyclotron frequency are of interest the dispersion relation can be simplified by the following approximations. For $\omega \sim O(\omega_{ci})$, $B_o = 4$ kG($f_{ci} = 6$ MHz), density = $5 \times 10^{12}$ $cm^{-3}$, Z = 1 for hydrogen, then

$$\omega_{pe} \sim 1.5 \times 10^{11} \text{ rad/sec}$$

$$\omega_{pi} \sim 3 \times 10^{9} \text{ rad/sec}$$

$$\omega_{ce} \sim 7 \times 10^{10} \text{ rad/sec}$$

$$\omega_{ci} \sim 4 \times 10^{7} \text{ rad/sec}$$

where $\omega_{pe}$ and $\omega_{pi}$ are the electron and ion plasma frequencies, $\omega_{ce}$ and $\omega_{ci}$ are the electron and ion cyclotron frequencies. Therefore, $\omega_{ce} >> \omega_{ci}$, $\omega_{pe} >> \omega_{ci}$. Let $\Omega_i = \omega/\omega_{ci}$. The components of the dielectric tensor can be simplified as follows

$$\varepsilon_{\perp} \simeq \varepsilon_o \frac{\omega_{pi}^2}{\omega_{ci}^2 - \omega^2}$$

$$\varepsilon_x = \varepsilon_o \frac{\omega}{\omega_{ci}} \left[ \frac{\omega_{pe}^2 \, \omega_{ce} \, \omega_{ci}}{\omega^2 \, \omega_{ce}^2 (1 - \frac{\omega^2}{\omega_{ce}^2})} - \frac{\omega_{pi}^2 \, \omega_{ci}^2}{\omega^2 (\omega_{ci}^2 - \omega^2)} \right]$$

$$= \varepsilon_o \, \Omega_i \left[ \frac{\omega_{pi}^2}{\omega^2} \frac{\omega_{ce}^2}{(\omega_{ce}^2 - \omega^2)} - \frac{\omega_{pi}^2 \, \omega_{ci}^2}{\omega^2 (\omega_{ci}^2 - \omega^2)} \right] \qquad \text{(b.15)}$$

$$= \varepsilon_o \, \Omega_i \omega_{pi}^2 \left[ \frac{(\omega_{ci}^2 - \omega_{ce}^2)}{(\omega_{ci}^2 - \omega^2)(\omega_{ce}^2 - \omega^2)} \right]$$

$$\varepsilon_x \simeq - \varepsilon_o \, \Omega_i \frac{\omega_{pi}^2}{\omega_{ci}^2 - \omega^2} = - \Omega_i \varepsilon_{\perp}$$

$$\varepsilon_{||} \simeq - \varepsilon_o \left( \frac{\omega_{pe}}{\omega_{ci}} \right)^2 \sim - \varepsilon_o (1 \times 10^7) \qquad \text{(b.16)}$$

For $\varepsilon_{||}$ very large compared to the other terms in the dispersion relation (equation b.14), one can make the following approximation

$$\varepsilon_{||} \rightarrow \infty$$

By substituting this approximation into equation b.14, the simplified

dispersion relation is as follows:

$$\gamma_1^2 - \gamma_2^2 + \gamma_1 T^2 = 0 \tag{b.17}$$

Substituting the values of $\gamma_1$ and $\gamma_2$ the solution of $k^2$ in terms of $T^2$ is

$$k^2 = \omega^2 \varepsilon_\perp \mu_o - \frac{T^2}{2} + \sqrt{(T^2/2)^2 + (\omega^2 \mu_o \varepsilon_x)^2} \tag{b.18}$$

$$k^2 = \omega^2 \varepsilon_\perp \mu_o - \frac{T^2}{2} - \sqrt{(T^2/2)^2 + (\omega^2 \mu_o \varepsilon_x)^2} \tag{b.19}$$

A consequence of $\varepsilon_{||}$ being large compared to the various other quantities in the differential equation, is that $E_z$ is small (see equation (b.11)). In our approximation we will take $E_z = 0$.

As mentioned before, the magnetosonic wave is right circularly polarized; thus, it has no resonance at the ion cyclotron frequency. Since there are two branches of the dispersion relation (b.17), one can check the polarization of the waves propagating along the longitudinal d.c. magnetic field by letting $T \to 0$. It is easier to find the polarization of the wave in rectangular coordinates. As $T \to 0$, the cylindrical solution should reduce to the same solution.

The polarization of an electromagnetic wave can be expressed as follows:

$$\frac{jE_x}{E_y} = \pm 1$$

where +1 corresponds to a right circularly polarized wave, and -1 corresponds to a left circularly polarized wave. The polarization of an oblique wave propagating in a cold magnetized plasma is

$$\frac{jE_x}{E_y} = \frac{\eta^2 - S}{D} \tag{b.20}$$

where the d.c. magnetic field is in the z direction, $\eta = kc/\omega$ is the index of refraction, $S = \varepsilon_\perp/\varepsilon_o$, $D = -\varepsilon_x/\varepsilon_o$. For propagation along the d.c. magnetic field, there are two solutions:

$$\eta^2 = R \tag{b.21}$$

$$\eta^2 = L \tag{b.22}$$

When these solutions are substituted into equation (b.20) and the definition of the dielectric tensor (b.3) is used, the following polarizations are found for the two branches.

$$\frac{jE_x}{E_y} = \frac{R-S}{D} = +1 \quad ; \quad \frac{jE_x}{E_y} = \frac{L-S}{D} = -1$$

$\eta^2 = R$ is a right circularly polarized wave and $\eta^2 = L$ is a left circularly polarized wave.

For frequencies near the ion cyclotron frequency, the following simplification to the dispersion relation can be made. For $\omega \sim \omega_{ci}$ the frequency is small compared to the electron cyclotron frequency and to the electron plasma frequency. Therefore, R can be approximated as follows:

$$R \sim \frac{c^2}{V_A^2} \frac{1}{(1+\Omega_i)}$$

where $V_A = B_o/\sqrt{\mu_o n_i m_i}$ is the Alfven velocity, and $B_o$ is the d.c. magnetic field. Thus for the right circularly polarized wave

$$k^2 \simeq \frac{\omega^2}{V_A^2} \frac{1}{(1+\Omega_i)} \tag{b.23}$$

and so there is no resonance at the ion cyclotron frequency, i.e., $\Omega_i = 1$. For the left circularly polarized wave

$$L \simeq \frac{c^2}{V_A^2}\left(\frac{1}{1-\Omega_i}\right)$$

and (b.24)

$$k^2 \simeq \frac{\omega^2}{V_A^2}\frac{1}{(1-\Omega_i)}$$

so for this wave there is a resonance at the ion cyclotron frequency. As $T \to 0$ in equations (b.18) and (b.19), we have

$$k^2 = \omega^2\mu_o[\varepsilon_\perp + \varepsilon_x] = \frac{\omega^2}{c^2}L \qquad \text{(b.18a)}$$

$$k^2 = \omega^2\mu_o[\varepsilon_\perp - \varepsilon_x] = \frac{\omega^2}{c^2}R \qquad \text{(b.19a)}$$

And so equation (b.19) is the magnetosonic branch that is of interest.

Since the tokamak has a conducting wall, consider the solution of the magnetosonic wave in a cylindrical cavity. To simulate the closing of the tokamak on itself, periodic boundary condition in the axial direction is imposed (i.e., $k = N/R$ where R = major radius of the tokamak, see Fig. b.1). At $r = a$, a perfectly conducting wall is assumed; thus the tangential electric field $E_t$ and the normal magnetic field $H_n$ must vanish. Since the approximation of $\varepsilon_\parallel \to \infty$ implies that $E_z = 0$, all the remaining fields can be written in terms of $H_z$.

$$H_r = \frac{-jk}{T^2}\left[\frac{\partial H_z}{\partial r} + \frac{\gamma_2}{\gamma_1}\frac{m}{r}H_z\right] \qquad \text{(b.25)}$$

$$H_\theta = -\frac{k}{T^2}\left[\frac{m}{r}H_z + \frac{\gamma_2}{\gamma_1}\frac{\partial H_z}{\partial r}\right] \qquad \text{(b.26)}$$

$$E_r = -\frac{\omega\mu_o}{T^2}\left[\frac{m}{r}H_z + \frac{\gamma_2}{\gamma_1}\frac{\partial H_z}{\partial r}\right] \tag{b.27}$$

$$E_\theta = \frac{j\omega\mu_o}{T^2}\left[\frac{\partial H_z}{r} + \frac{\gamma_2}{\gamma_1}\frac{m}{r}H_z\right] \tag{b.28}$$

Note that

$$E_r = \frac{\omega}{k}\mu_o H_\theta \tag{b.29}$$

$$E_\theta = -\frac{\omega}{k}\mu_o H_r \tag{b.30}$$

The solution of (b.12) is the integer Bessel's function. Thus, $H_z$ is

$$H_z = H_o J_m(Tr)e^{j(\omega t - m\theta - kz)} \tag{b.31}$$

The boundary condition is $E_\theta = H_r = 0$ at $r = a$, or from (b.25) we have

$$Ta\, J'_m(Ta) + \frac{\gamma_2}{\gamma_1} m\, J_m(Ta) = 0 \tag{b.32}$$

[For more details on the fast magnetosonic cavity modes see references 31 to 35].

## Appendix c

## RESISTIVITY LOADING OF THE R.F. WAVE BY TOKAMAK WALL

The r.f. energy generated in the tokamak by the transmitting antenna can be assumed to be either dissipated in the plasma, or lost in the tokamak wall which has a finite conductivity. It is important to estimate the resistive loading of the wave due to the finite conductivity of the tokamak wall, and to compare the calculated value with the measured resistivity loading in the low power experiment. If the estimated loss in the tokamak wall can account for most of the resistive loading effects measured in the low power experiments, then the validity of the high power experiment becomes questionable, because the r.f. wave will tend to heat the tokamak wall more than the plasma.

The most convenient method to study the effect of the tokamak wall loading is to compare the estimated Q of the cavity, due to wall losses alone, with the measured Q of the cavity. If the estimated Q due to the wall, denoted by $Q_w$, is comparable to the measured Q, then the wall loading is the dominating dissipation factor in the tokamak.

One approach to estimate $Q_w$ is to calculate the damping decrement, $\gamma$, of the cavity modes due to the finite resistivity of the cavity wall. The damping decrement is defined as the attenuation per unit time of the electromagnetic wave in the cavity. If the time dependence of the $i^{th}$ eigenmode is assumed to be $e^{j\omega_i t}$, where $\omega_i = \omega_{0i} + j\omega_2$, then the damping decrement $\gamma_i$ is just $\omega_2$. The cavity $Q_w$ can be related to the damping decrement as

$$Q_w = \omega_{0i}/2\gamma_i \qquad (c.1)$$

where $\omega_{0i}$ is the $i^{th}$ eigenmode frequency of the cavity. The damping decrement due to the cavity wall can be calculated for the various modes by using a finite conducting wall boundary condition at the cavity wall. The new boundary condition is

$$\underline{E} = \hat{n} \times \underline{H}(1+j)\sqrt{\frac{\omega\mu_o}{2\sigma}}$$

where $\sigma$ is the conductivity of the wall and $\hat{n}$ is the outer normal to the wall [36]. If the tokamak is again approximated by a cylinder with periodic boundary in the axial direction, then the boundary can be written in terms of $E_\theta$ and $H_z$,

$$E_\theta/H_z = (1+j)\sqrt{\omega\mu_o/2\sigma} \qquad (c.2)$$

The real part of the term on the right is the wall resistance, and the imaginary part is the additional reactance from the wall. From Appendix b, the solution of $H_z$ for a plasma-filled cylindrical cavity is as follows:

$$H_z = H_o J_m(Tr)\, e^{j(\omega t - m\theta - kz)} \qquad (c.3)$$

$E_\theta$ is related to $H_z$ in the following manner (b.28)

$$E_\theta = (j\omega\mu_o/T^2)[\partial H_z(Tr)/\partial r + \frac{\gamma_2}{\gamma_1}\frac{m}{r} H_z(Tr)] \qquad (c.4)$$

where T is the radial wave number, k is the axial wave number, and m is the azimuthal mode number. For the perfectly conducting wall $E_\theta = 0$ at $r = a$. Now the boundary condition at $r = a$ is

$$\frac{j\omega\mu_o}{T}\left[\frac{H_z'}{H_z} + \frac{\gamma_2}{\gamma_1}\frac{m}{\zeta}\right] = (1+j)\sqrt{\omega\mu_o/2\sigma} \qquad (c.5)$$

where Ta is replaced by $\zeta$, and $H_z' = \partial H_z/\partial\zeta$. Rearranging the above equation, obtain a dimensionless equation,

$$\frac{1}{\zeta}\left[\frac{H_z'}{H_z} + \frac{\gamma_2}{\gamma_1}\frac{m}{\zeta}\right] = \frac{(1-j)}{a}\sqrt{\frac{1}{2\sigma\omega\mu_o}} \qquad (c.6)$$

For a highly conducting wall, the term on the right side, $\frac{1}{a}\sqrt{\frac{1}{2\sigma\omega\mu_o}} << 1$. Thus, the wall resistance contributes a small imaginary term to $\zeta$ and the wall reactance adds a small real term to $\zeta$. If $\zeta$ is written as $\zeta = \zeta_o + j\delta$, where $\delta << \zeta_o$, then the wall resistance adds a damping term to the radial wave number T, and the wall reactance will shift the resonance frequency $\omega_i$ by a small amount. To find the damping decrement, solve the complex $T = \zeta/a$ and substitute into the dispersion relation (b.11):

$$k^2 = \frac{\Omega_i^2\,\omega_{ci}^2}{V_A^2(1-\Omega_i^2)} - \frac{T^2}{2} - \sqrt{\left(\frac{T^2}{2}\right)^2 + \frac{\Omega_i^3\,\omega_{ci}^2}{V_A^2(1-\Omega_i^2)}}$$

For the purpose of this section where only an estimated damping decrement is needed, the approximate dispersion relation can be used. For the lowest few axial mode numbers N, where $k = N/R$ and R is the major radius of the torus, the dispersion relation can be approximated in the following way:

$$\omega_i = \omega_o + j\gamma_i = V_A\sqrt{T^2 + k^2} \qquad (c.7)$$

where $V_A$ is the Alfven velocity. The simplest mode to estimate is the $k = 0$, $m = 0$, and the lowest T mode. From equation (b.32), one can see that the lowest radial mode for $m = 0$ corresponds to the first zero of the first integer order Bessel's function, $J_1$. Equation (c.7) can be reduced to the following:

$$\omega_{oi} + j\gamma_i = V_A T = V_A(T_o + j\delta/a) \qquad (c.8)$$

where $T_o = \zeta_o/a$. The following parameters for the Caltech tokamak are substituted into equations (c.6) and (c.8):

$\sigma$ = conductivity of stainless steel = $1 \times 10^6$ mho $m^{-1}$

a = minor radius = .15 m

R = major radius = .45 m

f = input frequency = 12 MHz

$\zeta_o$ = first zero of $J_1$ = 3.83

The following value of $Q_w$ is obtained

$Q_w$ = 1300

which is two to three times the various measured cavity Q in the experiment.

For the higher radial and axial modes, both $T_o$ and k will be larger, which means that $Q_w$ should be higher. Therefore, this estimated $Q_w$ for m = 0, k = 0 , and lowest radial mode is a lower limit for the higher modes. Although the wall loading is not negligible, it does not account for all the measured loading in the tokamak; thus, r.f. energy should be dissipated in the plasma.

REFERENCES

1. E. Thompson, "Perspective of Neutral Beam Injection Techniques," Proc. Third International Meeting on Theoretical and Experimental Aspects of Heating of Toroidal Plasmas, Grenoble, France, vol. 2, 93 (1976).

2. Equipe TFR, "Heating by Injection of Fast Neutrals and Study of the Ion Energy Balance in TFR," Proc. Sixth Conference on Plasma Physics and Controlled Nuclear Fusion Research, Berchtesgaden, Germany, vol. 1, 69 (1977).

3. T. H. Stix, "The Physics of R.F. Heating," Princeton Plasma Physics Lab. Report, Matt-929, Oct. 1972.

4. F. W. Perkins, M. Chance, and J. E. Kindel, Proc. Third International Symposium on Toroidal Plasma Confinement, Garching, Germany, Paper B8 (1973).

5. J. C. Hosea, W. M. Hooke, "Ion Cyclotron and Fast Hydromagnetic Wave Generation in the ST Tokamak," Phys. Rev. Lett. 31, 150 (1973).

6. H. Takahashi, C. Daughney, R. Ellis, R. Goldson, H. Hsuan, T. Nagashima, F. Paoloni, A. Sivo, S. Suckewer, Phys. Rev. Lett. 39, 31 (1977).

7. J. C. Hosea, Princeton Plasma Physics Lab., private communication.

8. J. Adam, M. Chance, H. Eubank, W. Getty, E. Hinov, W. Hooke, J. Hosea, F. Jobes, F. Perkins, R. Sinclair, J. Sperling, H. Takahashi, "Wave Generation and Heating in the ST Tokamak at the Fundamental and Harmonic Ion Cyclotron Frequencies," Proc. Fifth Conference on Plasma Physics and Controlled Nuclear Fusion Research, Tokyo, Japan, Paper IAEA-CN-33/A3-2 (1974).

9. V. L. Vdovin, et al., JETP Lett. 14, 149 (1973); JETP Lett. 17, 2 (1973).

10. N. V. Ivanov, I. A. Kovan, E. V. Los', JETP Lett. 14, 138 (1971); JETP Lett. 16, 60 (1972).

11. TFR Group, "Excitation and Damping of the Fast Magnetosonic Wave in TFR near the Harmonic Cyclotron Frequency," Proc. Third International Meeting on Theoretical and Experimental Aspects of Heating of Toroidal Plasmas," Grenoble, France, vol. 1, 87 (1976).

12. TFR Group, "Magnetosonic Wave Generation and Damping in the TFR Tokamak near the Ion Cyclotron Frequencies," Proc. Sixth International Conference on Plasma Physics and Controlled Nuclear Fusion Research, Vienna, Paper IAEA-CN-35/G8 (1977).

13. R. J. Taylor, G. J. Morales, "Efficiency of Power Absorption in the Ion-Cyclotron and Lower-Hybrid Ranges," 19th Annual Meeting of the Division of Plasma Physics, Atlanta, Georgia, Paper 7C7 (1977).

14. V. P. Bhatnagar, G. Bosia, M. Bures, J. Jacquinot, A. M. Messiaen, G. Telesca, P. E. Vandenplas, R. R. Weynants, "Preliminary RF Experiments on the Erasmus Tokamak," Proc. Third Topical Conference on Radio Frequency Plasma Heating, Pasadena, Calif., Paper C-4, (1978).

15. R. J. Taylor, G. J. Morales, "Efficiency of Antenna Coupling to the Fast Alfven Modes in Macrotor," Proc. Third Topical Conference on Radio Frequency Plasma Heating, Pasadena, Calif, Paper C-5 (1978).

16. T. H. Stix, The Theory of Plasma Waves (McGraw-Hill Book Co., Inc., New York, N.Y., 1962), Chapter 2.

17. R. W. Gould, Caltech, unpublished memo (1960) and private communication.

18. F. Paoloni, "Boundary Effects on M = 0,±1 Alfven Wave in a Cylindrical Collisionless Plasma," Phys. Fluids 18, 640 (1975).

19. F. Paoloni, "Coupling to Fast Eigenmodes in a Non-Uniform Plasma," Nuclear Fusion 18, 359 (1978).

20. E. L. Ginzton, Microwave Measurements (McGraw-Hill Book Co., Inc., New York, N.Y., 1957), Chapter 9.

21. J. C. Slater, Microwave Electronics (D. Van Nostrand Co., Inc., New York, N.Y., 1950), Chapter 4.

22. C. G. Montgomery, R. H. Dicke, E. M. Purell, Principles of Microwave Circuits (Dover Publications, Inc., New York, N.Y., 1965), Chapter 7.

23. C. G. Montgomery, et al., ibid, p. 221.

24. S. R. Seshadri, Fundamentals of Transmission Lines and Electromagnetic Fields (Addison-Wesley Publishing Co., Inc., Philippines, 1971), Chapter 2.

25. F. Paoloni, "Waveguide and Loop Coupling to Fast MHD Toroidal Eigenmodes," Princeton Plasma Physics Lab. MATT-1173 (1975).

26. L. Oren, R. J. Taylor, "Trapping and Removal of Oxygen in Tokamak," Nuclear Fusion 17, (1977).

27. D. J. Rose and M. Clark, Plasma and Controlled Fusion (MIT Press, 1961), p. 232-236.

28. D. J. Rose and M. Clark, ibid, p. 173.

29. R. C. Cross, "Construction of Diagnostic Equipment for the Texas Tech Tokamak," Texas Tech University, Plasma Laboratory Report NSF-ENG-7303941-2 (1977).

30. R. L. Kubena, "Fluctuations in a Tokamak Plasma," Ph.D. Thesis, California Institute of Technology (1978).

31. W. M. Hooke, M. A. Rothman, P. Avivi, J. Adam, "Measurements on the Fast Hydromagnetic Wave above the Ion Cyclotron Frequency", Physics of Fluids 5, 864 (1962).

32. N.I. Nazarov, A.I. Ermakov, V.V. Dolgopolov, L.N. Stepanov, V.T. Tolok, Nuclear Fusion 3, 255 (1963).

33. D. G. Swanson, R. W. Gould, R. H. Hertel, "Experimental study of Compressional Hydromagnetic Waves", Physics of Fluids 7, 269 (1964).

34. K. Chung, M. A. Rothman, "Plasma Heating by the Fast Hydromagnetic Wave", Physics of Fluids 10, 2634 (1967).

35. T. H. Stix, "Fast-Wave Heating of a Two Component Plasma", Nuclear Fusion 15, 737 (1975).